NUEJ

NARESUAN UNIVERSITY ENGINEERING JOURNAL

July-December 2023 Vol.18, No.2
ISSN : 2651-1568

NUEJ
Naresuan University
Engineering Journal

Editorial Team

NUEJ

Naresuan University Engineering Journal

Editorial Board

NUEJ
Naresuan University
Engineering Journal

NUEJ
Naresuan University
Engineering Journal

Research Articles

NUEJ
Naresuan University
Engineering Journal

Aims and Objectives

The primary objective of *the Naresuan University Engineering Journal (NUEJ)* is to publish high-quality research articles presenting contemporary developments in theory, design, and applications in all areas of Engineering, Science, and Technology, including research in Civil, Environmental, Mechanical, Electrical, Computer, Industrial, Chemical, and Material Engineerings. NUEJ covers all multidisciplinary research in associated areas, such as Mechatronics, Energy, Industrial and Engineering Design, Manufacturing Technology, Engineering Management, and Medical Engineering.

Journal Policies

Naresuan University Engineering Journal (NUEJ) is a peer reviewed journal, regularly published with 2 issues per year (January – June and July – December). Submissions must be original, unpublished works and not currently under review by other journals. NUEJ will consider only submitted works which respect research ethics, including confidentiality, consent, and the special requirements for human and animal research All research articles dealing with human or animal subjects must attach an approval certificate from the Ethics Committee. Additionally, the research article dealing with human subjects must provide evidence of informed consent.

Editorial board of NUEJ reserves the right to decide whether the submitted manuscript should be accepted for publication. The final decision of the editorial board cannot be appealed.

The submitted manuscript has to be written in English only, and can be in Microsoft Word (doc or docx) or PDF file format. The corresponding author is required to register and submit the manuscript at https://ph01.tci-thaijo.org/index.php/nuej

Editorial board of Naresuan University Engineering Journal (NUEJ)
Faculty of Engineering, Naresuan University
Phitsanuloke, 65000 Thailand
Tel. +66(0)55 963951
Fax. +66(0)55 964000
Email: nuej@nu.ac.th

NUEJ
Naresuan University Engineering Journal

Editor's Note

Advancing Engineering for Entrepreneurial Society

Greetings to all our readers,

As the editor of Naresuan University Engineering Journal, I am delighted to present the latest issue of our journal, which serves as a vital platform for the exchange of knowledge and experiences in the ever-evolving and forward-moving field of engineering.

In this issue, we have compiled research articles that are both challenging and exciting. They reflect not only the advancements in various engineering disciplines but also the pursuit of sustainable and environmentally responsible methods. From the development of new materials to the application of advanced technologies in solving engineering problems, this issue covers a broad spectrum.

We also emphasize supporting new researchers by providing opportunities for them to publish high-quality work that presents new directions in the field of engineering. These works are not only valuable sources of information for academics but also an inspiration for the next generation of researchers.

The connection to society and industry is equally important. Hence, our journal is not just an academic forum but also a bridge linking engineering knowledge to its real-world applications.

Finally, I would like to express my gratitude to our editorial team, peer reviewers, and all members who contribute to the creation and maintenance of the quality of this journal. It is our hope that our journal will continue to be a source of high-quality knowledge and benefit the field of engineering and entrepreneurial society

With respect,

Assist Prof. Dr. Ananchai Ukaew
Editor
Naresuan University Engineering Journal

NUEJ
Naresuan University
Engineering Journal

Low Frequency Planar Wireless Power Transfer with Impedance Matching using L-Section Matching Network for Underwater EVs

Hajira Masood, Watchara Amasiri, Artit Rittiplang, and Wanchai Pijitrojana*

Department of Electrical and Computer Engineering, Thammasat School of Engineering, Thammasat University, Pathum Thani, Thailand 12120

*Corresponding author e-mail: pwanchai@engr.tu.ac.th

(Received: 14 August 2022, Revised: 24 June 2023, Accepted: 26 June 2023)

Abstract

For the Wireless Power Transfer (WPT) system, the impedance Matching (IM) is the technique in which a wide range of resonant and strong coupling structures have been studied which mostly operate at an ideal parameter, i.e., resistive load and high RF greater than1MHz, however these parameters have some limitations in which the most important is that the high frequency is usually inefficient and complex load. This paper presents an L-section matching network to find the ideal load and source conditions. Thus, under the normal load and source conditions, we estimate the maximum power transfer efficiency and describe how to configure the matching network for the given load and source conditions for low-frequency WPT system. The L-section matching network to connect to a WPT structure using air-core spiral coils. The following configuration of network can operate at a low frequency of 20 kHz. From the calculation the moderate efficiency is 67 % while the efficiency from the experiment is 60 % at 9-cm transfer distance without an ideal parameter. The applications of the proposed work are suitable for underwater electric vehicles. Since the eddy current loss of seawater is critical when the operating frequency is higher than 250 kHz.

Keywords: impedance matching, Low-frequency wireless power transfer, L-section matching network, wireless power transfer system for underwater electric vehicles.

1. INTRODUCTION

Wireless power transfer based on magnetic resonant coupling appears to be difficult for commercial applications until the last few years (Shinohara et al., 2017, Li et al., 2015). Nowadays the common form of WPT mainly consists of three ways, radio waves or microwaves, inductive coupling or inductive power transmission and electromagnetic resonant coupling. It has been widely used in many applications as highlighted in Fig.1.

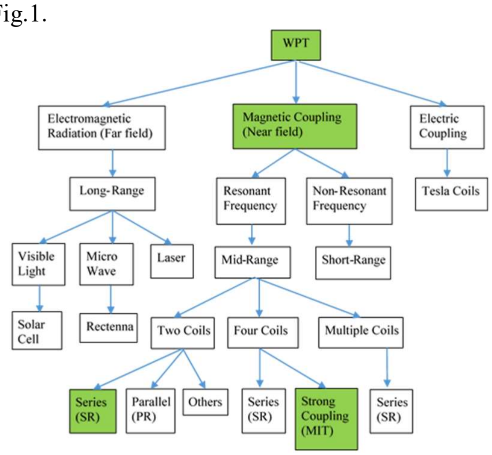

Figure 1 WPT categories and structures (Jang et al., 2016).

For an efficient power transmission, WPT should fulfill three conditions: (a) high power, (b) large air gap, and (c) high efficiency (Li et al., 2015). The efficiency of WPT system also depends on WPT techniques. Transfer efficiencies of different WPT techniques for both near and far region, 70 % to 90 % transfer efficiency can be achieved through inductive coupling while magnetic resonance coupling offers a moderate efficiency of 40% to 60%. These transfer efficiencies decay with distance. Especially, in the underwater environment, WPT technology solves the problem of wet plugging and the unplugging of underwater energy supply and provides a safer method for the rapid charging of autonomous underwater vehicles (AUVs) (Zhang et al., 2016, Yan et al., 2019, Kim et al., 2019, Dou et al., 2019) and unmanned underwater vehicles (UUVs). Therefore, in view of the widespread application of underwater WPT technology, it is of great research significance to improve its energy transmission efficiency.

The WPT system in the air uses one or more pairs of induction coils. The alternating current (AC) of the primary-side coil generates the induced alternating current (AC) in the coupled secondary-side coil, and then the direct current (DC) is generated through rectification to complete the power supply to the equipment. The process of underwater WPT is similar to that in the air, but the medium in the transmission area changes from air to seawater. There are various challenges for underwater WPT summarized here. 1. What is the effect of high conducting water medium on electrical parameters of WPT system? 2. How coil radiation resistance is affected by seawater? 3. What are the main losses incurred and how to minimize these losses? 4. If any loss is highly dependent of frequency then how to select an operating frequency to achieve an efficient wireless power transmission (Syed et al., 2020)

Therefore, the underwater WPT process considered in this paper is to solve the third and fourth challenges. Since for underwater, the coupling characteristics between the coils have changed, and the changed magnetic field will generate eddy current in the seawater, which brings new energy loss, namely, eddy current loss. From (Shi et al., 2014), they analyzed various losses in underwater WPT systems, including copper loss, semiconductor loss, core loss, and eddy current loss by using circuit analysis and electromagnetic field (EMF) simulation.

In this paper, we focused to reduce eddy current loss. In order to reduce the eddy current loss of underwater WPT systems, several researchers have studied it. From (Zhang et al., 2018), they analyzed some factors that affect the eddy current loss of underwater charging systems, and used EMF simulation software to optimize the number of coils turns on the primary side and the secondary side and the frequency of the AC source, thereby reducing the eddy current loss, and also designed experiments to verify optimization results. From (Zhang et al., 2019), they presented a new coil structure, taking advantage of two primary-side coils placed symmetrically adjacent to each side of the secondary-side coil to reduce the eddy current loss of WPT systems for underwater vehicles.

Seawater medium is a good electromagnetic conductor. At a low electromagnetic frequency, since it satisfies the loss tangent, $\sigma/(\omega \cdot \varepsilon) >> 1$. The expressions for the seawater attenuation constant and phase constant can be simplified as follows: $\alpha \approx \beta \approx \sqrt{f\pi\mu\sigma} = 0.004\sqrt{f}$. The attenuation constant is not only related to the conductivity, permeability and dielectric constant of the seawater medium, but also closely related to the frequency of the electromagnetic wave. The attenuation is positively correlated with frequency, and this is more obvious in the high-frequency range. Therefore, it is given that the eddy current loss is caused by electromagnetic wave transmission in seawater medium, it can be reduced by controlling the transmission frequency to achieve efficient energy transmission.

A remarkable innovation of non-radiated wireless power transfer (WPT) system using strongly magnetic resonant coupling has been observed in recent years, and due to its operating range and efficiency, it has shown more prospects for powering devices (Shinohara et al., 2017, Jang et al., 2016, Choi et al., 2015, Li et al., 2016). Because the magnetic field weakly interacts with other objects in the surrounding environment, the resonant circuits are used to improve the efficiency (Shinohara et al., 2017). Nowadays, most of the WPT structures are usually presented the two-coil Series Resonance (SR) and strong coupling (MIT team) models as shown in Fig. 2 (a) - (b) (Shinohara et al., 2017, Jang et al., 2016, Choi et al., 2015, Li et al., 2016, Zhang et al., 2016, Yan et al., 2019, Kim et al., 2019). These structures can be achieved the high transfer distance at high frequency as shown in Fig. 2 (c), the transfer distance of 56 cm is achieved at 5.26 MHz with 36 % efficiency.

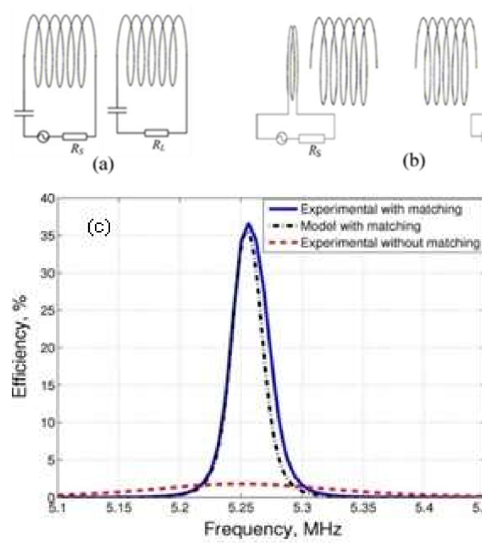

Figure 2 (a) The two-coil SR structure (Zhang et al., 2014c). (b) The strong coupling structure (Zhang, et al., 2014b) (c) The two-coil SR structure of the ten-tum at the transfer distance of 56 cm shows the high efficiency at about 5.26 MHz (Yan et al., 2019).

The Impedance Matching (IM) condition in Fig. 2 (a) - (b) is achieved by using an optimal parameter (usually either load or transfer distance) for improving the efficiency. However, an optimal parameter is a fixed value that limits the design, so this issue can be solved by using L-section matching networks as shown in Fig. 3.

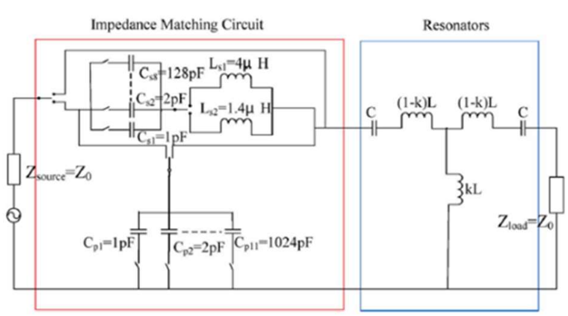

Figure 3 The IM circuit is connected to the two-coil SR structure at 13.56 MHz frequency operation (Beh et al., 2013).

As shown in Fig. 3, they proposed the high frequency operation at 13.56 MHz for obtaining the high transfer distance and efficiency. Unfortunately, the high - frequency RF sources are usually inefficient (Zhang et al.,

NUEJ
Naresuan University
Engineering Journal

2014, Zhang et al., 2014, Zhang et al., 2014), and the high-frequency operation causes eddy current loss for underwater media, electromagnetic interference, tissue absorption, etc. (Hui et al., 2014, Zhang et al., 2014, Zhang et al., 2014, Zhang et al., 2014, Jolani et al., 2014).

From (Wang et al., 2022), the simulation results of a single-plane coil using electromagnetic field simulation software are shown in the Fig. 4 - 6. Fig. 7 shows the AC resistance and eddy current loss resistance of the planar coil in the air and seawater, respectively. Fig. 8 and 9 show the comparison of its electric field intensity modulus and phase angle under different frequency excitations. It can be seen from the results as shown in the figures below that in the air medium, the eddy current loss resistance is always zero, while in the seawater medium, with the increase in frequency, the eddy current loss resistance increases rapidly. However, with the low frequency under 100 kHz, the eddy current loss resistance, the electric field intensity modulus and phase angle under different frequency excitations do not affect the underwater WPT system.

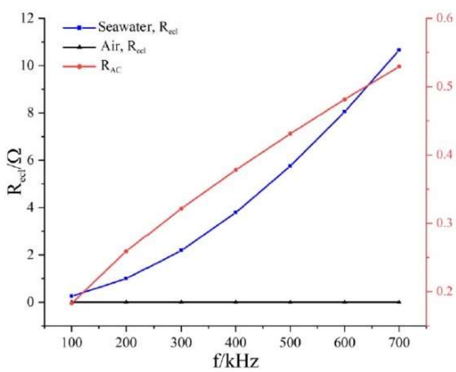

Figure 4 Variation of AC resistance and eddy current loss resistance with frequency.

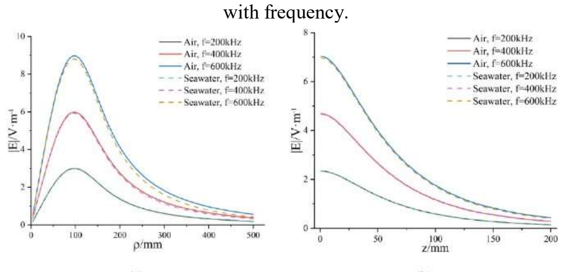

Figure 5 Modulus of electric field intensity generated by planar coil in the (a) radial direction (b) axial direction.

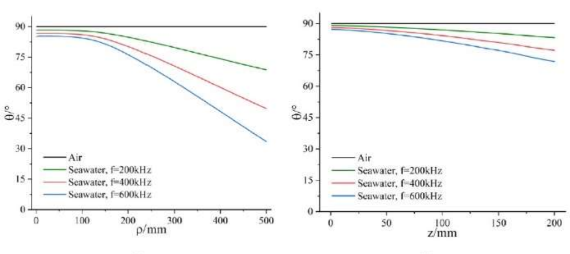

Figure 6 Phase of electric field intensity generated by planar coil in (a) radial direction (b) axial direction.

Thus, in this work, we propose a low-frequency WPT by a secondary capacitor (C2) to parallel to the secondary coil as shown in Fig. 4, because of the high-quality factor (QParallel = RL/ωL2) at a low-frequency operation (Ahn et al., 2015). And spiral circular coils are applied for a planar WPT. The result of the L-section circuit is used in this WPT because its resistive losses are less than the resistive losses of π- and T-section circuits (Pozar et al., 2012). Finally, we also show the resistive losses of two coils in the equivalent circuit because these values are the important factors which determine the efficiency of the WPT.

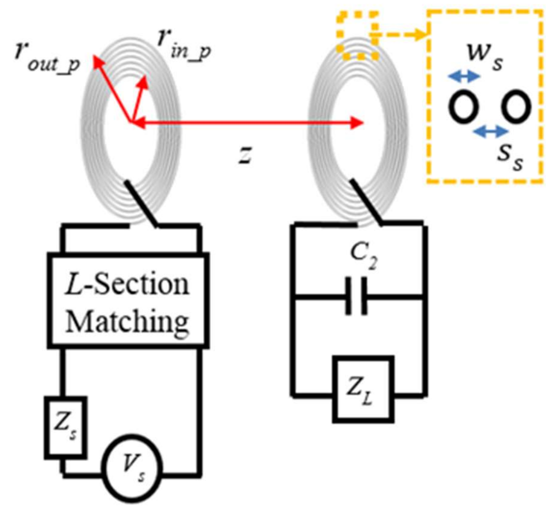

Figure 7 The proposed structure.

2. Electrical Parameters

To start the design of the proposed structure, the electrical parameters of the two-coil side in Fig. 7 must be calculated. Let r_{out}, r_{in}, w, s, z, and N are the outer radius of the coil, the inner radius of the coil, a diameter of the conductor, line separation, transfer distance, and a number of turns. The equivalent circuit of Fig. 7 can be shown in Fig. 8. Z_L is a complex load ($R_L + jX_L$).

The resistances (R_1 and R_2), the mutual inductance (M), the self-inductance (L_1 and L_2), and the secondary capacitance (C_2) are described below.

1. R_1 and R_2 can be calculated from Eq. (1) (Hui et al., 2014)

$$R_{1,2} = \frac{\rho l}{\pi (w/2)^2}\frac{w}{2\delta\left(1-e^{-\frac{w}{\delta}}\right)} \quad (1)$$

Where δ is the skin depth, $\delta = \sqrt{(\rho/\pi\mu_0 f)}$, ρ is the resistivity of copper (1.68×10^{-8} Ω.m), μ_0 is the free space permeability constant ($4\pi\times10^{-7}$ H·m^{-1}), and l is the length of the conductor, $l = \pi N(2r_{in} + wN - w)$.

2. M can be calculated as shown below. (Raju et al., 2014)

$$M = \left(\frac{4}{\pi}\right)^2 \sum_{i=1}^{i=N_p} \sum_{j=1}^{j=N_s} M_{ij} \qquad (2)$$

Where N_p is number of primary turns and N_s is number of secondary turns;

$$M_{ij} = \frac{\mu_0 \pi a_i^2 b_j^2}{2\left(a_i^2 + b_j^2 + z^2\right)^{\frac{3}{2}}} \cdots$$

$$\cdots \begin{pmatrix} 1 + \frac{15}{32}\gamma_{ij}^2 + \frac{315}{1024}\gamma_{ij}^4 \\ + \frac{15015}{65536}\gamma_{ij}^6 \end{pmatrix} \qquad (3)$$

$$a_i = r_{out\_p} - (i-1)\left(w_p + s_p\right) - \frac{w_p}{2} \qquad (4)$$

$$b_j = r_{out\_s} - (j-1)(w_s + s_s) - \frac{w_s}{2} \qquad (5)$$

$$\gamma_{ij} = \frac{2a_i b_j}{a_i^2 + b_j^2 + z^2} \qquad (6)$$

3. L_1 and L_2 are obtained as shown in Eq. (7). (Mohan et al., 1999)

$$L = \frac{\mu_0 N^2 (r_{out} + r_{in})}{2}\left[\ln\left(\frac{2.46}{\varphi}\right) + 0.2\varphi^2\right] \qquad (7)$$

$$\varphi = \frac{r_{out} - r_{in}}{r_{out} + r_{in}} \qquad (8)$$

4. C_2 is calculated as shown in Eq. (9) to maximize the load voltage.

$$C_2 = \frac{1}{L_2 \omega^2} \qquad (9)$$

The electrical parameters as stated above are used to calculate the reflected impedance Z_P as shown in Eq. (10).

$$Z_P = \alpha + j\beta \qquad (10)$$

Where,

$$\alpha = R_1 + \frac{\omega^2 M^2 (R_2 + Y)}{A} \qquad (11)$$

$$\beta = \omega L_1 - [\tfrac{\omega^2 M^2}{A} \cdots$$

$$\cdots \frac{\left(\omega L_2 - \omega C_2 R_L Y + \frac{(X_L - \omega C_2 X_L^2)Y}{R_L}\right)}{A}] \qquad (12)$$

$$A = (R_2 + Y)^2 + \cdots$$

$$\cdots \left(\omega L_2 - \omega C_2 R_L Y + \frac{(X_L - \omega C_2 X_L^2)Y}{R_L}\right)^2 \qquad (13)$$

$$Y = \frac{R_L}{(1 - \omega C_2 X_L)^2 + \omega^2 C_2^2 R_L^2} \qquad (14)$$

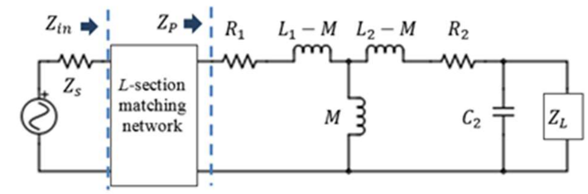

Figure 8 The equivalent circuit of the proposed structure.

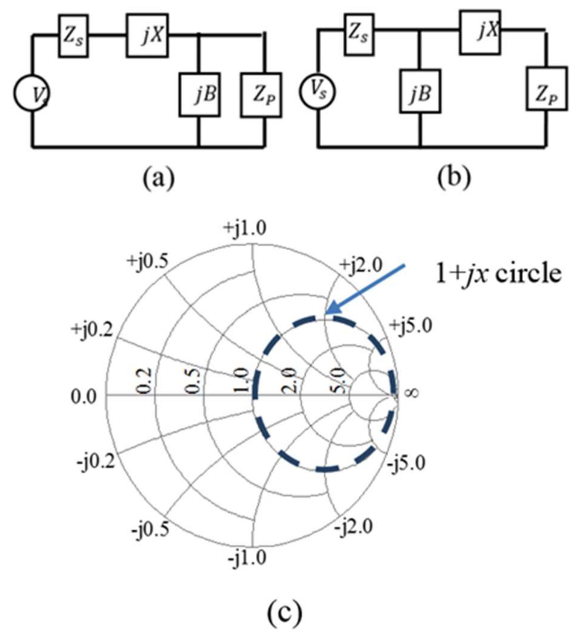

Figure 9 The two possible *L*-section matching circuits (a) Network Z_p/Z_s inside the 1+*j*x circle. (b) Network for Z_p/Z_s outside the 1+*j*x circle. (c) The impedance 1+*j*x circle on the Smith chart.

3.THEORY

From Fig. 8, the IM condition (Z_s^*- Z_{in} = 0) is commonly used to maximize the input power. The intrinsic impedance of the RF source is defined as Z_s. The circuit of Fig. 8 can be presented as two possible matching circuits as shown in Fig.9(a) and 9(b).

Accordingly, a suitable circuit must be selected and then a reactance X and a susceptance (B) for achieving the IM condition are calculated (Zhang et al., 2014). Firstly, we calculate the normalized reflected impedance z_p (Z_p/Z_s). If z_p is inside the 1+*jx* circle on the Smith chart of Fig. 9(c), then the circuit of Fig. 9(a) is used.

$$X = \frac{1}{B} + \frac{\beta Z_s}{\alpha} - \frac{Z_s}{B\alpha} \qquad (15)$$

$$B = \frac{\beta \pm \sqrt{\alpha/Z_s}\sqrt{\alpha^2 + \beta^2 - \alpha Z_s}}{\alpha^2 + \beta^2} \qquad (16)$$

Also, if z_p is outside the 1+jx circle on the Smith chart of Fig. 9(c), then the circuit of Fig. 9(b) is used.

$$X = \pm\sqrt{\alpha(Z_s - \alpha)} - \beta \qquad (17)$$

$$B = \pm\frac{1}{Z_s}\sqrt{(Z_s - \alpha)/\alpha} \qquad (18)$$

From Eq. (15) to (18), a positive X implies an inductor and a negative X implies a capacitor, while a positive B implies a capacitor and a negative B implies an inductor (Pozar et al., 2012).

To demonstrate the design processes clearly, the design is summarized as the flowchart as show in Fig. 10.

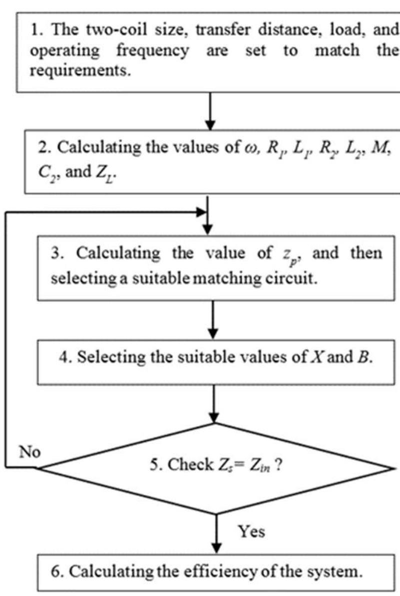

Figure 10 Flowchart of design.

4. Calculation and Experiment

In this section, the physical parameters as shown in Fig. 7 are required as follows: z = 9 cm, $r_{out\_p} = r_{out\_s}$ = 8 cm, $r_{in\_p} = r_{in\_s}$ = 6.5 cm, $w_p = w_s$ = 1 mm, $s_p = s_s$ = 0.2 mm, and $N_p = N_s$ = 10 turns. The RF source voltage is set to be 20 V with the intrinsic impedance Z_s = 50 Ω, and the operating frequency is set to be 20 kHz because the RF source is efficient. A load is assumed to be 25 Ω. The calculated electrical parameters using Eq. (1) - (10) are shown in Table 1.

The normalized reflected impedance z_p is outside the 1+jx circle on the Smith chart, so the circuit of Fig. 9(b) is used. Then, from Eq. (17) two reactances X are calculated as 1.8051 Ω and -8.9521 Ω, while two susceptances B are calculated as 0.1837 Ω^{-1} and - 0.1837 Ω^{-1} by using Eq. (18). Next, the system has two matching circuits as shown in Fig.11(a) and 11(b), where the parameters of Fig.11(a)-11(b) are shown in table 2.

Table 1 The electrical parameters

Parameter	Value
$L_1 = L_2$ (μH)	28.89
$R_1 = R_2$ (Ω)	0.11
M (μH)	4.3733
C_2 (μF)	2.192
Z_p (Ω)	0.5854+j3.5735
$z_p = Z_p/Z_s$ (Ω)	0.0117+j0.0715

Table 2 Parameters of the matching circuits

Parameter	Value
L_s (μH)	14.365
C_p (μF)	1.4622
L_p (μH)	43.309
C_s (μF)	0.89

From Fig. 11(c), solution 1 is required to connect to the system because its bandwidth is significantly better than of the solution 2 (Pozar et al., 2012, Raju et al., 2014). Hence, an equivalent circuit of the design can be illustrated by Fig. 12.

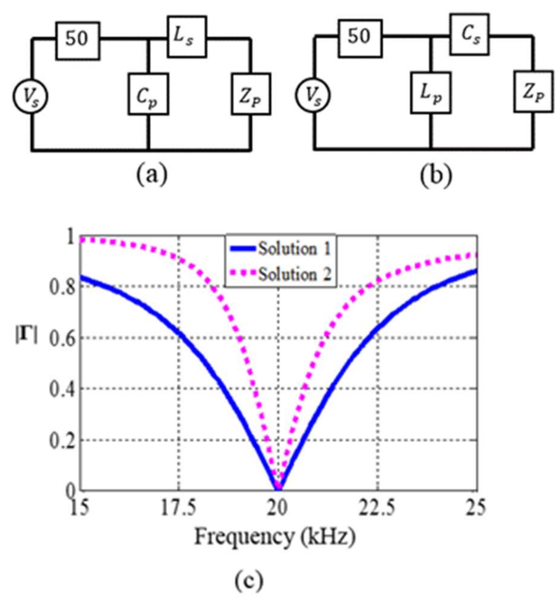

Figure 11 Two matching circuits: (a) solution 1 (b) solution 2 (c) reflection coefficient magnitude |Γ| versus frequency.

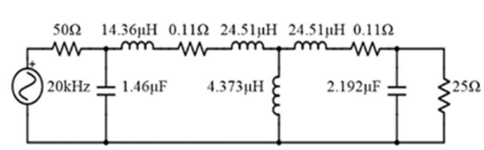

Figure 12 An equivalent circuit model of the design.

The input impedance Z_{in} of the system is calculated as 50.02 Ω using (19) so that the system achieves the IM condition. Then *Z*- and *ABCD*-parameter matrices as shown in Eq. (20) - (21) are used.

$$Z_{in} = Z_{11} - \frac{Z_{12}Z_{21}}{Z_{22}+Z_L} \qquad (19)$$

Where,

$$\begin{bmatrix} Z_{11} & Z_{12} \\ Z_{21} & Z_{22} \end{bmatrix} = \begin{bmatrix} \frac{A_a}{C_c} & \frac{A_aD_d - B_bC_c}{C_c} \\ \frac{1}{C_c} & \frac{D_d}{C_c} \end{bmatrix} \qquad (20)$$

$$\begin{bmatrix} A_a & B_b \\ C_c & D_d \end{bmatrix} = \begin{bmatrix} 1 & j\omega L_p \\ j\omega C_s & 1-\omega^2 L_p C_s \end{bmatrix} \cdots$$

$$\cdots \begin{bmatrix} 1 & R_1 + j\omega L_1 \\ 0 & 1 \end{bmatrix} \begin{bmatrix} 0 & -j\omega M \\ \frac{-j}{\omega M} & 0 \end{bmatrix} \cdots$$

$$\cdots \begin{bmatrix} 1 & R_2 + j\omega L_2 \\ 0 & 1 \end{bmatrix} \begin{bmatrix} 1 & 0 \\ j\omega C_2 & 1 \end{bmatrix} \qquad (21)$$

The efficiency of the system can be calculated as 67 % by using Eq. (22) (Pozar et al., 2005).

$$\eta = \frac{Re\{Z_L\}}{Re\{Z_{in}\}} \left| \frac{Z_{21}}{Z_{22}+Z_L} \right|^2 * 100 \qquad (22)$$

An experiment is conducted and set up according to the circuit in Fig. 12, which is illustrated in Fig. 13.

Table 3 Current, voltage signal and efficiency

	I_{in} (A)	Z_{in} (Ω)	V_L (V)	η (%)
Calculation	0.4∠0°	50∠0°	11.244∠-83°	67
Experiment	0.41∠-3°	48.78∠3°	10.1∠-71°	60

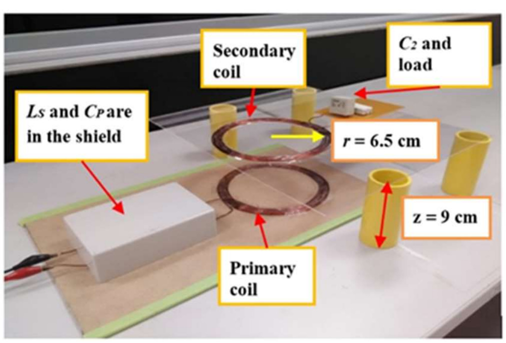

Figure 13 Experimental setups with C2 ≈ 2.2 µF, ZL = 25 Ω, as well as CP ≈ 1.5 µF and LS ≈ 15 µH in the shield chassis, and η = 60 %.

The input current and load voltage signals of the experiment are measured as shown in Table 3 and Fig. 14.

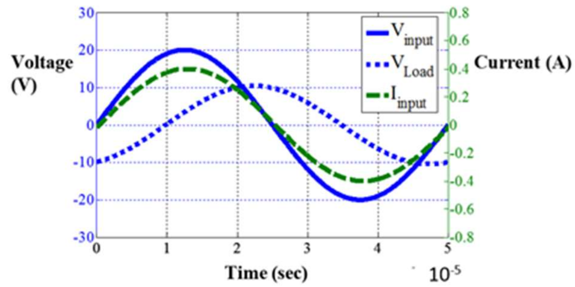

Figure 14 The measured Iin, Vin, and VL from the experiment.

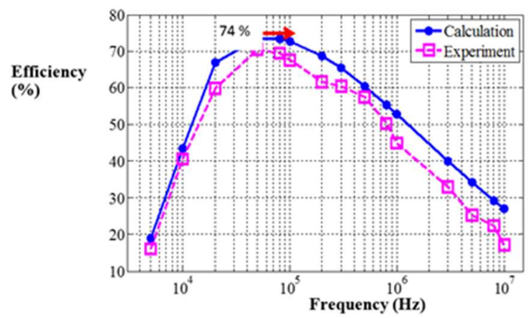

Figure 15 The efficiency of the system versus the frequency.

Fig. 15 shows a 3° phase shift between the input current and voltage, and the input impedance Z_{in} is equal to 48.78∠3° Ω. The experiment is approximately closed to the IM condition. This is due to the parasitic losses of the circuit and devices. Furthermore, the system is also conducted by varying the frequencies in the range from 5 kHz to 10 MHz, while also maintain the IM condition as shown in Fig. 12. The maximum efficiency is equal to 74 % at the frequency of 50 kHz.

From the results and the circuit of Fig. 12, the proposed structure can operate at low frequencies which are less than the critical frequency of 250 kHz for underwater WPT system, while maintaining high efficiency (the maximum efficiency is 74 % at 50 kHz) without an optimal parameter. However, the transfer distance is in the short range of 9 cm so that it is easy to control the magnetic flux along the transfer distance.

5. Conclusion

Most of the WPT structures proposed are the SR structure and the strong coupling structures under the IM condition using an optimal parameter, but an optimal parameter (fixed value) limits the design. In addition, they operate at a high frequency of several MHz to GHz. Unfortunately, the high-frequency RF sources are usually inefficient and difficult to implement, and the high-frequency operation is well-known to cause several problems, especially for the underwater WPT system. Therefore, to obtain low-frequency operation is the main goal of this paper while it is still maintaining the high efficiency and under the IM condition without an optimal parameter. To compare to the standard design approach, the efficiency of the matching networks designed by using the implemented approach is observed that the significant improvements for efficiency are possible. These improvements are validated by extensive simulations and experiment. Lastly, in this paper, we show that the proposed structure can operate at a low frequency under the IM condition using *L*-section matching with high efficiency using parallel C_2. In addition, the planar coils are a more effective candidate for a low-profile and small-footprint WPT system, especially the underwater WPT system.

6. Acknowledgment

This work was supported financially by the Master Scholarship from Thammasat School of Engineering, Thammasat University and the Ph.D. Scholarship from Thammasat University, The authors would like to thank the Quantum Technology and Energy Research Group, Thammasat University, for the technical supports.

7. References

Ahn, D. and Hong, S. (2015). Wireless Power Transfer Resonance Coupling Amplification by Load-Modulation Switching Controller. *IEEE Transactions on Industrial Electronics, 62*(2), 898 - 909. https://doi.org/10.1109/TIE.2014.2336627

Beh T. C., Kato M., Imura T., Oh S., and Hori Y. (2013).Automated Impedance Matching System for Robust Wireless Power Transfer via Magnetic Resonance Coupling. *IEEE Transactions on Industrial Electronics*, 60(9), 3689-3698. https://doi.org/10.1109/TIE.2012.2206337

Choi S. Y., Gu B. W., Jeong S. Y., and Rim C. T. (2015). Advances in Wireless Power Transfer Systems for Roadway Powered Electric Vehicles. IEEE J. Emerg. Sel. *Topics Power Electron*., 3(1), 18 - 36. https://doi.org/10.1109/JESTPE.2014.2343674

Dou, Y., Zhao, D., Ouyang, Z., and Andersen, M.A.E. (2019). Investigation and Design of Wireless Power Transfer System for Autonomous Underwater Vehicle. *In Proceedings of the 2019 IEEE Applied Power Electronics Conference and Exposition (APEC)*, 17(2), 3144–3150. https://doi.org/10.1109/APEC.2019.8721879

Fu M., Zhang T., Zhu X., and Ma C. (2013). A 13.56 MHz wireless power transfer system without impedance matching networks. Proc. *WPTC*, 222–225. https://doi.org/10.1109/WPT.2013.6556923

Han Y., and Perreault D. J. (2006). Analysis and Design of High Efficiency Matching Networks. *IEEE Transactions on Power Electronics,* 21(5),484-1491. https://doi.org/10.1109/TPEL.2006.882083

Hui, S. Y. R. Zhong, W. and Lee, C. K. (2014). A Critical Review of Recent Progress in Mid-Range Wireless Power Transfer. *IEEE Transactions on Power Electronics*, 29(9),4500-4511. http://dx.doi.org/10.1109/TPEL.2013.2249670

Jang Y. J., Suh E. S., and Kim J. W. (2016). System Architecture and Mathematical Models of Electric Transit Bus System Utilizing Wireless Power Transfer Technology. *IEEE Syst. J*., 10(2), 495-506. https://doi.org/10.1109/JSYST.2014.2369485

Jolani, F. Yu, Y. and Chen, Z. (2014). A Planar Magnetically Coupled Resonant Wireless Power Transfer System Using Printed Spiral Coils. *IEEE Antennas and Wireless Propagation Letters*, 13, 1648-1651. https://doi.org/10.1109/LAWP.2014.2349481

Kim, J., Kim, K., Kim, H., Kim, D., Park, J., and Ahn, S. (2019). An Efficient Modeling for Underwater Wireless Power Transfer Using Z-Parameters. IEEE Trans. *Electromagn. Compat*, 61, 2006–2014. http://dx.doi.org/10.1109/TEMC.2019.2952320

Kumar Ashish, Sinha Sreyam, Sepahvand Alihossein. And Afridi Khurram K. (2018). Improved Design Optimization for High-Efficiency Matching Networks. *IEEE Transactions on Power Electronics*, 33(1). https://doi.org/10.1109/TPEL.2017.2670640

Li S., and Mi C. C. (2015). Wireless power transfer for electric vehicle applications. IEEE J. Emerg. Sel. *Topics Power Electron*., 3(3), 4-17. https://doi.org/10.1109/JESTPE.2014.2319453

Lum Kin Yun, Lindén Maria, and Tan Tian Swee (2015). Impedance Matching Wireless Power Transmission System for Biomedical Device. Stud. *Health Technol. Inform*., 211,225-32. http://dx.doi.org/10.3233/978-1-61499-516-6-225

Mohan S. S., Hershenson M. D. M., Boyd S. P., and Lee T. H. (1999). Simple Accurate Expressions for Planar Spiral Inductances. *IEEE Journal of Solid-State Circuits,* 34(10),1419-1424. https://doi.org/10.1109/4.792620

Pozar, D. M. (2012). 4th Editor, Microwave Engineering. New Jersey. John Wiley and Sons, Inc. Raju S. Wu,

R. Chan M. and Yue C. P. (2014). Modeling of Mutual Coupling Between Planar Inductors in Wireless Power Applications.*IEEE Transactions on Power Electronics*, 29(1), 481-490. https://doi.org/10.1109/TPEL.2013.2253334

Ramrakhyani A.K., Mirabbasi S., and Chiao, M. (2011). Design and Optimization of Resonance-Based Efficient Wireless Power Delivery Systems for Biomedical Implants. *IEEE Transactions on Biomedical Circuits and Systems*, 5(1), 48-63. https://doi.org/10.1109/tbcas.2010.2072782

Shi, J., Li, D., and Yang, C. (2014). Design and Analysis of an Underwater Inductive Coupling Power Transfer System for Autonomous Underwater Vehicle Docking Applications. *J. Zhejiang Univ.Sci.* C 15, 51–62. https://doi.org/10.1631/jzus.C1300171

Shinohara, Naoki & Mitani, Tomohiko (2017). Impedance Matching in Wireless Power Transfer. *IEEE Transactions on Microwave Theory and Techniques*, 65(2), 1-9. https://doi.org/10.1109/TMTT.2016.2618921

Syed Agha Hassnain Mohsan, Mushtag Ali Khan, Laraba Selsabil Rokia, Asad Islam, Arfan Mahmood, and Alireza Mazinani (2020). A Review on Research Challenges, Limitations and Practical Solutions for Underwater Wireless Power Transfer. *International Journal of Advanced Computer Science and Applications 11*(8). https://doi.org/10.14569/IJACSA.2020.0110869

Thomas, E. M. Heebl, J. D. Pfeiffer, C. and Grbic, A. (2012). A Power Link Study of Wireless Non-Radiative Power Transfer Systems Using Resonant Shielded Loops. *IEEE Transactions on Circuits and Systems I: Regular Papers*, 59(9), 2125-2136. https://doi.org/10.1109/TCSI.2012.2185295

Urano, Mitsuhiro, and Akira Takahashi (2016). Study on underwater wireless power transfer via electric coupling. *2016 IEEE International Meeting for Future of Electron Devices*, Kansai (IMFEDK). https://doi.org/10.1109/IMFEDK.2016.7521674

Wang Jiale, Song Baowei, and Wang Yushan (2022). A Method to Reduce Eddy Current Loss of Underwater Wireless Power Transmission by Current Control. *Appl. Sci. 2022*, 12(5), 2435. https://doi.org/10.3390/app12052435

Yong Huang, Naoki Shinohara, and Tomohiko Mitani (2017). Impedance Matching in Wireless Power Transfer. *IEEE TRANSACTIONS ON MICROWAVE THEORY AND TECHNIQUES*, 65(2) https://doi.org/10.1109/TMTT.2016.2618921

Yan, Z., Song, B., Zhang, Y., Zhang, K., Mao, Z., and Hu,Y. A. (2019). A Rotation-Free Wireless Power Transfer System with Stable Output Power and Efficiency for Autonomous Underwater Vehicles. IEEE Trans. *Power Electron.* 2019, 34,4005–4008. https://doi.org/10.1109/TPEL.2018.2871316

Zhang, K.-H., Zhu, Z.-B., Song, B.-W.; Xu, D.-M. (2016). A Power Distribution Model of Magnetic Resonance WPT System in Seawater. *Proceedings of the 2016 IEEE 2nd Annual Southern Power Electronics Conference (SPEC),*1–4. https://doi.org/10.1109/SPEC.2016.7845532

Zhang, K.-H., Zhu, Z.-B., Du, L.-N., and Song, B.-W. (2018). Eddy Loss Analysis and Parameter Optimization of the WPT System in Seawater. J. *Power Electron*., 18, pp. 778–788. http://dx.doi.org/10.6113/JPE.2018.18.3.778

Zhang, K., Zhang, X., Zhu, Z., Yan, Z., Song, B., and Mi, C.C. (2019). A New Coil Structure to Reduce Eddy Current Loss of WPT Systems for Underwater Vehicles. *IEEE Trans. Veh. Technol*., 68, 245–253. https://doi.org/10.1109/TVT.2018.2883473

Zhang, Y. Zhao, Z. and Chen, K. (2014). Frequency Decrease Analysis of Resonant Wireless Power Transfer. *IEEE Transactions on Power Electronics*, 29(3), 1058–1063. https://doi.org/10.1109/TPEL.2013.2277783

Zhang, Y. Zhao, Z. and Chen, K. (2014). Frequency Splitting Analysis of Four-Coil Resonant Wireless Power Transfer. *IEEE Transactions on Industry Applications*, 50(4), 2436-2445. https://doi.org/10.1109/TIA.2013.2295007

Zhang, Y. and Zhao, Z. (2014). Frequency Splitting Analysis of Two-Coil Resonant. *IEEE Antennas and Wireless Propagation Letters*, 13, 400-402. https://doi.org/10.1109/LAWP.2014.2307924

NUEJ
Naresuan University
Engineering Journal

A Genetic Algorithm-Based Reversible Data Hiding Approach for Enhancing QR Code Security

Chaiyaporn Panyindee*

Department of Computer Engineering, Faculty of Engineering, Rajamangala University of Technology Rattanakosin, Nakhon Pathom, 73120, Thailand

*Corresponding author e-mail: Chaiyaporn.pan@rmutr.ac.th

(Received: 15 March 2003, Revised: 6 June 2023, Accepted: 30 October 2023)

Abstract

The problems concerning efficient RDH algorithms are often complex and involve a combination of several methods. Embedding capacity and each image require different optimum parameters. This paper presents an investigation of the parameters for the reversible data hiding algorithm for QR code images. One tool was used for finding those optimal parameters. The genetic algorithm was applied to find the weighting value and level of Expanded Variance Mean sorting that provides the lowest possible distortion for each image and each embedding capacity. Using pixel sorting before embedding is essential for modern RDH algorithms to reduce the location map size, thus allowing more information to be embedded with less distortion. The path of the threshold values of the QR code image (close to 0 and 255) was also checked to ensure the best embedding interval. The performance test for the proposed method used six QR code images (Image with the smallest and least variance to image with the largest and most variance), and the hidden bits were random. The experimental results of the proposed method show that the peak signal-to-noise ratio values are superior compared to the previous two works, averaging about 2 dB compared to LV+EMSW and 0.5 dB compared to EVM+EMSW. In the future, it should be possible to explore multi-bit embedding schemes for smooth areas that enable more embedding and still have low distortion.

Keywords: genetic algorithm, Linear multi-scale weighting, reversible data hiding.

1. INTRODUCTION

Currently, QR codes are used extensively in media applications. The information transmitted with the image QR code can be easily accessed by scanning by using a smartphone. However, some information still requires privacy, such as transaction numbers, date of birth, national ID number, etc. For this reason, reversible data hiding (RDH) techniques are considered preventing unauthorized access to top-secret information.

RDH is part of steganography, which has become popular among image processing researchers in recent years. The key condition of RDH is to restore both the original host image and message without loss. In addition, RDH methods should have a high embedding capacity, with less distortion. The main challenge faced by RDH in QR code imaging is trying to hide information in a pixel with high variance and intensity values close to the maximum and minimum without causing the Overflow and Underflow problem. The first RDH was presented by Mintzer et al. (1997). They introduced a visible embedding technique exploiting the property of reversibility of the original image. Fridrich et al. (2002) proposed a lossless compression algorithm for RDH. A least significant bit (LSB) substitution technique using an efficient entropy coder is proposed by Celik et al. (2002). Yang et al. (2004) proposed an integer discrete cosine transform (DCT) based RDH for images using a companding technique. Several RDH techniques based on integer discrete wavelet transform (DWT) are proposed by Xuan et al. (2002-2004). Zou et al. (2006) proposed a semi-fragile, lossless digital watermarking scheme based on integer DWT.

Tian (2003) introduced reversible data embedding using a difference expansion (DE). His scheme divides the image into pairs of pixels and uses each pair to hide a bit of information. Thus, his embedding capacity is at best 0.5 bits/pixel. The major problem in the original DE method was the large size of the location map, which must be included as part of the payload. Therefore, reducing the size of the location map is one of the key goals in this field. Kamstra and Heijmans (2005) improved the DE method by sorting pairs according to correlation measures facilitating compression. Kim et al. (2008) reduced the size of the location map by removing non-ambiguous parts. Their methods achieve better results when compared to Kamstra and Heijmans' method (2005). Ni et al. (2006) introduced a histogram shifting technique in the spatial domain. Thodi and Rodrıguez (2007) explored the histogram shifting (HS) method by employing prediction errors for efficiency, which is sometimes called prediction-error histogram shifting (PEHS). Sachnev et al. (2009) improved the performance of PEHS by using sorting. Kotvicha et al. (2012) improved the performance of the sorting using expand variance mean (EVM) technique base on Sachnev's algorithm etc. For the past few years, a new framework based on PEHS called pixel-value-ordering (PVO) has drawn significant interest from researchers. PVO was initially proposed by Li et al. (2013) to embed secret data into the minimum and maximum pixel values of divided image blocks. After that, Ou et al. (2014) attempted to exploit the correlation of smooth blocks, so they proposed PVO-k to modify the blocks that have the k largest or smallest pixels. In 2014, Peng et al. (2014) embedded secret data into smooth blocks by utilizing the spatial position and proposed an improved PVO (IPVO). In 2015, Wang et al. (2015) proposed a PVO method in which block sizes are dynamic. In the same year, Qu and Kim (2015) proposed a pixel-based PVO method to predict pixels one by one. In 2016, the pairwise modification was employed in PVO, and unique 2D mapping was designed according to the specific 2D PEHS by Ou et al. (2016). In subsequent years, pairwise PVO was improved by Dragoi et al. (2018), Gao et al. (2019), He and Cai (2020), and Zhang et al. (2020) to achieve better performance. In 2021, Fan et al. (2021) merged the advantages of sorting and averaging by combining IPVO and a conventional Rhombus predictor through the multi-predictor mechanism. Their method outperformed state-of-the-art PVO-based RDH methods. In the same year, Panyindee (2021) improved sorting and conventional Rhombus predictor by modifying the dynamic variance mean (DVM) sorting models and applying a fitting weight rhombus (FWR) predictor. Recently, Fan et al. (2023) proposed one-dimensional and two-dimensional flexible patch moving (FPM) modes to move the patch with adaptive step lengths to further improve the embedding performance.

Over the past few years, RDH methods (2015-2019) have been applied to QR code images, causing Overflow and Underflow problems because the pixels in QR code images are the highest and lowest values (255 and 0). To solve this problem, Panyindee et al. (2019) proposed the linear multi-scale weighting (LMSW) technique; their approach achieves several embedding capacities. Another problem with QR code images is that the pixel texture is highly variable. As a result, the use of local variance sorting is insufficient for correct pixel sorting (Low PE should be before high PE). In the same year, Panyindee et al. (2019) applied the EVM technique together with the LMSW technique based on PEHS, their method achieved PSNR results superior to previous methods, especially with small payload embedding.

However, when a RDH algorithm (2019) combines several methods together, there are several parameters that must be repeated (find) in many parts, such as weighting value (W), threshold values (T_n, T_p), EVM value (S) in order to get the best possible PSNR result. Their parameter search uses step-by-step tuning for each embedding capacity, which is difficult because many parameters must be searched simultaneously as unknown. In this paper, GA was used to find the optimal parameters for each image and each embedding capacity. Our results provide low distortion and achieve PSNR values that are superior to the two previous works.

The rest of the paper is arranged as follows. Section 2 discuss the analyze the modifying pixels using PEHS + sorting for QR code images problem. Section 3 describes the proposed method. Section 4 shows the experimental results and concluding remarks are given in the final section.

2. Analyze The Overflow Problem Of QR Codes

Several predictors based on PEHS (2007) were proposed to reduce distortion significantly, such as median edge detector predictor (MED) (2007) and (2009), the gradient-adjusted predictor (GAP) (2011), the rhombus predictor (2019), accurate predictor (2012), PDE predictor (2013), Gaussian weight predictor (2016), etcetera. PEHS encoding can be calculated as follows.

$$D_{i,j} = \begin{cases} 2d_{i,j} + b, & \text{if } d_{i,j} \in \left[T_n; T_p\right] \\ d_{i,j} + T_p + 1, & \text{if } d_{i,j} > T_p \text{ and } T_p \geq 0 \\ d_{i,j} + T_n, & \text{if } d_{i,j} < T_n \text{ and } T_n < 0 \end{cases} \tag{1}$$

Where d is the PE value. b is the embedded data bit (i.e., 0 or 1). T_n is the negative threshold value. T_p is the positive threshold value. The determination of the T_n and T_p range directly affects the embedding capacity, and the obtained PSNR values. Therefore, the range of T_n and T_p should fit the required payload size. Conversely, if Tn and T_p are extended more than necessary, the PSNR is dropped. PEHS decoding was calculated by equations (2) and (3).

$$d_{i,j} = \begin{cases} \left\lfloor D_{i,j} / 2 \right\rfloor, & \text{if } D_{i,j} \in \left[2T_n; 2T_p + 1\right] \\ D_{i,j} - T_p - 1, & \text{if } D_{i,j} > 2T_p + 1 \text{ and } T_p \geq 0 \\ D_{i,j} - T_n, & \text{if } D_{i,j} < 2T_n \text{ and } T_n < 0 \end{cases} \tag{2}$$

$$b = D_{i,j} \bmod 2, \quad D_{i,j} \in [2T_n; 2T_p + 1] \tag{3}$$

Analyzes of a recent problem of RDH base on PEHS for QR code images, where the gray-scale values were the highest and lowest as shown in Figure 1.

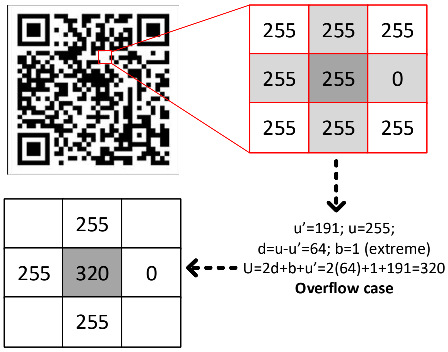

Figure 1 An example of the overflow problem after data embedding using PEHS.

These pixels often caused Overflow and Underflow problems after the modified pixels using condition (4).

$$0 > U = 2d + b + u' > 255 \tag{4}$$

Panyindee et al. (2019) introduced a LMSW technique to create free space for each size of embedding data, but still able to scan and access the data. The weighting (W) value can be calculated as Equation (5).

$$W = \frac{255 - C}{P_{MAX}} \quad ; \quad C \in \{1,2,3,\ldots,255\} \tag{5}$$

Where C is the ascending constant, P_{MAX} is the maximum gray-level intensity, I_m is an original QR code image and the weighted image I_w can be calculated as

$$I_W = \lceil W \times I_m \rceil \tag{6}$$

Their approach makes it possible to hide information in QR code images by a PEHS method. However, finding the ideal W parameter of the RDH algorithm for each image and each embedding size is still necessary and must be investigated.

Another enhancement of the sorting process of RDH algorithm (2019), is that the static sorting technique (local variance (2009)) that has been replaced by an adaptive sorting technique (EVM (2012)). The EVM is applied to get the correct sequence of PE values in each QR code image and each embedding size. EVM can be calculated as follows.

$$\overline{\mu}_{i,j}^{S} = \frac{\sum_{l=-\lfloor S/2 \rfloor}^{\lfloor S/2 \rfloor} \mu_{i+l,j+l} + \sum_{k=1}^{\lfloor S/2 \rfloor} \sum_{l=-\lceil S/2 \rceil}^{\lceil S/2 \rceil - 2k} (\mu_{i+l,j+l+2k} + \mu_{i+l+2k,j+l})}{2\lceil S/2 \rceil^2 + 2\lceil S/2 \rceil + 1 - 4(S \bmod 2)} \tag{7}$$

Where μ is the local variance. S is the degree of expanding μ. l is the length radius of the mask. Note, that the correct PE sequencing significantly increases the PSNR value. When a low PE is used, the post-embedded distortion remains as low as the PE itself. The QR code image looks like noise. Experiments have shown that the dynamic data sorting techniques produce excellent results, especially with highly variable images.

Two previous RDH solutions for QR code images make data hiding possible. However, the consequence is that their work has more parameters that must be searched for optimal results. Thus, a tool to find the optimal parameters became necessary to get as close to the best possible results. In this work, GA was considered.

3. THE PROPOSED METHOD

From solving the RDH problem for the QR code image to the improvement of the embedding method, an algorithm (2019) that combines techniques such as PEHS, EVM, Two-pass tasting (TPT), Double Embedding for QR code images was investigated to get the parameters that achieve the highest possible PSNR value. In this work, GA is applied to find those suitable parameters. GA is an ideal tool for finding optimal solutions using natural selection or natural evolution. Moreover, default parameters are also set using the best parameters of the former methods to ensure that the results are not worse than the previous methods. An overview of the application of GA in combination with the RDH algorithm is shown in Figure 4. To ensure the efficacy of the proposed method, six QR code images representing the smallest image with the least variance to the largest image with the greatest variance were used for testing. The data bits used for embedding were random, starting with 10,000 bits then increasing to 20,000 bits and 30,000 bits, respectively, until embedding was not possible. The measurement tools use PSNR and MSE values, which are standard formats for RDH work.

GA is a method for solving both unconstrained and constrained optimization problems based on natural selection, the procedure that runs biological evolution. GA repeatedly modifies a population (or chromosomes) of individual solutions. In each step, GA selects individuals from the current population to serve as parents and uses them to produce children for the subsequent generation. Over successive generations, the population evolves into the best solution. GA has parameters known as "gene" and "chromosome". Long genes produce efficient information exchange results. Our chromosome was a row of binary numbers which consists of two genes, as shown in Figure 2.

$b_{m_W-1}b_{m_W-2}\ldots b_{0_W}$	$b_{m_S-1}b_{m_S-2}\ldots b_{0_S}$
gene1=W	gene2=S

Figure 2 A chromosome in GA consists of two genes.

Binary numbers can be changed to decimal numbers by using equation (8)

NUEJ
Naresuan University
Engineering Journal

$$decimal = l_b + (u_b - l_b)(\sum_{i=1}^{m} 2^{i-1} b_{i-1}) / (2^m - 1) \quad (8)$$

Where u_b is the upper bound parameter. l_b is the lower bound parameter. m is the number of bits used for each gene. b_{i-1} is a binary value of i^{th}, after creating n rows of different chromosomes. An objective function (Sometimes called the fitness function) is defined as the mean square error (MSE) calculated as equation (9).

$$MSE = \sum_{i=1}^{N} \sum_{j=1}^{M} \left| u_{i,j} - U_{i,j} \right|^2 / (N \cdot M) \quad (9)$$

MSE is the total error between the original image and the embedded image. GA will search for W, and S which has the minimum MSE in each image and each required payload. To increase the performance of GA, the scope of the parameters is defined: by setting the default weight W_{Init} = 0.992, while the maximum weighting is W_{max} = 0.921, which is superior for large data embedding. For T_n and T_p are determined at -1 and 0, respectively, according to the required payload size. Note, that the histogram of prediction error of QR code images is not Laplacian, as shown in Figure 3. Most PE values in the first layer (cross layer) were 0 whereas in the next layer (dot layer) the PE value graph dropped rapidly as the pixels in the cross layer were already embedded and used to make predictions in the dot layer. This embedding process, called Double Embedding (2009), which can be effectively used with the rhombus predictor and sorting techniques. The combination of many techniques allows the embedding of a large payload to be possible. Another note, for most PE values in the dot layers found are 0 and -1 drop down, which directly affected the high-distortion after the embedded data had been extracted. It became the reason that threshold values were fixed at those two values. The last parameter is S, from the test, S_{max} = 64 is enough for the extreme version of the QR code image (i.e., version 40). All the reasons mentioned above will help GA run faster.

The next step will be chromosomal enhancement using three steps of a genetic operation: Selection, Crossover, and Mutation as shown in Figure 4, which also shows an overview of the system. After all operations are completed, the next generation of chromosomes is regenerated. New chromosomes often provide better or equal fitness values. Although the algorithm cannot guarantee that the best results will be found, it will approach the best potential value. Sometimes the number of generations is another important factor to get the best results.

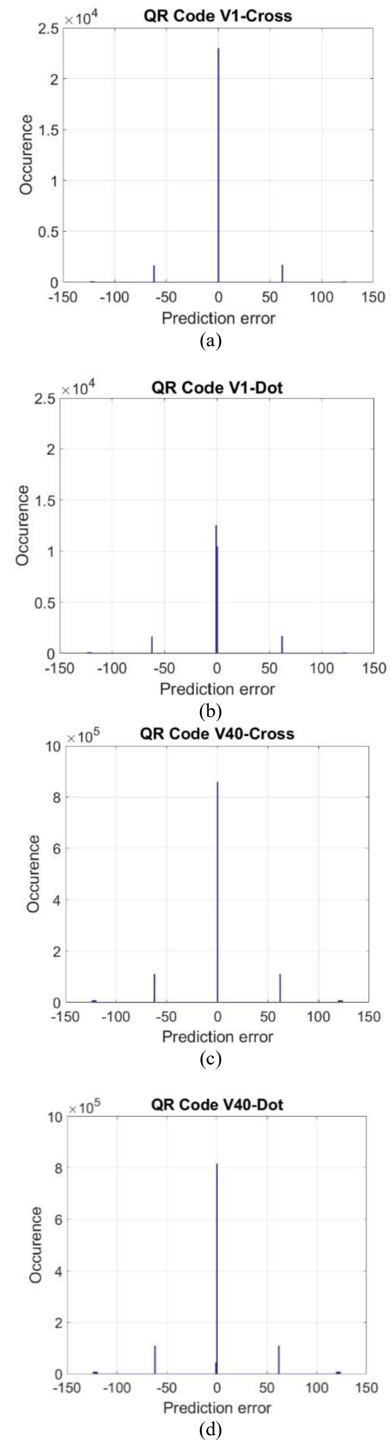

(a) (b) (c) (d)

Figure 3 (a), (c) shows histogram of rhombus predictor PEs in cross-layer and (b), (d) shows histogram of rhombus predictor PEs in dot-layer of the three QR Code images.

To reduce embedding distortion, all pixels are examined status by the TPT definition (2016), which are separated into seven sets: *EE*, *ES*, *SS*, *E*, *S*, *NE*, and *NS*. Where $EB(T_n,T_p)$ is an embeddable set while $LM(T_n,T_p)$ is a non-embeddable set and must be mapped and are defined as:

$$EB(T_n,T_p) = \{(i,j) \in EE \cup ES,\} \quad (10)$$

$$LM(T_n,T_p) = \{(i,j) \in E \cup S \cup NE \cup NS\} \quad (11)$$

Therefore, the number of pixels that can be embedded is equal to the number of *LM* plus the number of the payload, as in Equation (12).

$$n\left(EB(T_n,T_p)\right) = n\left(LM(T_n,T_p)\right) + n\left(Payload\right) \quad (12)$$

Detailed encoding and decoding algorithms are described as follows.

3.1 Encoding Algorithm

1. Start for GA by the initial population setting at *n* chromosomes (*W* and *S*).

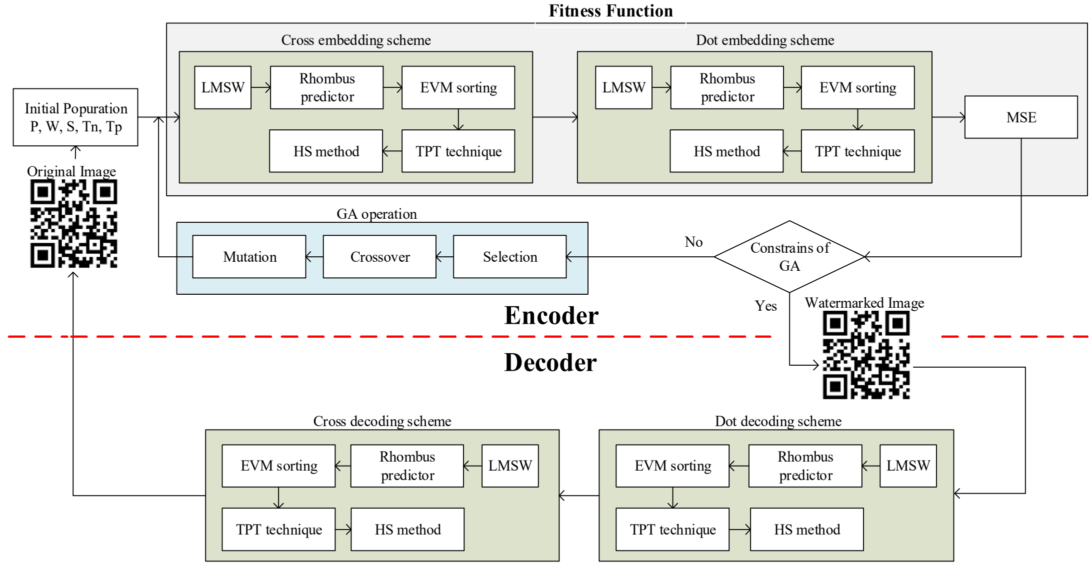

Figure 4 Block diagram for encoding and decoding algorithms using GA.

2. Convert all values to binary from decimal numeric parameters using equation (8).
3. Determine the cross and dot layer position in the QR code image according to Sachnev et al. (2009).
4. Each layer is calculated as follows.
   4.1 Starting from the position in the cross layer, calculated as follows:
      4.1.1 the prediction value $u' = floor[(v_{i,j-1} + v_{i,j+1} + v_{i-1,j} + v_{i+1,j})/4]$ and $d = u - u'$.
      4.1.2 Sort all pixels according to the EVM technique using Equation (7).
   4.2 Check the embedding area (Count the number of sets *EB* and *LM*) using Equation (12) until the desired position is obtained, but if not found, go to step 1 again.
5. For each chromosome that was previously collected, let start embedding and calculate the results following steps 5.1-5.5.
   5.1 Keep the LSB of the first h pixel and replace it with a header file for data recovery.
   5.2 Store the location map using Equation (11) and insert the LSB from the previous step into a request payload.
   5.3 Embed data using equation (1) and modified pixel value $U_{i,j} = u'_{i,j} + D_{i,j}$.
   5.4 Apply the above steps in a dot layer.
   5.5 Calculate the *MSE* value using Equation (9).
6. If GA is run up to the last generation, the lowest MSE received in that current generation, that is the best fitness value.

For data recovery, it is necessary to have the parameters transmitted from the encoding process to the decoder, which are stored in the header file as: 10 bits for a weighted value *W*, 6 bits for an expansion level *S*, 2 bits for a negative threshold T_n, 2 bits for a positive threshold T_p, and 21 bits for the size of a request payload *P*, a total of 41 bits. The decoding process is as follows.

3.2 Decoding Algorithm

1. Separate all positions in the embedded QR code image into crosses and dot layers according to their encoding.
2. Extract the LSB of the first *h* pixel of header file in the dot layer and convert all parameters (W, T_n, T_p, S and P) from binary to decimal using equation (8).
3. Calculate the *EVM* of every pixel and sorts them in ascending order.

4. Calculate prediction values and PE values of all pixels using the rhombus predictor and Equation (2) respectively.

5. Check the status of each PE values and threshold values from a previously header file using definition 2 in TPT.

6. Separate pixels that are *EE* and *ES* sets sequentially to restore the original pixels using Equation (3) and replace the original LSB of the header file back to the first *h* pixel.

7. Repeat steps 2 - 6 in the cross layer.

4. Experimental Results

In the experiment, six different versions of the QR code image were used to test the effectiveness of the proposed method, which was created online by Nayuki (2021) and set the standard according to LV+LMSW (2019) as shown in Figure 5. Note that all six images were RGB color images with the same gray-scale for all three planes, so the embedding performance test used only one plane. All processes were tested by using a PC CPU Core I7-7700 HQ 2.8 GHz, 4 GB RAM, 256 GB HDD on Windows 10 Pro 64 bit operating system, processed by using MATLAB version R2016a. The PNSR value was used to measure the performance of the proposed method, which was calculated as follows.

$$PSNR = 10\log_{10}\left(\frac{255^2}{MSE}\right) \qquad (13)$$

Several randomized bits were used in testing by starting at 10k bits and increasing to 20k, 30k, respectively, until reaching the final size that could still be embedded. The

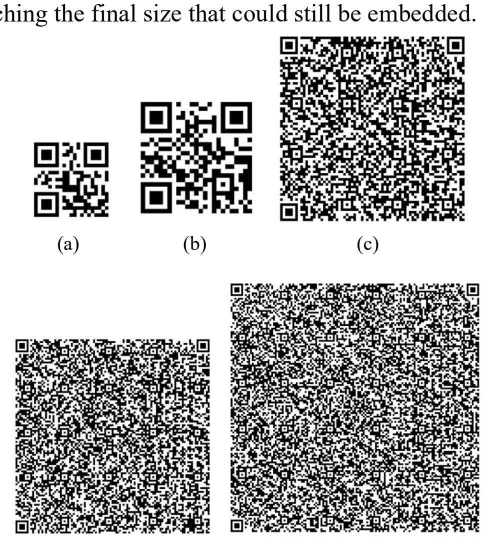

(a) (b) (c)

(d) (e)

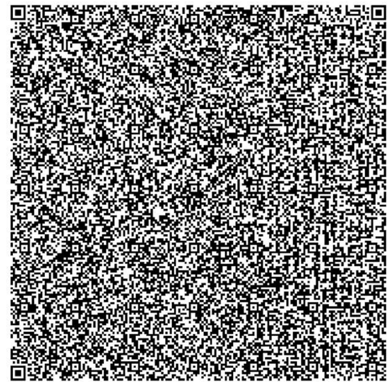

(f)

Figure 5 Test images: (a) QR Code V1 size 232 x 232 pixels, (b) QR code V2 size 264 x 264 pixels, (c) QR code V14 size 648 x 648 pixels, (d) QR code V22 image size 904 x 904 pixels, (e) QR code V31 image size 1192 x 1192 pixels, (f) QR code V40 size 1480 x 1480 pixels.

parameters *W* and *S* for each image and each embedding size investigated by GA are shown in Table 1. Note that image size and pixel variability affected the size of the embedding. In the image, the QR code V1 could only embed a maximum of approximately 30k bits, while the QR code V40 could embed data up to around 1,160k bits. However, the average bit-embedding rate of all six images remained about 0.5 bpp.

The proposed method provided superior PSNR results than two previous methods (2019) for almost every size of the payload with six QR code images, as shown in Figure 6. The combination of GA+EVM+LMLW based

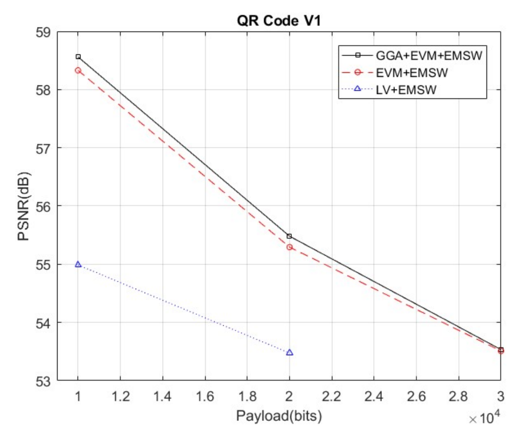

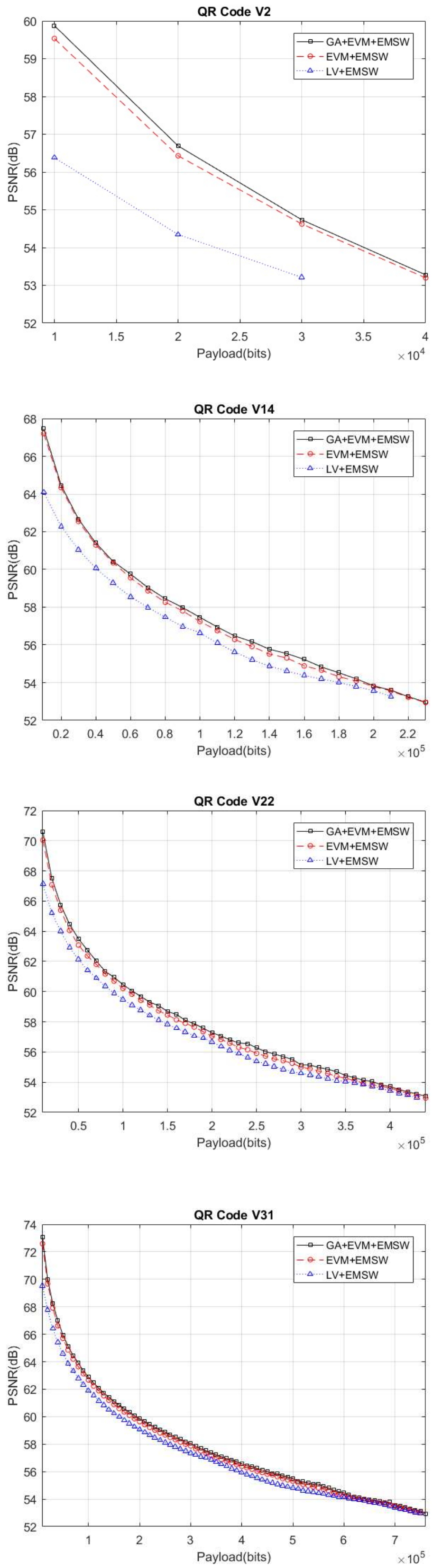

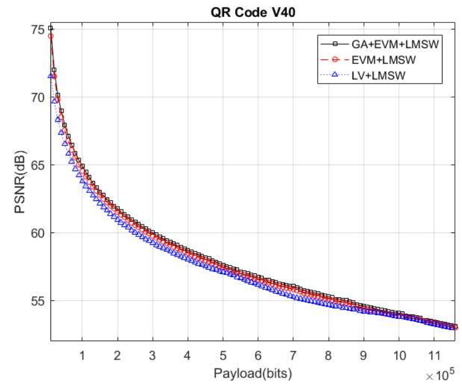

Figure 6 Graphs showing PSNR VS Payload values of the proposed method (GA+EVM+LMSW) compared with two previous methods (EVM+LMSW) and (LV+LMSW) for the six different QR code images.

on PEHS achieved the best possible results in a limited range. Note that sorting techniques are essential and must be part of the RDH algorithm, especially with highly variable images, to achieve low distortion. From the experiments, dynamic sorting techniques yielded superior results to static sorting techniques. In Figure 6, the PSNR graph shows a solid black line (GA+EVM+LMSW) and a red dotted line (EVM+LMSW) comparatively above the blue dotted line (LV+LMSW), especially in the early stages of embedding at low payloads. In the footer of embedding large payloads, the PSNR graphs of the three methods were seldom different because the PE values in the dot layer were used. Although the results of the proposed method were improved by using the GA tool, the consequence was higher process complexity and a longer processing time according to the specified scope and conditions. An optimal parameter search should remain in a limited area to avoid searching unnecessary areas.

An effective prediction method is still essential for reducing distortion and size of the location maps. In the future, dynamic predictors for each image and each embedding size should be considered.

Table 1 Parameter values and PSNR values obtained from GA tested with different payload sizes for V1, V2 and V14 images.

Pay	**QR Code V1**	**QR Code V2**	**QR Code V14**
Load	***W*, *S*, PSNR**	***W*, *S*, PSNR**	***W*, *S*, PSNR**
10k	0.980, 6, 58.56	0.972, 7, 59.87	0.980, 27,67.662
40k	---	0.998, 2, 53.27	0.988, 18, 61.40
100k	---	---	0.976, 2, 57.26
300k	---	---	---
700k	---	---	---
1000k	---	---	---

Table 2 Parameter values and PSNR values obtained from GA tested with different payload sizes for V22, V31 and V40 images.

Pay Load	QR Code V22	QR Code V31	QR Code V40
	W, *S*, PSNR	*W*, *S*, PSNR	*W*, *S*, PSNR
10k	0.972, 18,70.77	0.972, 15,72.79	0.972, 10, 75.04
40k	0.980, 13, 64.30	0.972, 14,66.69	0.984, 10, 68.60
100k	0.980, 4, 60.29	0.984, 4, 62.70	0.972, 8, 64.59
300k	0.992, 3, 55.16	0.992, 2, 57.87	0.972, 4, 59.80
700k	---	0.992, 1, 53.48	0.972, 3, 55.83
1000k	---	---	0.976, 1, 53.87

4. Conclusion

A survey of the appropriate parameters of the PEHS + sorting RDH algorithm using GA and LMSW strategy in limited scope for each QR code image and each payload is presented in order to achieve the best possible results. Different payload sizes were used to test the performance of the proposed method and the previous methods. The experimental results showed that the proposed GA was superior compared to the two previous similar approaches. However, the average embedding ratio efficiency of the proposed method is still only half the image size, which should be improved. In the future, multi-bit per pixel embedding strategies for smooth regions should be exploited to embed more information while maintaining low distortion.

6. Acknowledgment

This research was supported by the Faculty of Engineering, Rajamangala University of Technology Rattanakosin (RMUTR).

7. References

Mintzer, F., Lotspiech, J. and Morimoto, N. (1997). Safeguarding digital library contents and users: digital watermarking, *D-Lib Magazine*., 3, 33-45.

Fridrich, J. Goljan, M. and Du, R. (2002). Lossless data embedding for all image formats. *Proceedings of the SPIE*., 4675, (pp. 572-583).

Celik, M. Sharma, U. G. Tekalp, A. M. and Saber, E. (2002). Reversible data hiding. *Proceedings of the IEEE International Conference on Image Processing*, 2, (pp. II/157-II/160).

Yang, B. Schmucker, M. Funk, W. Busch, C. and Sun, S. (2004). Integer DCT-based reversible watermarking for images using companding technique. *Proceedings of SPIE-The International Society for Optical Engineering*, 5306, (pp. 405-415).

Xuan, G. Chen, J. Zhu, J. Shi, Y. Q. Ni, Z. and Su, W. (2002). Lossless data hiding based on integer wavelet transform. *Proceedings of the IEEE Workshop on Multimedia Signal Processing*, (pp. 312-315).

Xuan, G. Shi, Y. Q. Ni, Z. C. Chen, J. Yang, C. Zhen, Y. and Zheng, J. (2004). High capacity lossless data hiding based on integer wavelet transform. *Proceedings of the IEEE International Symposium on Circuits and Systems*, 2, (pp. II29-II32).

Xuan, G. Yang, C. Zhen, Y. Shi, Y. Q. and Ni, Z. (2004). Reversible data hiding based on wavelet spread spectrum. *Proceedings of the IEEE 6th Workshop on Multimedia Signal Processing*, (pp. 211-214).

Zou, D. Shi, Y. Q. Ni, Z. and Su, W. (2006). A semi-fragile lossless digital watermarking scheme based on integer wavelet transform. *IEEE Trans. Circuits Syst. Video Technol*., *16*(10), 1294-1300.

Tian, J. (2003). Reversible Data Embedding Using a Difference Expansion. *IEEE Trans. Circuits Syst. Video Technol*., *13*(8), 890-896.

Kamstra, L. H. J. and Heijmans, A. M. (2005). Reversible Data Embedding into Images Using Wavelet Techniques and Sorting. *IEEE Trans. Image Process*., *14*(12), 2082-2090.

Kim, H. J. Sachnev, V. Shi, Y. Nam, Q. J. and Choo, H. G. (2008). A novel difference expansion transform for reversible data embedding. *IEEE Trans. Inf. Forensics Secur*., *3*(3), 456-465.

Ni, Z. Shi, Y. Q. Ansari, N. and Su, W. (2006). Reversible data hiding. *IEEE Trans. Circuits Syst. Video Technol*., *16*(3), 354-362.

Thodi, D. M. and Rodriguez, J. J. (2007). Expansion Embedding Techniques for Reversible Watermarking. *IEEE Trans, Image Process*., *16*(3), 721-730.

Sachnev, V. Kim, H. J. Nam, J. Suresh, S. and Shi, Y. Q. (2009). Reversible Watermarking Algorithm Using Sorting and Prediction. *IEEE Trans. Circuits Syst. Video Technol*., *19*(7), 989-999.

Kotvicha, A. Sanguansat, P. and Kasemsa, M. L. K. (2012). Expand Variance Mean Sorting for Reversible Watermarking. *Int. J. Comput. Commun. Eng*., *1*, 196-199.

Li, X., Li, B., Yang, B., & Zeng, T. (2013). General framework to histogram-shifting-based reversible data hiding. *IEEE Transactions on Image Processing*, *22*, 2181–2191.

Ou, B., Li, X., Zhao, Y., & Ni, R. (2014). Reversible data hiding using invariant pixel-value-ordering and prediction-error expansion. *Signal Processing: Image Communication*, *29*, (pp. 760–772).

Peng, F., Li, X., & Yang, B. (2014). Improved PVO based reversible data hiding. *Digital Signal Processing*, *25*, 255–265.

Wang, X., Ding, J., & Pei, Q. (2015). A novel reversible image data hiding scheme based on pixel value ordering and dynamic pixel block partition. *Information Sciences*, *310*, 16–35.

Qu, X., & Kim, H. J. (2015). Pixel-based pixel value ordering predictor for high-fidelity reversible data hiding. *Signal Processing*, *111*, 249–260.

Ou, B., Li, X., & Wang, J. (2016). High-fidelity reversible data hiding based on pixel-value-ordering and pairwise prediction-error expansion. *Journal of Visual Communication and Image Representation*, *39*, 12–23.

Dragoi, I. C., Caciula, I., & Coltuc, D. (2018). Improved pairwise pixel-value-ordering for high-fidelity reversible data hiding. *In IEEE International Conference on Image Processing,* (pp. 1668–1672).

Gao, E., Pan, Z., & Gao, X. (2019). Reversible data hiding based on novel pairwise PVO and annular merging strategy. *Information Sciences*, *505*, 549–561.

He, W., & Cai, Z. (2020). An insight into pixel value ordering prediction-based prediction-error expansion. *IEEE Transactions on Information Forensics and Security*, *15*, 3859–3871.

Zhang, T., Li, X., Qi, W., & Guo, Z. (2020). Location-based pvo and adaptive pairwise modification for efficient reversible data hiding. *IEEE Transactions on Information Forensics and Security*, *15*, 2306–2319.

Fan, G., Pan, Z., Gao, E., Gao, X., & Zhang, X. (2021). Reversible data hiding method based on combining IPVO with bias-added Rhombus predictor by multi-predictor mechanism. *Signal Processing*, 180, Article 107888.

Panyindee, C. (2021). Efficient Reversible Data Hiding Using Dynamic Variance Mean Sorting and Fitting Weight Rhombus Predictor. *Journal of Circuits, Systems, and Computers*, *30*(9), 2150169-1-2150169-17.

Fan, G., Pan, Z., Zhou, Q., & Zhang, X. (2023). Flexible patch moving modes for pixel-value-ordering based reversible data hiding methods. *Expert Systems with Applications*, *214*, 1–14.

Dangmee, P. and Lilakiatsakun, W. (2015). Steganography hiding data within QR Code. *J. Inf. Sci. Technol.*, *5*(1), 35-41.

Panyindee, C. Leelawiwat, T. and Rangsirak, P. (2019). Study and Development of a Reversible Data Hiding Algorithm Using Linear Weighting for QR Code images. *Engng. J. CMU.*, *26*(1), 80-92.

Panyindee, C. Leelawiwat, T. and Rangsirak, P. (2019). Improved Sorting in QR Code images Using EVM technique for Reversible Data Hiding. *Engng. J. CMU.*, *26*(3), 66-76.

Hu, Y. Lee, H. K. and Li, J. (2009). De-based reversible data hiding with improved overflow location map. IEEE Trans. *Circuits Syst. Video Technol., 19*(2), 250-260.

Li, X. Yang, B. and Zeng, T. (2011). Efficient reversible watermarking based on adaptive prediction-error expansion and pixel selection. *IEEE Trans. Image Process.*, *20*(12), 3524-3533.

Kang, S. Hwang, H. J. and Kim, H. J. (2012). Reversible watermark using an accurate predictor and sorter based on payload balancing. *ETRI.*, *34*(3), 410-420.

Ou, B. Li, X. Zhao, Y. and Ni, R. (2013). Reversible data hiding based on PDE predictor. *J. Syst. Softw.*, *86*(10), 2700-2709.

Panyindee, C. and Pintavirooj, C. (2016). Optimal Gaussian Weight Predictor and Sorting Using Genetic Algorithm for Reversible Watermarking Based on PEE and HS. *IEICE Trans. Info Syst.*, *E99-D* (9), 2306-2319.

Project Nayuki. (2021). *QR Code generator library*. https://www.nayuki.io/page/qr-code-generator-library.

NUEJ
Naresuan University Engineering Journal

Real-Time Root Cause Analysis of Governor Control System for Sirikit Hydropower

Uthai Kumthai[1,*] and Suttichai Premrudeepreechacharn[2]

[1] Department of Electrical Engineering Faculty of Engineering, Chiang Mai University, University, Chiang Mai, 50200 Thailand and Electricity Generating Authority of Thailand, Sirikit Dam, Uttaradit, 53190 Thailand.
[2] Department of Electrical Engineering Faculty of Engineering, Chiang Mai University, University, Chiang Mai, 50200 Thailand.

[*]Corresponding author e-mail: uthai_kumthai@cmu.ac.th, uthai.kum@egat.co.th

(Received: 28 April 2023, Revised: 1 December 2023, Accepted: 1 December 2023)

Abstract

The existing governor control system of Sirikit Hydropower is designed as a standalone system. It communicates to another system such as the distributed control system (DCS), protection system, and excitation system by hardwiring. Some abnormal events are the group alarms that cause the operator and maintenance team to spend more time on problem-solving. This paper studies real-time root cause analysis of the governor control system for Sirikit Hydropower. This real-time root cause can improve operator and maintenance team performance, especially in case of emergency and ready-to-start events. The real-time root cause analysis system knowledge is based on input/output real-time data of the governor system and DCS, maintenance instruction manual, history events, and drawing of the governor control system. The root cause analysis in this research is a fault tree logic analysis technique for diagnosing alarms and emergency events. Developing a graphical user interface is a real-time troubleshooting guide monitor with user-friendly. This system can help the operator and maintenance team to solve problems of the governor control system more effectively.

Keywords: Diagnostic, Fault Tree Logic Analysis, Governor Control System, Real-Time Root Cause Analysis, Troubleshooting guide.

1. INTRODUCTION

Nowadays, renewable energy plays an important role in generating electricity to provide the greatest environmental benefit. Hydropower plant currently is the largest source of renewable energy in the electricity sector. Sirikit Hydro Power Plant is the largest saddle dam in Thailand, not only help power system fulfill peak demand period but also support power systems in northern Thailand during transmission maintenance, affecting approximately start-stop 3,000 times/year. Therefore, Sirikit Hydro Power Plant always prepares for synchronization systems. One of the important speed and load adjustments is Governor control systems.

The governor control system of Sirikit Hydro Power Plant is an electrical automatic control guide vane and inlet valve consisting of sequence control, power output control, turbine speed control, opening limiter, guide vane position control, and isolated network control. Thus, the system is essential for releasing water and generating electricity of the Sirikit Hydro Power Plant.

Figure 1 shows an overview of a part of the governor control system. The Governor control system is the main controller of the hydraulic turbine, control command, and automation of machines and processes of the proportional valve by the programmable logic controller (PLC). Solenoid valves are electronic devices that transform electrical energy into mechanical force and motion controlled by PLC in multiple control modes such as normal, freezing, emergency shutdown (ESD), quick shutdown (QSD), and manual mode.

This work is sponsored by Electricity Generating Authority of Thailand (EGAT).

The principle of mechanical systems begins with the governor oil pump building up oil pressure when systems detect that the pressure of the tank drops. As a result, the pressure tank distributes oil pressure to both of proportional control valve and the distributing valve. Then position sensor of the proportional control valve has the role of feedback for controlling the position of the distributing valve by closing or opening the oil pressure. After that, the distributing valve controls the servo motor to close or open the wicket gate. The turbine speed sensor is sensed by the rated speed for the control speed of the turbine. Finally, the output power is controlled by opening a wicket gate to increase the load (MW). On the other hand, the load will decrease if the wicket gate closes.

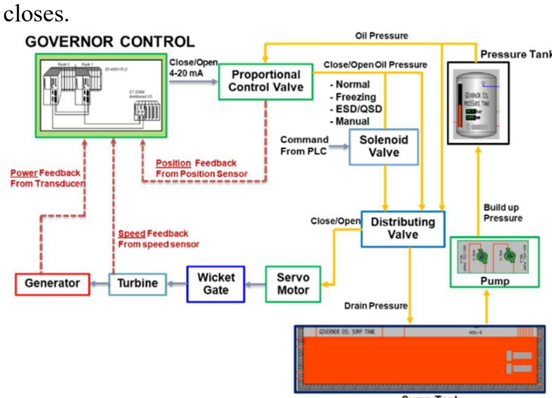

Figure 1 overview a part of the governor control system

The governor control systems interface with the user by programming device is an engineering laptop used together with programmable logic control (PLC) and human-machine interface (HMI) at the operator panel. Limited access and no specific troubleshooting guidance can cause spending more time on problem-solving and loss more availability payment leading to generating power. Reducing working time to resolution requires being able to identify event root causes in minutes or seconds. The Real-Time Root Cause Analysis of the Governor Control System in this paper helps to identify the contributing causal factors associated with adverse events.

The various method that identifies the root cause of events or system failure condition was proposed in the literature. The reliability assessment can be performed based on quantitative and qualitative analysis. The most used methods are fault tree analysis as shown in the research of Knezevic et al. (2020), Hu et al. (2020), Melani et al. (2018), Wang et al. (2017) and Kemikem et al. (2018) and the other methods are rule and logic trees as shown in Nicolau et al. (2017), simulation method in research of Priambodo et al. (2018) and Dudgeon (2017), Expert system method in research of Buaphan et al. (2017), and the last method is Failure Modes and Effects Criticality Analysis (FMECA) is used in research of Hu et al. (2020), Melani et al. (2018). Our project uses fault tree analysis (FTA) because simple to comprehend the reasoning behind the undesirable state or top event and demonstrate compliance with input system reliability standards.

The FTA is a systematic and deductive procedure for defining the adverse event and determining all possible reasons that could result in the adverse events of the system. The adverse event will be the top event of a fault tree diagram, then takes a top-down approach to assess failure consequences and trouble-shooting root cause failure analysis as presented by Buaphan et al. (2017).

This paper study to develop a real-time root cause analysis of the governor control system for Sirikit Hydropower and create the FTA by using Node-red software based on real-time data as shown in Figure 2.

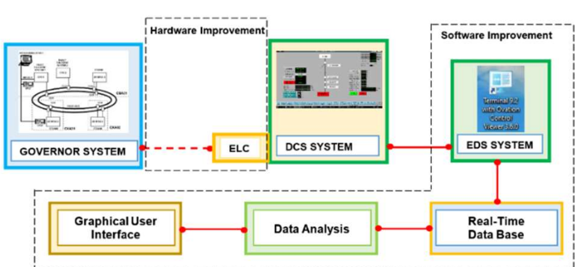

Figure 2 overview improvement diagram

Hardware improvement:

Ethernet Link Controller (ELC) Module to get data interface between governor system and DCS by communication cable (LAN) using Modbus protocol.

Software improvement:

(a) Enterprise Data Server (EDS) is an existing online application of DCS and shows current/historical data.

(b) Real-Time Data Base access data from EDS, this use for knowledge is based on input/output real-time data of the governor system and DCS, maintenance instruction manual, history events, and drawing of the governor control system.

(c) Data Analysis uses fault tree analysis techniques to analyze fault events using information from a knowledge base and a real-time database.

(d) Graphical User Interface is a real-time trouble shooting guide monitor with user-friendly.

2. Design Concept of Real-Time Root Cause Analysis

To facilitate more effective problem-solving for maintenance & operation staff. This results in reduced financial loss and charges from stopping the machine. the real-time root cause analysis has been developed for problems solving not only electrical failure but also mechanical failure of the governor control system Sirikit Hydro Power Plant in this paper. For example, the Turbine is ready To Start, the governor is quick or emergency shutdown, the temperature turbine guide bearing is too high, and the shaft seal water flow is too low. The flow diagram is shown in Figure 3.

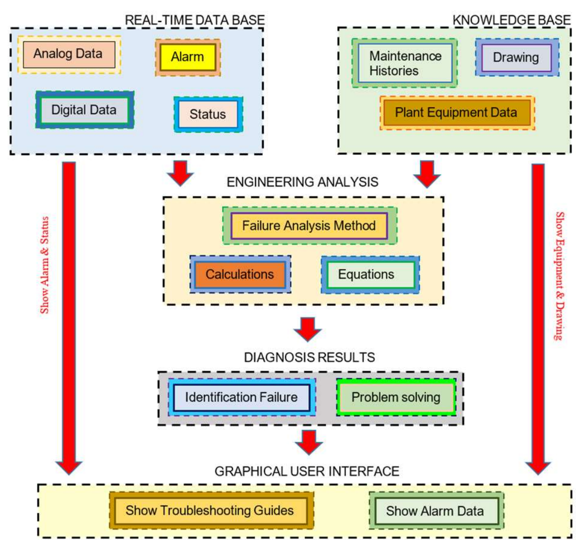

Figure 3 flow diagram of the real-time root cause analysis

The real-time root cause analysis flow diagram displays the program's overall workflow. The first is a knowledge base derived from power plant data and a database containing real-time data from DCS. The second is engineer analysis, which makes use of FTA, equations, and calculations based on the governor control system's parameter settings. The third step involves identifying failures in the diagnosis results and displaying problem-solving techniques. The final graphic user interface shows alarm data and user-friendly suggestions for troubleshooting.

A. Real-time database

The DCS system data will transfer via the EDS system and then send real-time application program interface (API) data including analog data, digital data, sequence of events (SOE), alarm, and status of the governor system. Finally, the software application will receive the data from the API. We chose the Node-red program for our project because it can transfer API data and has a user-friendly Boolean logic flow feature.

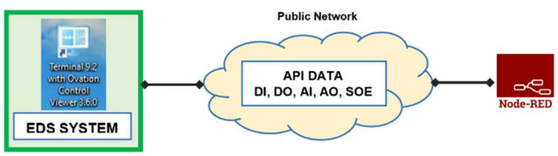

Figure 4 EDS system transfer to Node-Red program

B. Knowledge base

The knowledge base is supporting data to improve root cause analysis more effectively as listed below and the structure is shown in Figure 5.

1) Maintenance histories: corrective & preventive maintenance report, minor inspection report, major overhaul report, and test report.

2) Plant equipment data: instruction manuals.

3) Drawing: control logic and parameter setting.

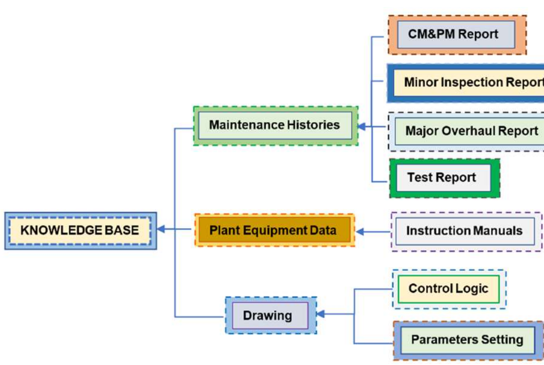

Figure 5 knowledge base structure

C. Engineering analysis

1. Failure Analysis Method

The method of reliability analysis engineering technique is fault tree analysis to understand how systems components can fail, and to identify the best ways to solve emergency case problems of the system, aiming at obtaining optimized results. After that, a summary of failure and transfer data in logic algorithm form. The emergency case problem leading to an emergency shutdown in this project has four types as listed below.

1.1 Lock-out relay 86-1 is an emergency shutdown to instantaneous stop the unit.

1.2 Lock-out relay 86-2 is a quick shutdown. The system decreases load by about 10% of maximum power (12.5 MW) after that stops the unit.

1.3 Lock-out relay 86-3 is a partial shutdown. The system opens the unit circuit breaker, excitation off and down a step from load mode to turbine start mode. The machine runs at the rated speed (125 rpm.).

1.4 Lock-out relay 86-4 is a differential relay. The system instantaneously stops the unit.

If the emergency case of governor control systems happened, systems operate will respond immediately depending on the situation of the emergency case. For instance, as seen in Figure 6, the temperature turbine guide bearing too high (38B21H2) triggers lockout 86-2 as a result of root cause analysis using real-time database and knowledge base data.

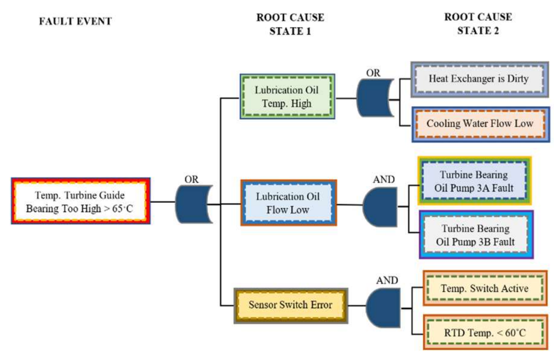

Figure 6 example case "Temperature Turbine Guide Bearing Too High (38B21H2)"

2. Equations and Calculations

Both historian value and testing report data will be analyzed for setting alerts. After that setting alerts notify the operator of first aid this event because the unit is at high risk of emergency shutdown. The alert is helpful for outage planning for preventive maintenance with the maintenance team.

In the example from the knowledge base, Temperature Turbine Guide Bearing Too High (38B21H2) we used a bearing run test report from minor inspection 2017 unit 3 as Figure 7.

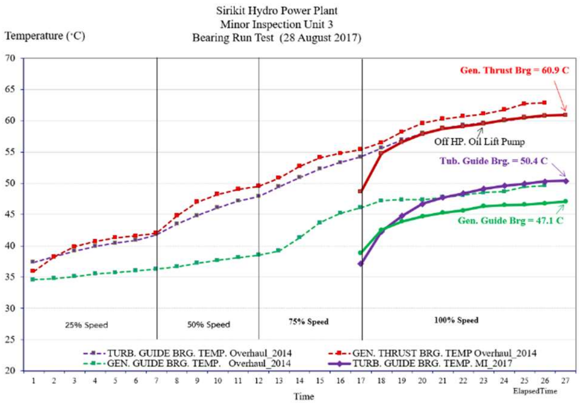

Figure 7 Unit 3 bearing run test report

This report shows the turbine guide bearing temperature needs a time of approximately 30 minutes to be saturate at 50.4 ˚C. The parameter setting of turbine guide bearing temperature alarm and trip at 60 ˚C and 65 ˚C respectively. In this case, we alert at temperature 58 ˚C and notify to operator for planning with the maintenance team to clean the turbine oil cooler heat exchanger.

From a historical value, the governor oil pump normally runs about 30 seconds each time during the mechanic run as Figure 8. When the governor oil pump appears to be something wrong. for example, if the governor oil pump runs overtime, the temperature of the governor oil sump tank will increase at the point of alarm is 65 ˚C and trip at 70 ˚C. So, the set-up alert time of the governor oil pump working is more than 3 minutes. The systems will alert and notify operators then operators have to check the governor oil pump working and the governor oil sump tank temperature.

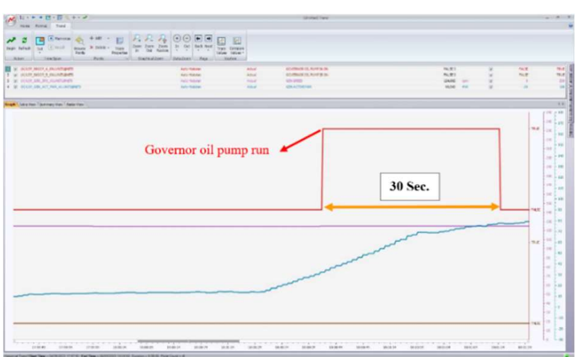

Figure 8 Governor oil pump run of historian

D. Diagnosis result

We collect 24 emergency failure occurrences in the governor system. All problem was identified and the failure cause and was solved by gathering information from engineer analysis, history of event, and experienced maintenance & operation staff of Sirikit Hydro Power Plant from the corrective maintenance report. Then, Information data and problem-solving steps are analyzed to a summary of troubleshooting guide details shown in three examples of emergency failure cases in Sirikit Hydro Power Plant as Table 1 and listed below.

1. Fault Events: Name of an emergency case.
2. Default reaction: The affected machine such as unit trip lockout 86-2.
3. Root Cause State 1: First state of root cause analysis for identify possible main cause of fault event.
4. Root Cause State 2: Second state of root cause analysis for identifying the underlying possible cause from root cause state 1 of fault event in more detailed.
5. Possible Reason: The gathering information from manual of equipment, drawing and experience maintenance & operation staff.
6. Recommend Inspection: The solution recommends for solve and check of each problem that different depend on an emergency case cause.

Subsequently, both engineering analysis and diagnosis result process are important data for creating real-time root cause analysis via Boolean logic that each component has input data then the data can be evaluated as true or false, or 1 or 0 in the node-red program.

For example, in analysis case 38B12H2 - Temp. Generator Thrust Bearing Too High, we analyze how low lubricating oil flow in condition 1 and the generator bearing oil pump A (88QBM1) and B (88QBM2) in root cause state 2 are the main causes of the thrust bearing temperature too high. In the node-red software, we use the AND Boolean operator between the generator-bearing oil pumps A and B failures when the lubricating oil flow is low, as shown in Figure 9.

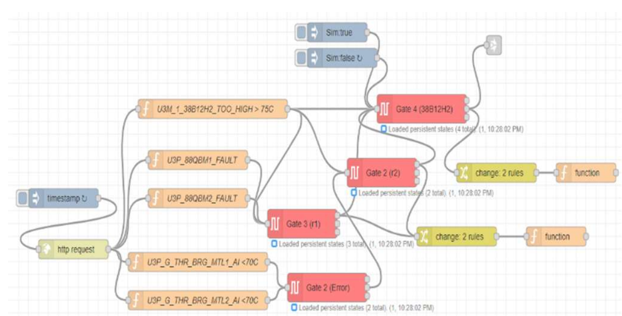

Figure 9 Example create logic flow of 38B12H2 - Temp. Gen. Thrust Bearing Too High at node-red program.

Table 1 The example of trouble shooting guides

No.	Fault Events	Default Reaction	Root Cause State 1	Root Cause State 2	Possible Reason	Recommend Inspection
1	Temperature turbine guide bearing too high (38B21H2)	Unit trip lockout 86-2	1. Lubrication oil temperature high	1.1 heat Exchanger is dirty	- Lubrication oil is contaminated - Cooling water is dirty	- Inspection and clean heat exchanger
				1.2 Cooling water flow low	- Electrical flow sensor switch is bad - Cooling water valve is not fully opened	- Check electrical flow sensor switch - Check status cooling water valve
			2. Lubrication oil flow low	2.1 Turbine bearing oil pump A, B fault	- Motor overcurrent	- Check overload relay - Check status lubrication oil valve - Pump A, B inspection
			3. Temperature detector is error	3.1 Temperature switch is active and RTD temperature is lower than 65 ˚C	- Wiring connection is loose - Temperature detector is Bad	- Check annunciator - Check relay K902 - Check wiring connection at terminal
2	Temperature governor oil sump tank too high (23QTTH2)	Unit trip lockout 86-2	1. Oil circulation at governor oil sump tank	1.1 Governor oil pump A run overtime or 1.2 Governor oil pump B run overtime	- Pressure relief valve mechanical "ON"	- Check pressure at governor pressure tank - Inspection governor oil pump A, B - Check unloading valve
					- Electrical pressure switch malfunction	- Check pressure switch - Logic function check
3	Shaft seal water flow too low (80FPTL)	Unit trip lockout 86-2	1. Orifice valve is dirty	1.1 Main strainer is dirty	- Cooling water is dirty	Inspection & clean main strainer
				1.2 Shaft seal strainer is dirty	- Cooling water is dirty	Inspection & clean shaft seal strainer
			2. Flow sensor is error	-	- Wiring connection is loose - Flow sensor switch is bad	- Check flow sensor - Check relay K1130 - Check wiring connection at Terminal

E. Graphical user interface

A graphical user interface is a computer program that enables a person to interact with a computer through the graphical components. This shows the overall status of the system and makes with user-friendly, simple, and easy to use. The graphic was created by the node-red dashboard program. In this paper, the graphic working separate in two parts.

Part 1: Ready to start checker of governor system as Figure 11. This is importance part because the machine was started-stopped many times/years. If start-up failure happens, effect to available payment of the power purchase agreement and key performance index of hydro power plant.

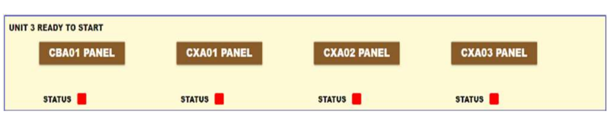

Figure 11 Graphic unit 3 ready to start

Part 2: Emergency Cases of the governor system that divided into 6 groups as Figure 12 and list below.

Group 1: External Trip is the governor system that cannot detect fault. So, other equipment such as the generator protection relay or excitation system can detect faults and then will send a trip command to the governor system.

Group 2: Emergency push button on every panel of the governor system. The button has 2 types.

Type 1: Emergency shutdown is instantaneous stop.

Type 2: Quick shutdown is decrease about 10% load of maximum power (12.5 MW) after that stop the unit.

Group 3: Speed device is detected overspeed from electrical and mechanical and need 2 failures of 3 speed sensor failures.

Group 4: Inlet Valve System is detected hydraulic control of the inlet valve such as the pressure or level of the inlet valve pressure tank.

Group 5: Turbine System is detected hydraulic control and shaft sealing water of the turbine.

Group 6: Temperature is detected oil temperature such as lubrication oil temperature at the guide bearing and thrust bearing of the machine, oil temperature of the control actuator.

NUEJ
Naresuan University
Engineering Journal

3. Results and Discussion

Case Study, The generator can't control power in load mode status. So, that effect to load (MW) swing and unit trip lockout 86-2 detected temperature too high. The system sends the trip signal from the temperature governor oil sump tank that is too high temperature (23QTTH2) as Figure 12.

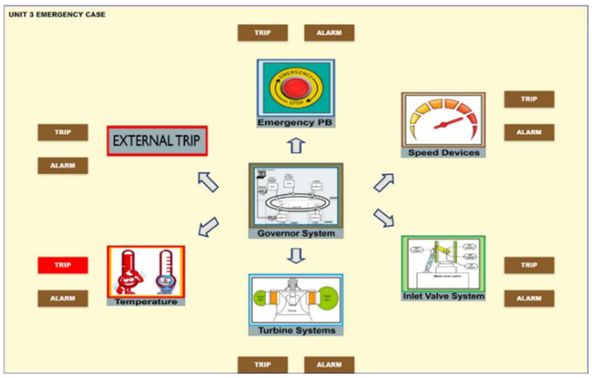

Figure 12 Detected temperature high trip

The program's real-time root cause analysis will show a troubleshooting guide as listed below and in Figure 13.

Fault Events: Temperature governor oil sump tank too high (23QTTH2)

Default Reaction: Unit trip lockout 86-2

Root Cause State 1: Oil circulation at governor oil sump tank

Root Cause State 2: 1.1 Governor oil pump A run overtime or
1.2 Governor oil pump B run overtime

Possible Reason: 1. Pressure relief valve mechanical "ON"

Recommend Inspection: - Check pressure at governor pressure tank
- Inspection governor oil pump A, B
- Check unloading valve

Possible Reason: 2. Electrical pressure switch malfunction

Recommend Inspection: - Check pressure switch
- Logic function check

Event History: Unit 4
- Gov. oil Pump still working and unloading equipment always on, effect to increase governor oil sump tank temperature leading to uncontrol power (MW)

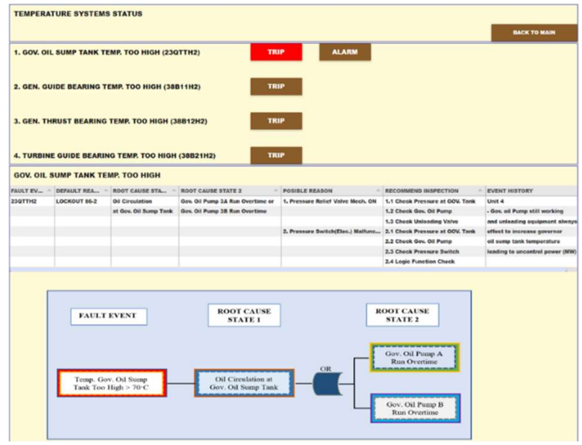

Figure 13 Trouble shooting guide of "Temperature governor oil sump tank too high (23QTTH2)"

If the oil sump tank temperature is high before synchronizing mode, it will be hard to synchronize to the grid. Because difficult control speed relates to frequency before synchronizing into the power grid and effect start-up unit failure.

Typically, we solve fault events by depending on the expertise of the operation and maintenance personnel. After that, we use the real-time root cause analysis system which helps to reduce the time for deification fault events and has a guide dance to solve the problem.

4. Conclusion

The real-time root cause analysis of the governor control system can help maintenance & operation staff reduce the time for solving problems by using a troubleshooting guide from the dashboard of the node-red program. This system can reduce financial loss and charges from stopping the machine. In addition, the maintenance managers can choose the best way to decision solve the problem or plan to shut down the machine when major or minor trouble happens and decide to shut down at a suitable time. Gained a great benefit for the Sirikit hydropower plant by applying a real-time root cause analysis system to diagnose fault events.

5. Acknowledgment

The authors are grateful to knowledge support for this research from Electricity Generating Authority of Thailand (EGAT) and Chiang Mai University (CMU). Moreover, we are thankful to the operation and maintenance staff of Sirikit Hydro who sharing experience about the governor system emergency case that occur in Sirikit Hydro Power Plant.

6. References

Buaphan, I., & Premrudeepreechacharn, S. (2017, 21-24 June 2017). *Development of expert system for fault diagnosis of an 8-MW bulb turbine downstream irrigation hydro power plant*. Paper presented at the 2017 6th International Youth Conference on Energy (IYCE). https:/doi.org/10.1109/IYCE.2017.8003740

Dudgeon, G. (2017). *Power Plant Model Validation (PPMV) with MATLAB and Simulink [White paper]. MathWorks Principal Industry Manager, Utilities &Energy*. https://www.mathworks.com/campaigns/offers/next/power-plant-model validation.html

Hu, X., Zhang, K., Liu, K., Lin, X., Dey, S., & Onori, S. (2020). *Advanced Fault Diagnosis for Lithium-Ion Battery Systems: A Review of Fault Mechanisms, Fault Features, and Diagnosis Procedures*. IEEE Industrial Electronics Magazine, 14(3), 65-91. https:/doi.org/10.1109/MIE.2020.2964814

Knezevic, V., Orovic, J., Stazic, L., & Culin, J. (2020). *Fault Tree Analysis and Failure Diagnosis of Marine Diesel Engine Turbocharger System*. 8(12), 1004. https://doi.org/10.3390/jmse8121004

Kemikem, D., Boudour, M., Benabid, R., & Tehrani, K. (2018, 19-22 June 2018). *Quantitative and Qualitative Reliability Assessment of Reparable Electrical Power Supply Systems using Fault Tree Method and Importance Factors.* Paper presented at the 2018 13th Annual Conference on System of Systems Engineering (SoSE). https://doi.org/10.1109/ SYSOSE.2018.8428729

Melani, A. H. A., Murad, C. A., Caminada Netto, A., Souza, G. F. M. d., & Nabeta, S. I. (2018). *Criticality-based maintenance of a coal-fired power plant. Energy, 147, 767-781.* https://doi.org/10.1016/j.energy.2018.01.048

Nicolau, A. d. S., Algusto, J. P. d. S. C., Pereira, C. M. d. N. A., & Schirru, R. (2017). *A Real Time Expert System for Decision Support in Nuclear Power Plants.* World Academy of Science, Engineering and Technology International Journal of Nuclear and Quantum Engineering, 11(9), 612-618. doi:https://doi.org/10.5281/zenodo.1131982

Priambodo, N. W., Harsono, B. B. S. D. A., & Munir, B. S. (2018, 24-26 July 2018). *Root Cause Analysis of Transformer and Generator Stator Failure on Hydropower Plant in Indonesia.* Paper presented at the 2018 10th International Conference on Information Technology and Electrical Engineering (ICITEE). https://doi.org/10.1109/ICITEED.2018.8534825

Wang, Y., Li, X., Ma, J., & Li, S. (2017). *Fault diagnosis of power transformer based on fault-tree analysis (FTA*). IOP Conference Series: Earth and Environmental Science, 64(1), 012099. https://doi.org/10.1088 /1755-1315/64/1/012099

NUEJ
Naresuan University
Engineering Journal

Study of Unbalanced Voltage on Rotor Classes of Induction Motor According to NEMA Standard

K. Kraikitrat[1], S. Ruangsinchaiwanich[2], and D. Phaengkieo[3*]

[1] Department of Electrical Engineering, Faculty of Engineering, University of Phayao, Phayao, Thailand
[2] Department of Electrical and Computer Engineering, Faculty of Engineering, Naresuan University, Phitsanuloke, Thailand
[3] Department of Electrical Engineering, Faculty of Engineering, Rajamangala University of Technology Lanna Phitsanulok, Phitsanulok, Thailand

[*]Corresponding author e-mail: duanraem@rmutl.ac.th

(Received: 2 May 2023, Revised: 21 November 2023, Accepted: 1 December 2023)

Abstract

This investigation studies core loss and thermal distributions. There are four types of 3-phase induction motors that meet the National Electrical Manufacturers Association (NEMA) standard when receiving unbalanced voltage by testing the motor under unbalanced voltage conditions. The conditions are different. The model analysis method was used in conjunction with the Finite Element Method (FEM) as well as experimental and computational theory. To analyze the change in magnetic flux density and the resulting temperature. Along with finding a conclusion on the effect on the motor when the voltage is unbalanced.

Keywords: FEM, Flux Distributions **,** Induction Motor, Thermal distributions, Unbalanced Voltage Conditions.

1. INTRODUCTION

Electricity is a crucial element for economic growth and national security. When the power system is abnormal, such as when the magnitudes of phase or line voltages are distinct, and the phase angles differ from balanced conditions or both, Etc., it is detrimental to the system's overall performance because even the smallest imbalance will have a significant effect on the electrical equipment particularly 3-phase induction motors, which are extensively utilizing. The operating parameters vary if the motor operates under an unbalanced voltage condition. Consequently, the motor's performance is altering and may be damaged. The National Electrical Manufacturers Association (NEMA) has classified the various types of induction motors so that the appropriate selection can be made based on the nature of the activity. Each variety is characterized by its Torque-Speed. However, NEMA has not clarified how Core Loss and Thermal differ between motor types. Therefore, this study investigated the effect of Core Loss. Furthermore, Thermal occurs in each motor type under unbalanced input voltage conditions.

Faults of the electrical system, for example, unbalanced voltage conditions and inconsistent frequency, is frequently occurred, which reduces the quality of the electrical system and affects the efficiency of electrical appliances, especially electrical motors (Kersting & Phillips, 1997; Ching-Yin Lee et al., 1997; Siddique et al., 2004; Chen, K., 2009).

This paper analyzes the effects of unbalanced voltage conditions on the Core Loss and Thermal Analysis of Class A, B, C, and D motors according to NEMA standards by specifying and designing all four motor models with identical rotor volumes. Twenty cases are computed using the Line voltage unbalance rate (LVUR) and Phase voltage unbalance rate (PVUR) methods to ascertain the voltage unbalance condition.

2. UNBALANCE VOLTAGE CONDITIONS

Various standards have provided the following three definitions of voltage imbalances. The National Electrical Manufacturers Association (NEMA) standard MG1-1993 defines voltage unbalance, also known as the line voltage unbalance rate (LVUR).

$$\%\ \text{LVUR} = \frac{\begin{array}{c}\text{Max voltage deviation-}\\ \text{from the avg line voltage}\end{array}}{\text{avg line voltage}} \times 100\% \tag{1}$$

The IEEE defines voltage unbalance, called the phase voltage to unbalance rate (PVUR).

$$\%\ \text{PVUR} = \frac{\begin{array}{c}\text{Max voltage deviation-}\\ \text{from the avg phase voltage}\end{array}}{\text{avg phase voltage}} \times 100\% \tag{2}$$

Genuine Definition: The ratio of the negative sequence voltage component to the positive sequence voltage component is the simple definition of voltage unbalance (R.C. Dugan et al., 1996). The true definition of the percentage voltage disequilibrium factor (% VUF) is given by

$$\%\ \mathrm{VUF} = \frac{\text{Negative sequence-voltage component}}{\text{Positive sequence-voltage component}} \times 100\% \quad (3)$$

3. INDUCTION MOTOR OF NEMA DESIGNS CLASS

The national electrical manufacturers association (NEMA) defines a series of standard rotor-shape designs with different torque-speed characteristics. Figure 1 shows the prototype of a class B rotor induction motor, the main motor components, and the mesh of the 3D FEM model.

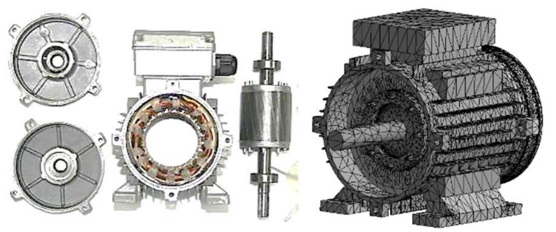

(a) (b)

Figure 1 Prototype of class B induction motor
(a) main motor components, (b) mesh of 3D FEM model

3.1 Stator Dimensions

Figure 2 depicts the dimensions of the induction motor prototype and the diameters of the stator and rotor.

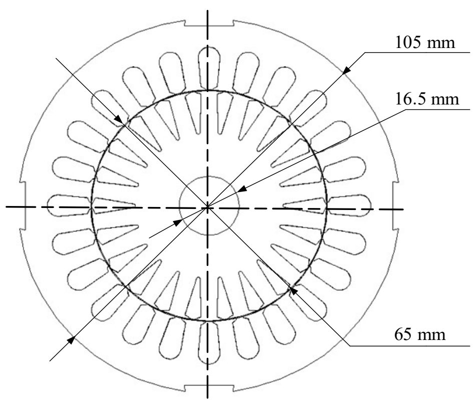

Figure 2 Dimension of the prototype induction

3.2 Rotor Dimensions of NEMA Designs

(a) (b) (c) (d)

Figure 3 Dimension of rotors
(a) class A (b) class B (c) class C (d) class D

The NEMA specification guides the design of the rotors utilized in this investigation. To facilitate comparison, the volume of each of the four rotor classes is identical. The prototype of rotor configurations, including classes A, B, C, and D, is illustrated in Figure 3.

4. ANALYSIS OF RESULT

Several methods can illustrate the effect of unbalanced voltage conditions on an induction motor. In this paper, FEM calculation is focused on. FEM is largely accepted as a significant method for analyzing the electromagnetic field, particularly electrical machines' performances.

The impact of rotor bar slot geometry on core loss and heat transfer is analyzed. In this study, the rotor volumes of all four varieties are equivalent. Before analyzing these effects on the prototype motor and models of all four categories of motors, these effects must be analyzed on the prototype motor. In the example depicted in Figures 4 and 5, the situation is as shown.

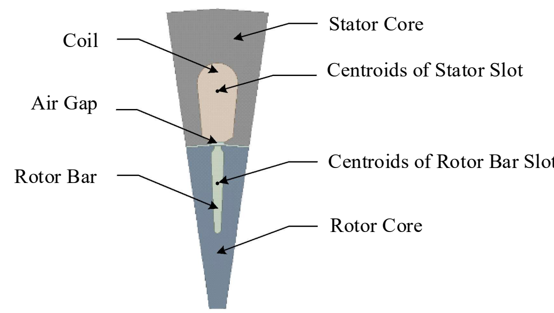

Figure 4 Dimension of sample model

Despite sharing an identical capacity, the four variants of motors differ in the configuration of the slots on the rotor bar. As illustrated in Figure 5, this investigation is also capable of identifying discrepancies in rotor bar slot geometries, specifically the distance between the rotor bar slot's centroid and the stator slot. The thermal and core loss are directly influenced by the centroid of the rotor opening.

10.33 12.07 10.61 12.92

(a) (b) (C) (d)

Figure 5 Examples of motor models (a) class A (b) class B
(c) class C (d) class D

4.1 Flux distributions

Magnetic field density can be derived from Equation (4), that is, by calculating the magnetic flux (ϕ) per unit area (A) that travels through the conductor.

$$B = \frac{\phi}{A} \tag{4}$$

When contemplating the transient for a 3D Cartesian problem, the magnetic field's mathematical model can be expressed as a second-order partial differential equation.

$$\frac{\partial}{\partial x}\left(\frac{1}{\mu}\frac{\partial A}{\partial x}\right)+\frac{\partial}{\partial y}\left(\frac{1}{\mu}\frac{\partial A}{\partial y}\right)+\frac{\partial}{\partial z}\left(\frac{1}{\mu}\frac{\partial A}{\partial z}\right)=-J+\sigma\frac{\partial A}{\partial t} \tag{5}$$

Where (A) is the desired magnetic vector potential, μ is the magnetic permeability, σ is the electrical conductivity, ω is the angular velocity, and J is the current density at is obtained from an external power source, and i is the imaginary part. The term $\sigma(\partial A/\partial t)$ represents the current induced in the conductor material as the magnetic flux changes with time.

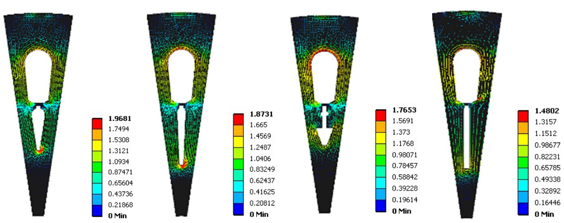

(a) (b) (c) (d)

Figure 6 Flux distributions of motor model examples by FEM (a) class A (b) class B (c) class C (d) class D

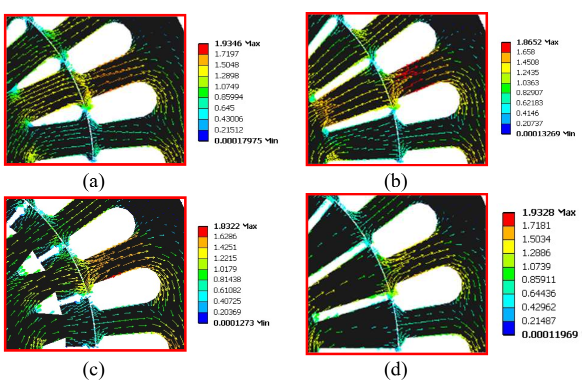

Figure 7 Flux distributions of motors by FEM
(a) class A (b) class B (c) class C (d) class D

The induced magnetic flux on the iron centers of the stator and rotor is illustrated in Figures 6 and 7. Using the FEM method, the no-load voltage rating is calculated from the example model in Figure 5 and the normal-sized motor model. As illustrated in Figure 6, the stator and rotor conductor currents produce magnetic flux in the stator and rotor iron cores. As a result, the magnetic flux that the motor produces is equal to the sum of the two magnetic fluxes. The distinct total magnetic fluxes result from the fact that the volume of the rotor bar slots remains constant while the centers of the slots' geometries (centroid points) vary. The magnetic flux in Fig. 6(d) is greater than in Fig. 6(a) due to the shorter distance between the conductor centers that produce the two magnetic flux sources. As a result, the magnetic flux will be amalgamated as well.

As shown in Equations (6) and (7), the magnetic field density immediately affects the iron core losses. Equation (6) illustrates the typical combination of hysteresis and eddy current losses that contribute to the iron core losses in the stator and rotor.

$$P_c = P_h + P_e$$

$$P_c = k_h f B^n + k_e f^2 B^2 \tag{6}$$

Where P_c is Core Loss, P_h is Hysteresis Loss, P_e is Eddy Current loss, k_h,k_e and n is Coefficients, f is Frequency, and B is the Peak value of the Magnetic Flux. Density. However, the effect of increased losses in the case of high frequencies has been added to increase the eddy current. Therefore, the calculation formula becomes.

$$P_c = P_h + P_e + P_a$$

$$P_c = k_h f B^n + k_e f^2 B^2 + k_a f^{1.5} B^{1.5} \tag{7}$$

Where P_a is Excess Loss and k_a is Coefficients.

Table 1 The core loss of induction motor class B

Conditions	Core Loss (W)		Error (%)
	Analysis	FEM	
Balance	31.3101	31.2759	0.1092
Under 1∅ 1 Percent	30.9989	31.1185	0.3825
Under 1∅ 2 Percent	30.6915	30.9281	0.7566
Under 1∅ 3 Percent	30.3972	30.7317	1.0695
Under 1∅ 4 Percent	30.1064	30.5326	1.3626
Under 1∅ 5 Percent	29.8281	30.3242	1.5861
Under 2∅ 1 Percent	30.6881	31.1018	1.3228
Under 2∅ 2 Percent	30.0932	30.9015	2.5843
Under 2∅ 3 Percent	29.5245	30.6985	3.7536
Under 2∅ 4 Percent	28.9633	30.4961	4.9010
Under 2∅ 5 Percent	28.4274	30.2813	5.9274
Over 1∅ 1 Percent	31.6251	31.4237	0.6312
Over 1∅ 2 Percent	31.9537	31.5684	1.2075
Over 1∅ 3 Percent	32.2863	31.6898	1.8693
Over 1∅ 4 Percent	32.6230	31.8081	2.5539
Over 1∅ 5 Percent	32.9638	31.9096	3.3037
Over 2∅ 1 Percent	31.9405	31.4405	1.5630
Over 2∅ 2 Percent	32.5990	31.5954	3.1373
Over 2∅ 3 Percent	33.2863	31.7405	4.8321
Over 2∅ 4 Percent	34.0033	31.8724	6.6611
Over 2∅ 5 Percent	34.7304	31.9910	8.5632

Table 1 shows the iron core loss of a prototype Class B motor under mechanical load at various voltage unbalanced conditions between the FEM method and the calculation. Furthermore, Figures 8 and 9 show the effect of voltage unbalance on core loss power, both under normal and above normal pressure conditions, while the motor operates without mechanical load.

Figure 10 depicts the influence of unbalanced voltage conditions on iron core power loss. Under typical and above normal voltage conditions for all four types of motors, While the motor operates without mechanical load, Figure 11 compares the core loss power under equilibrium voltage conditions while driving various mechanical load levels among the four motor varieties.

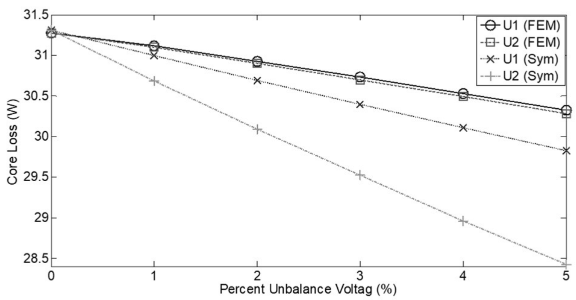

Figure 8 Core loss of the class B motor with under voltage conditions

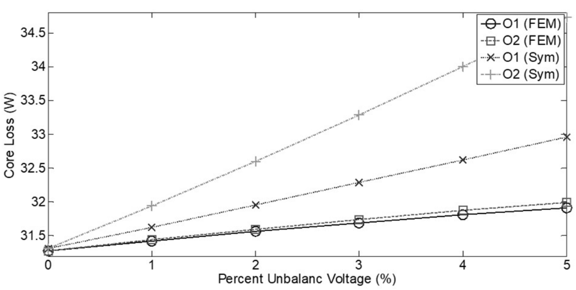

Figure 9 Core loss of the class B motor with over voltage conditions

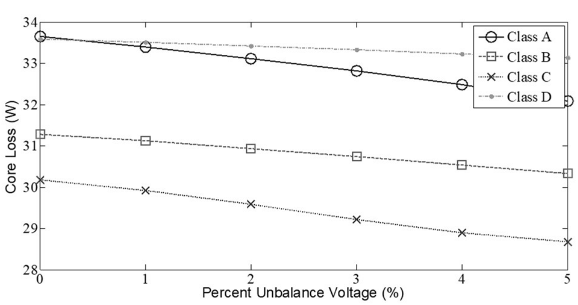

(a)

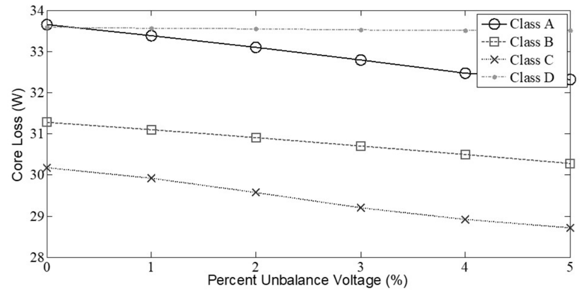

(b)

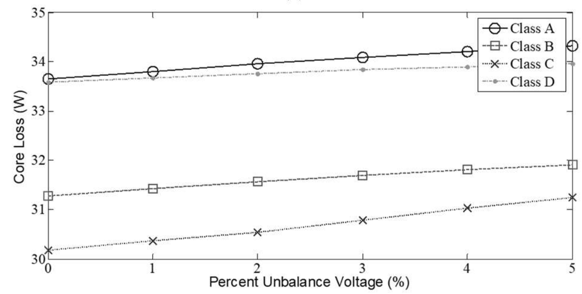

(c)

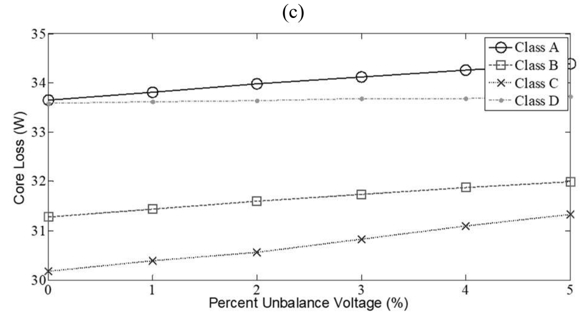

(d)

Figure 10 Core loss of motor class A, B, C and D
(a) under voltage 1 Phase (b) under voltage 2 Phase
(c) over voltage 1 Phase (d) over voltage 2 Phase

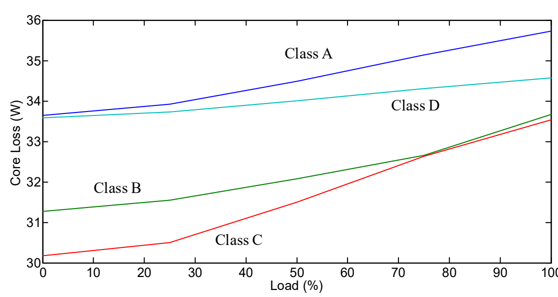

Figure 11 Core loss comparison of motors

4.2 Thermal Distributions

Heat Transfer is the exchange of hot energy. as a result of the temperature difference, and it drives the heat flow from high temperature to low temperature.

$$q = -k.A.\frac{T_2 - T_1}{L} \tag{8}$$

Equation (8) shows the thermal conductivity rate that is directly proportional to the temperature difference at both sides of the object (T_1 and T_2) and the surface area perpendicular to the heat flow direction (A) and is inversely proportional to the thickness of the object (L).

Figure 12 illustrates two sources of heat in the motor: the stator windings and the rotor bar openings. In Fig. 12(a), the distance between the two sources (centroid point) is smaller than the distance between the sources in Fig. 12(d), resulting in more significant maximal heat generation than in Fig. 12(d).

The 3D-heat conduction equation, which can describe steady-state and transient temperature distribution in the solution region (Ω), is regulated by the differential equation (9):

$$-\left(\frac{\partial q_x}{\partial x}+\frac{\partial q_y}{\partial y}+\frac{\partial q_z}{\partial z}\right)+q_O=\rho c\frac{\partial T}{\partial t} \tag{9}$$

Where q_x, q_y and q_z heat flow rate of x, y, z directions respectively; q_O heat generation; ρ mass density (kg/m^3), c specific heat capacity; T temperature (℃).

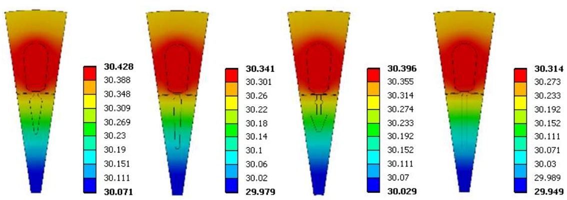

(a) (b) (c) (d)

Figure 12 Thermal distributions of motor model examples by FEM (a) class A (b) class B (c) class C (d) class D

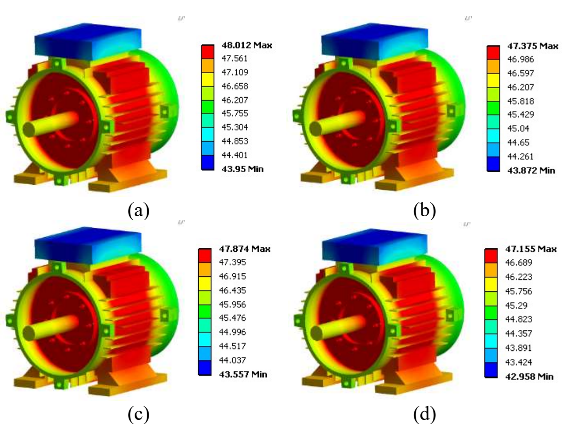

Figure 13 Thermal distributions of motors by FEM
(a) class A (b) class B (c) class C (d) class D

Figure 12 is the result of the analysis of how the rotor bar geometry affected the heat that the sample simulation in Figure 5 produced. Additionally, the findings of the investigation into the impact of the rotor bar slot geometry on the heat produced in four different types of conventional motors are presented in Figure 13. It was observed that the heating effect of the rotor bar varied depending on its geometry. As shown in Tables 2 and 3, Figure 14 is a thermal camera image of a prototype Class B motor operating under varying voltage and mechanical load conditions. Additionally, Figures 15 and 16 compare the heat the prototype Class B motor produces experimentally and using FEM. It was observed that both approaches produced thermal energy in the motor in the identical direction.

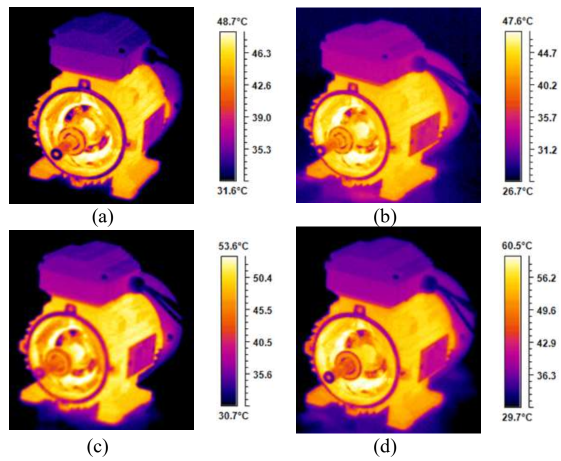

Figure 14 Thermal distribution of the class B motor by measurement with balancing voltage at no load condition

Table 2 Maximum temperature of induction motor class B

Load (%)	Maximum Temperature (˚C)		
	Test	FEM	Error
0	47.9	47.375	1.096
25	48.9	49.379	0.979
50	53.1	54.831	3.259
75	61.0	63.388	3.914
100	73.6	74.716	1.516

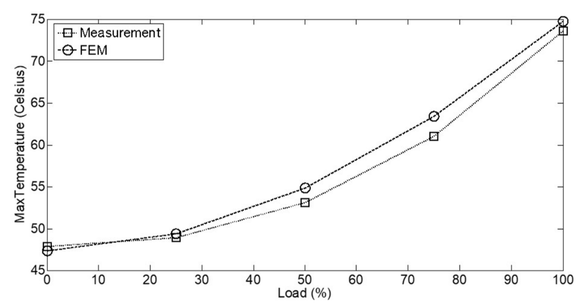

Figure 15 Maximum temperature of motors

Table 3 Maximum temperature of induction motor class B

Conditions	Maximum Temperature (˚C)		
	Test	FEM	Error
Balance Voltage	47.9	47.375	1.096
Under Voltage 1 Phase 5%	47.3	46.774	1.112
Under Voltage 2 Phase 5%	44.8	45.617	1.823
Over Voltage 1 Phase 5%	52.2	49.390	5.383
Over Voltage 2 Phase 5%	55.2	50.849	7.882

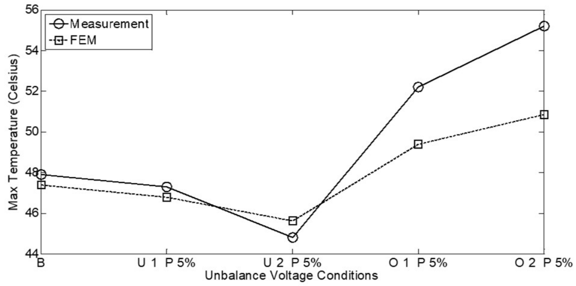

Figure 16 Maximum temperature of motors

When contemplating the effects of unbalanced voltage conditions on the heat generated by the four types of motors, under both normal and overvoltage conditions, while the motor is operating without mechanical load: Figure 17 depicts the result, and Figure 18 compares the heat generated by all four types of motors while driving various levels of load.

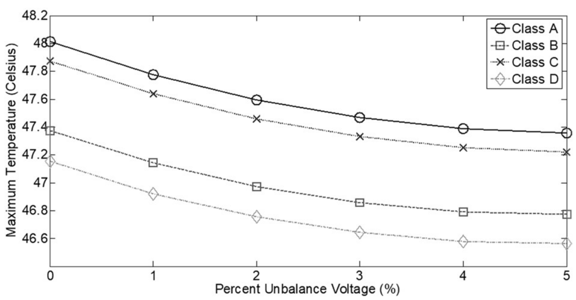

(a)

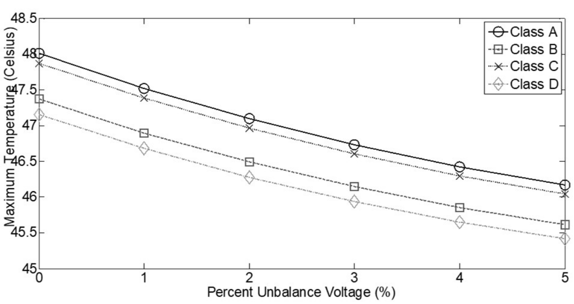

(b)

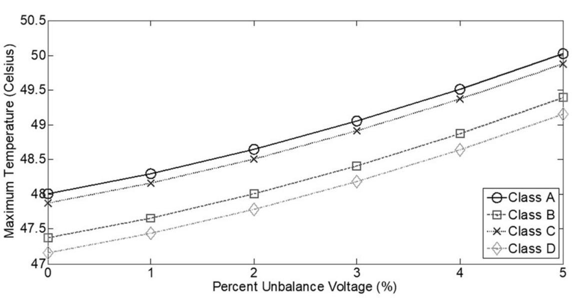

(c)

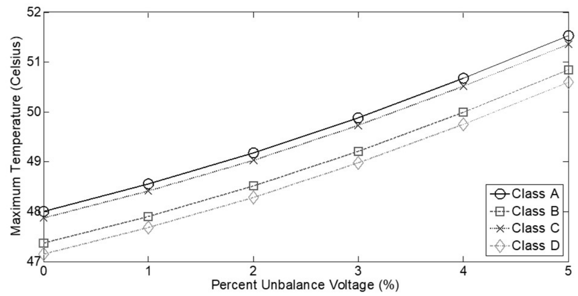

(d)

Figure 17 Maximum temperature of motor class A, B, C and D (a) under voltage 1 Phase (b) under voltage 2 Phase (c) over voltage 1 Phase (d) over voltage 2 Phase

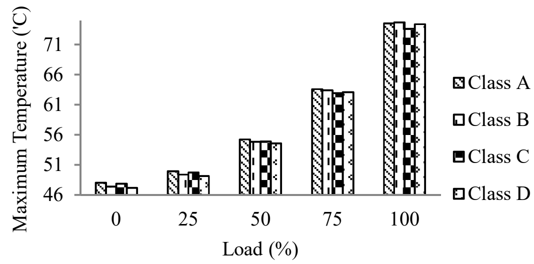

Figure 18 Maximum temperature comparison of motors

5. CONCLUSION

They are considering the effects of unbalanced voltages on iron core loss and heat generation in all four varieties of motors with identical rotor area specifications. The following results: Iron core loss is most significant in Class A motors. Because the distance between the centers of the conductors causes the two sources of magnetic flux to be shorter than in other motors, there is a possibility that the magnetic flux will also be combined. The value of magnetic flux is directly proportional to the resulting iron core loss. Class A motors were discovered to produce the most heat in terms of heat output. Since the distance between the two heat sources is the shortest between the stator winding and the rotor bar, the temperature accumulation is most significant.

Consider the various rotor shapes of the four varieties and the iron core loss and heat generated. Consequently, it can be concluded that, in addition to the size of the rotor bar, the geometry of the rotor bar also plays a role. This affects the iron core depletion and heat produced. The geometry factor may have less impact than the dimension factor. Therefore, when contemplating the selection of a motor, the rotor bar's size must be considered, which is the most critical factor in conjunction with the geometry of the rotor bar.

6. ACKNOWLEDGMENT

The author would like to express his gratitude to the Fundamental Fund Research and Innovation Research Budget Program, Thailand Science Research and Innovation (TSRI) Contract Number FF66-RIM033, and the Faculty of Engineering, University of Phayao for providing a space for research.

7. REFERENCES

Kersting, W. H., & Phillips, W. H. (1997). Phase frame analysis of the effects of voltage unbalance on induction machines. *IEEE Transactions on Industry Applications, 33*(2), 415-420.

Lee, C. Y., Chen, B. K., Lee, W. J., & Hsu, Y. F. (1998). Effects of various unbalanced voltages on the operation performance of an induction motor under the same voltage unbalance factor condition. *Electric Power Systems Research, 47*(3), 153-163.

Siddique, A., Yadava, G. S., & Singh, B. (2004, September). Effects of voltage unbalance on induction motors. *In Conference Record of the 2004 IEEE International Symposium on Electrical Insulation* (pp. 26-29). IEEE.

Chen, K. (2009, March). Iron-loss simulation of laminated steels based on expanded generalized steinmetz equation. *In 2009 Asia-Pacific Power and Energy Engineering Conference* (pp. 1-3). IEEE.

Motors and Generators, *ANSI/NEMA Standard MG1-1993*.

IEEE Standard Test Procedure for Polyphase Induction Motors and Generators, *IEEE Standard 112*, 1991.

Dugan, R. C., McGranaghan, M. F., & Beaty, H. W. (1996). *Electrical power systems quality*. New York.

Hwang, C. C., Tang, P. H., & Jiang, Y. H. (2005). Thermal analysis of high-frequency transformers using finite elements coupled with temperature rise method. *IEE Proceedings-Electric Power Applications, 152*(4), 832-836.

Reece, A. B. J., & Preston, T. W. (2000). *Finite element methods in electrical power engineering (Vol. 46).* Courier Corporation.

Shumei, C., Ying, D., & Liwei, S. (2006, September). Rotor slots design of induction machine for hybrid electric vehicle drives. *In 2006 IEEE Vehicle Power and Propulsion Conference* (pp. 1-3). IEEE.

Kirtley, J. L., Cowie, J. G., Brush, E. F., Peters, D. T., & Kimmich, R. (2007, June). Improving induction motor efficiency with die-cast copper rotor cages. *In 2007 IEEE Power Engineering Society General Meeting* (pp. 1-6). IEEE.

Turcanu, O. A., Tudorache, T., & Fireteanu, V. (2006, May). Influence of squirrel-cage bar cross-section geometry on induction motor performances. In International Symposium on Power Electronics, Electrical Drives, Automation and Motion, 2006. *SPEEDAM 2006*. (pp. 1438-1443). IEEE.

Fireteanu, V., Tudorache, T., & Turcanu, O. A. (2007, May). Optimal design of rotor slot geometry of squirrel-cage type induction motors. *In 2007 IEEE International Electric Machines & Drives Conference* (Vol. 1, pp. 537-542). IEEE.

Pillay, P., & Manyage, M. (2001). Definitions of voltage unbalance. *IEEE Power Engineering Review, 21*(5), 50-51.

8. BIOGRAPHIES

Kreangsuk Kraikitrat
Currently working as an Asst. Prof. at the Department of Electrical Engineering Faculty of Engineering, University of Phayao.

Somporn Ruangsinchaiwanich
Department of Electrical and Computer Engineering, Faculty of Engineering, Naresuan University, Muang, Phitsanuloke, Thailand

Duanraem Phaengkieo
Department of Electrical Engineering, Faculty of Engineering, Rajamangala University of Technology Lanna Phitsanulok, Phitsanulok, Thailand

NUEJ
Naresuan University
Engineering Journal

Modeling Molecular Structural Properties of Magnetite (Fe_3O_4) and Mackinawite (FeS) Using Density Functional Theory (DFT)

Saranya Tongkamnoi [1,*], Mayuree P. Reilly [2], Tanapon Phenrat [1,3*]

[1] Research Unit for Integrated Natural Resources Remediation and Reclamation (IN3R), Department of Civil Engineering, Faculty of Engineering, Naresuan University, Phitsanulok, Thailand, 65000
[2] College of Materials Innovation and Technology, King Mongkut's Institute of Technology Ladkrabang, Rd., Ladkrabang, Bangkok, Thailand, 10520
[3] Center of Excellence for Sustainability of Health, Environment, and Industry (SHEI), Faculty of Engineering, Naresuan University, Phitsanulok, Thailand, 65000

*Corresponding author e-mail: pomphenrat@gmail.com

(Received: 30 May 2023, Revised: 27 November 2023, Accepted: 29 November 2023)

Abstract

Bare and sulfidized nanoscale zerovalent iron (bare NZVI or Fe^0 and S-NZVI, respectively) has been widely utilized for environmental restoration. During the degradation and sequestration of contaminants of concern (COCs) such as chlorinated organics and toxic metals, interfacial detoxification reactions are governed by the physical chemistry of the iron oxide shell of bare NZVI and the iron sulfide shell of S-NZVI: magnetite (Fe_3O_4) and mackinawite (FeS), respectively. Because interfacial reactions generally cannot be directly and experimentally monitored, this study examines first-principles methods based on the use of the density functional theory (DFT) as a simulation tool to help understand interfacial phenomena. In this study, DFT approaches with and without long-range van der Waals interactions (so-called DFT and DFT-D2 approaches, respectively) were employed. The simulated unit cell parameters and electronic density of states (DOS) of bulk Fe_3O_4 and FeS were modeled using both DFT and DFT-D2 methods and compared with previous experimental results where these were available. We reveal that there was strong agreement between the simulated properties and previous experimental results. Nevertheless, for both Fe_3O_4 and FeS, the DFT-D2 method performed better than the DFT method in terms of the accuracy of simulated unit cell parameters. Furthermore, the DFT-D2 method simulated the DOS of both materials effectively. The DOS of Fe_3O_4 supports electron transfer from the central octahedral-Fe_B layer to the outer tetrahedral-Fe_A layer, while the DOS of FeS potentially explains the decrease of the NZVI aging effect and enhanced treatment for hydrophobic contaminants due to sulfidation reported in literature. This research projects that DFT-D2 can be used as a tool of choice for understanding the interaction between COCs and Fe_3O_4 and FeS surfaces at nanoscale in order to develop the environmental applications of nanomaterials. For this purpose, further modification of the model is required to properly downscale the computation from bulk to nanoscale materials.

Keywords: density functional theory (DFT), electronic density of states (DOS), simulation, surface energy, Unit cell parameter.

1. NOMENCLATURE

DFT: Density functional theory
DFT-D2: Method combining the DFT energy with a correction to the long-range dispersion interactions
GGA: Generalized gradient approximation
KS: Kohn-Sham
LEED: Low energy electron diffraction
PAW: Projector augmented-wave
PBE: Generalized gradient approximation density functional developed by Perdew, Burke and Ernzerhof
STM: Scanning tunneling microscopy
VASP: Vienna Ab-initio Simulation Package
XPS: X-ray photoelectron spectroscopy
XRD: X-ray diffraction

2. INTRODUCTION

Nanoscale zerovalent iron (NZVI, or Fe^0) has been widely utilized for environmental restoration due to its high reactivity with halogenated organic pollutants, heavy metals, and other inorganic pollutants (Phenrat et al., 2016; Phenrat et al., 2018; Phenrat and Lowry, 2019). Nevertheless, as a side reaction between Fe^0 and water in aquatic environments, NZVI oxidative aging results in unintended H_2 production and electron depletion and competes with intentional reactions for contaminant abatement (Liu et al., 2005; Liu et al., 2007; Mackenzie and Georgi, 2019; Phenrat and Lowry, 2019). NZVI aging leads to surface passivation and a short reactive lifetime unfavorable for environmental engineering applications due to the associated increase in material and operational costs. The main chemical reaction involved in NZVI aging is the oxidation of iron, which generally leads to the formation of a Fe(II)/(III) iron oxide shell. Magnetite (Fe_3O_4) is often a major oxide phase formed under anaerobic conditions. Intrinsic magnetic attraction caused by Fe_3O_4 is the dominant driving force for the agglomeration of NZVI, negatively affecting both suspension stability and transport in saturated porous media. Moreover, although Fe_3O_4 is widely used as the main component of industrial catalysts in numerous processes, there is no agreement on either the termination of its main surfaces or the thermodynamics of the redox reactions taking place on them (Reinsch et al., 2010) while the Fe^0 core is shrinking (Mackenzie and Georgi, 2019; Phenrat and Lowry, 2019). Thus, during the detoxification of chlorinated organics or the sequestration of toxic metals and metalloids in the subsurface using NZVI, contaminants of concern (COCs) will interact with the magnetite surface and not the Fe^0 surface. Consequently, understanding interfacial interactions between COCs and the Fe_3O_4 surface is important for the research and development of NZVI for engineering applications.

On the other hand, as an engineering attempt to alleviate the aging effect, sulfidation can be used to modify NZVI, resulting in the transformation of the NZVI surface to mackinawite (FeS). Sulfidized NZVI (S-NZVI) creates a nucleophilic zone on the particle surface with a lower density of H atoms compared to NZVI, which reduces the recombination of H atoms to form H_2 (water-induced corrosion). However, it enhances the β-elimination pathway for halogenated carbon compounds by facilitating the adsorption between positively charged carbons (α position) and the nucleophile (S^{2-})(Fan et al., 2016; Phenrat and Lowry, 2019). The FeS surface not only alleviates Fe^0 aging but also enhances reactivity and improves electron selectivity for targeted contaminants (Fan et al., 2016; Phenrat and Lowry, 2019). For example, during the dechlorination of chlorinated organics such as trichloroethene (TCE), S atoms on the FeS surfaces appear to induce the formation of acetylene through β-elimination, which consumes less electrons than the hydrogenolysis pathway (Su et al., 2019). Due to the high conductivity of FeS (Su et al., 2019), the dechlorination rate through β-elimination is accelerated. Furthermore, S results in low H atom density, which is not favorable for further hydrogenolysis of acetylene to ethene or ethane because the formation of ethene and ethane from acetylene occurs in high H atom density zones. This means that TCE dichlorination via S-NZVI consumes less electrons than via bare NZVI. Several mechanisms have been hypothesized for the enhanced reactivity and selectivity of S-NZVI compared to bare NZVI. First, S-NZVI is more hydrophobic than bare NZVI, resulting in less interaction with water and charged solutes and greater interaction with hydrophobic contaminants, such as chlorinated organics. Second, the incorporated sulfur lowers the electron transfer resistance of Fe^0 to the contaminant. Third, the incorporated sulfur blocks the adsorption sites for atomic hydrogen and inhibits the water reduction reaction and H_2 evolution (Xu et al., 2021).

These hypotheses have been proposed as a basis for the roles of NZVI aging and sulfidation in groundwater detoxification. Nevertheless, surface reactions are difficult to directly measure and quantify. For this reason, density functional theory (DFT), a form of molecular modeling, is a tool of choice to examine these hypotheses. The accuracy of the DFT is comparable with correlated molecular orbital methods but requires substantially less computational effort (Wimmer, 1996). Because of its computational advantages, DFT has evolved as the most important quantum mechanical approach in solid-state physics (Politzer et al., 1993; Dahl and Avery, 2013) and can handle large, periodic systems that are intractable when using correlated molecular orbital methods (Labanowski and Andzelm, 2012). In DFT, the energy is decomposed into contributions from kinetic energy, the Coulomb energy, and exchange-correlation energy. Although this decomposition is exact, its implementation requires approximations since the actual functionals for the many body exchange and correlation energies are unknown.

In this study, as the first step towards understanding bare and S-NZVI interfacial reactions at nanoscale, we examine the electronic and magnetic properties of bulk Fe_3O_4 and FeS via two different DFT tools and compare the modeling results with measurable parameters, where these are available, for calibration. In future studies, the calibrated model can be used as a base model for the modification and modeling of non-measurable phenomena at nanoscale for environmental nanotechnology applications.

3. COMPUTATIONAL METHODS AND MODEL EVALUATION

Atomistic model simulations based on Density Functional Theory (DFT) are undeniably the most popular quantum chemical methods for analyzing the structure-property relationships of crystalline compounds. DFT has gained significant popularity in solid-state physics. The choice of the functional and basis set are the two most critical variables that must be determined before commencing DFT calculations, and this choice greatly influences the results obtained. Fig. 1 shows two DFT approaches were used for all calculations and optimizations in this study. First, we carried out spin-polarized quantum mechanical calculations PBE was performed using a uniform Monkhorst and Pack grid of 21 x 21 x 21 for sampling BZ and density of states (DOS), because it provides a better description of the structure of solids than its parent functional (De la Pierre et al., 2011). Second, we also using density functional theory (DFT) as implemented in the Vienna Ab-initio Simulation Package (VASP) (Kresse and Hafner, 1993; Kresse and Furthmüller, 1996). The Perdew-Burke-Ernzerh functional (PBE) (Perdew et al., 1992; Perdew et al., 1996) was the version of the generalized gradient approximation (GGA) used as the exchange correlation functional for all geometry optimizations and for the calculation of electronic band structure integration over the Brillouin zone (BZ). The utilized the DFT-D2 proposed by Grimme to model long-range van der Waals interactions (Grimme, 2006). Although these interactions were not expected to significantly affect the bulk properties of the hard solids investigated here, we included the D2 correction at this stage because in future work we expect to study the surfaces of these solids under interactions with COCs at nanoscale, where dispersion effects may play a significant role (Santos-Carballal et al., 2014; Santos-Carballal et al., 2018). The projector augmented wave (PAW) pseudopotential method (Blochl, 1994; Kresse and Joubert, 1999) was used to describe the core electrons and their interactions with the valence electrons, i.e. those in level Fe(3s, 3p, 3d, 4s) and Fe(2s, 2p). The kinetic energy cutoff for the planewave basis set expansion was set at 520 eV for the geometry optimizations, in order to avoid Pulay stress arising from the cell shape relaxations(Mackenzie and Georgi, 2019). The BZ was examined using $11 \times 11 \times 11$ and $5 \times 5 \times 1$ Monkhorst-Pack mesh k-points for bulk and surface calculations, respectively (Monkhorst and Pack, 1976). During relaxation, the energy convergence defining the self-consistency of the electron density was 10^{-5} eV, while the Feynman forces acting on each atom were minimized until they were < 0.01 eV/Å.

Nanomaterials and bulk materials are both fundamental particle types, but the key distinction between nanomaterials and bulk materials is their 'size.' Nanomaterials have dimensions ranging from 1-100 nanometers, at least in one dimension, whereas bulk materials have sizes greater than 100 nanometers in all dimensions. Furthermore, bulk materials exhibit periodic crystalline arrangements occurring periodically in an orderly manner, while nanomaterials lack such characteristics. In addition, they possess differing chemical and physical properties, leading to diverse applications. To simulate Fe_3O_4 (magnetite, *Fd3m* space group and octahedral structure), a cubic inverse spinel structure with a lattice constant of 8.396 Å and eight formula units ($Fe_{24}O_{32}$) was set as an initial structure (Weiss and Ranke, 2002; Yang et al., 2010). The O anions formed a close-packed face-centered cubic (FCC), which was sublatticed with $Fe^{2+}$and Fe^{3+} sites; one site in the tetrahedral coordinate was occupied only by Fe^{3+}, while the other sites in the octahedral coordinate were equally occupied by Fe^{3+} and Fe^{2+} ions. In this work, the magnetite model which used ionic cores was described by the ultrasoft pseudo potential (Vanderbilt, 1990). On the other hand, to simulate FeS (mackinawite, *P4/nmm* space group) (Lennie et al., 1995; Dzade et al., 2013; Dzade et al., 2014), a tetragonal structure consisting of two Fe and two S atoms (Berner, 1962) was set. A non-magnetic state was modeled in this study according to work by Devey et al. which revealed that the stable ground state of FeS is non-magnetic (Devey et al., 2008). This effect has been ascribed not only to the strong covalency of the Fe–S bond but also to extensive d-electron delocalization within the sheets (Vaughan and Ridout, 1971).

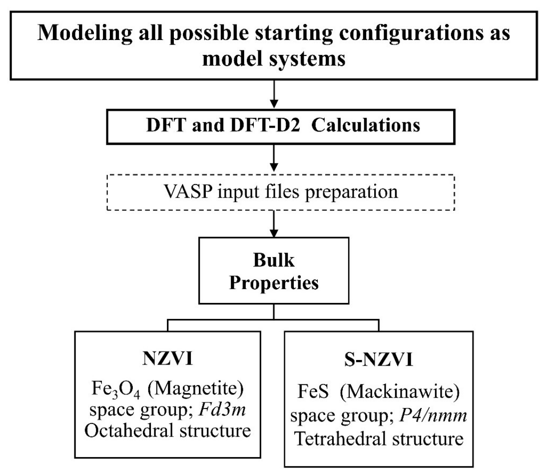

Figure. 1 Flowchart of all the DFT and DFT-D2 steps in this study

As for model evaluation, two major indicators were assessed. Lattice parameters and bond distances optimized by both simulation approaches for both bulk materials were compared with the measured lattice parameters and bond distances of the corresponding bulk materials as experimentally quantified using scanning tunneling microscopy (STM), low-energy electron diffraction (LEED) and X-ray photoelectron diffraction (XPD) in previous studies. While these DFT simulations yield graphical profiles of electron density in states at different energy levels, these profiles cannot be monitored experimentally; rather, only the energy band gap can be experimentally measured using a photoconductive light detector. Thus, the simulated band gaps of the two DFT approaches were compared against the experimental band gap values. Understanding the entire electron density profiles at different energy levels is important, since this governs bulk properties such as specific heat, paramagnetic susceptibility, and other transport phenomena of conductive solids.

4. RESULTS AND DISCUSSION

4.1 Structural Properties of Fe_3O_4 and FeS

Fig. 2 demonstrates the simulated magnetite (Fe_3O_4) unit cells adhering to the face centered cubic pattern. It shows the presence of eight formula units (*z* parameter) within each magnetite unit cell. The super cell parameters optimized using the DFT and DFT-D2 methods are shown in Table 1.

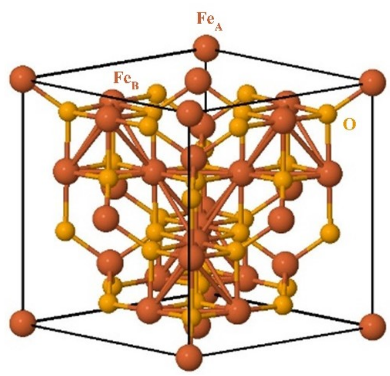

Figure. 2 Schematic illustration of bulk bare-NZVI (Fe_3O_4) Color scheme: Fe = brown and O = orange.

Notably, the super cell parameters optimized by both the DFT and DFT-D2 methods in this study substantially agree with previous experimental results obtained using STM, LEED and XPD (Barbieri et al., 1994; Kim-Ngan et al., 2004). Nevertheless, the super cell parameters optimized by DFT-D2 agree with the experimental results better than those optimized by DFT, suggesting that long-range van der Waals interactions are relevant for modeling magnetite structures. For example, the a = b = c values optimized by DFT-D2 and DFT were 8.324 Å and 8.533 Å, respectively, while the experimental a = b = c value was 8.396 Å. Similarly, the $d(Fe_{tet}\text{-}O)$ values optimized by DFT-D2 and DFT were 1.850 Å and 1.939 Å, respectively, while the experimental $d(Fe_{tet}\text{-}O)$ value was 1.880 Å. Finally, the $d(Fe_{oct}\text{-}O)$ values optimized by DFT-D2 and DFTwere 2.079 Å and 2.082 Å, respectively, while the experimental $d(Fe_{oct}\text{-}O)$ value was 2.070 Å.

Table 1 Optimized bulk structural parameters of magnetite (Fe_3O_4) compared with lattice parameters and bond distances from previous studies.

Unit cell parameters (Å)	**DFT**	**DFT-D2**	**Experimental** (Barbieri et al., 1994; Kim-Ngan et al., 2004)
a = b = c	8.533	8.324	8.396
$d(Fe_{tet}\text{-}O)$	1.939	1.850	1.880
$d(Fe_{oct}\text{-}O)$	2.082	2.079	2.070

In the simulated mackinawite (FeS) structure (Fig. 3), each iron atom was arranged in tetrahedral coordination with sulfur in a square lattice. This yielded edge-sharing tetrahedral layered sheets, which were stacked along the c-axis and stabilized via van der Waals forces (Dzade et al., 2013; Dzade et al., 2014). The sulfur atoms were positioned on the elongated sides of the unit cell. The super cell parameters optimized by DFT and DFT-D2 from this initial structure are shown in Table 2.

Notably, the super cell parameters optimized by both DFT and DFT-D2 in this study agree well with previous experimental results measured using XRD, TEM and XPS (Berner, 1962; Lennie et al., 1997; Jeong et al., 2008). Initially, we carried out geometry optimizations of the FeS structure without accounting for van der Waal forces (i.e., DFT only) and found that the interlayer spacing was overestimated. For example, the lattice parameters produced by DFT after a full geometry optimization converged to $a = b = 3.587$ Å, $c = 5.484$ Å, and c/a ratio = 1.529 Å, which is 12% greater than the c/a ratios; this compares well with the range of previous experimental values reported in Table 2.

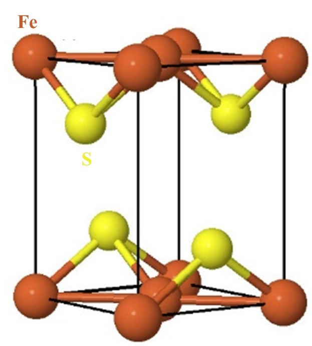

Figure. 3 Schematic illustration of bulk (a) S-NZVI (FeS). Color scheme: Fe = brown, S = yellow.

Nevertheless, as previously mentioned, standard DFT-based methods often result in poor estimation of the inter-layer spacing of most layered structures, including FeS. For this reason, by implementing the DFT-D2 method of Grimme to account for the weak dispersion forces, we predicted the interlayer separation distance as 4.861 Å. This is only 3% lower on average than previous experimental results (Lennie et al., 1997), confirming the importance of this correction to include dispersion forces for an accurate prediction of the interlayer separation distance in FeS. Using the DFT-D2 theoretical method described above and allowing all atoms to fully relax until the required accuracy was reached, we calculated the unit cell parameters at a = b = 3.564 Å and c = 4.861 Å with c/a ratio = 1.364 Å, which compares well with the range of experimental values reported in Table 2 (Berner, 1962; Lennie et al., 1997; Jeong et al., 2008).

Table 2 Optimized bulk structural parameters of mackinawite (FeS) compared with lattice parameters and bond distances from previous studies.

Unit cell parameters (Å)	DFT	DFT-D2	Experiment (Lennie et al., 1997)
a = b	3.587	3.564	3.650
c	5.484	4.861	4.997
c/a	1.529	1.364	1.363
d(Fe-S)	2.160	2.156	2.240
d(Fe-Fe)	2.536	2.520	2.598

4.2 Electronic Structure of Fe_3O_4 and *FeS*

Band structure

Fig. 4 shows the electronic band structure of Fe_3O_4 in the *Fd3m* unit cell simulated by DFT-D2. Red lines show valance bands, while blue lines represent conduction bands. The X-axis illustrates the Brillouin zone (BZ), defined as a Wigner-Seitz primitive cell in the reciprocal lattice specified with systematic symbols of the cell, such as Z, R, and M points (Monkhorst & Pack, 1976), while the Y-axis illustrates the energy of the band (eV). This simulated result provides insight into several measurable or observable physicochemical characteristics of the materials. For example, Fig. 4 shows that the band gap was calculated as 0.82 eV, which is similar to the band gap measured by photoconductor (1.26 eV) (Marand et al., 2014). Moreover, the Z point in the X-axis shows a direct band gap where the valance band and the conduction band meet, confirming the pattern of a metal electronic structure, which is in good agreement with the metal nature of Fe_3O_4. The PBE results indicate that cubic Fe_3O_4 is a half-metallic oxide, with the majority spin band exhibiting insulating or semiconducting behavior and the minority spin band showing metallic behavior.

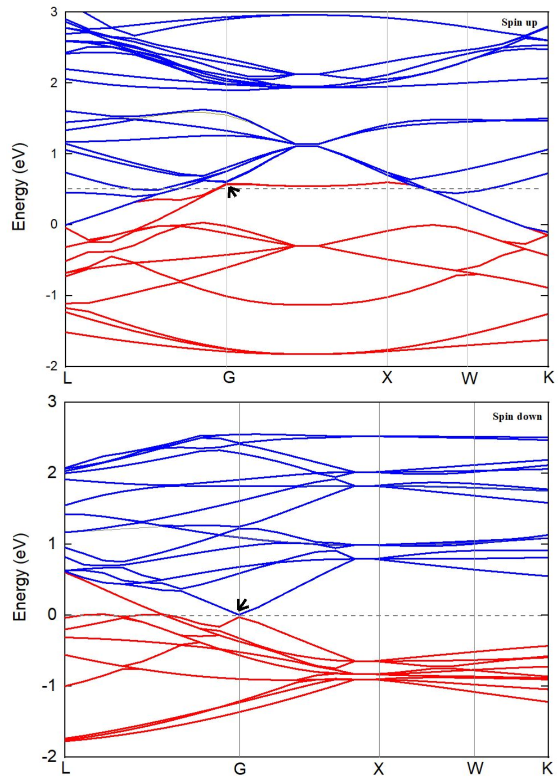

Figure 4 DFT-D2(PBE) electronic band structure of Fe_3O_4 in the *Fd3m* unit cell and. The partial charge density at valence band maximum or conduction band minimum (VBM or CBM, as indicated with an arrow). The Fermi level (=zero of energy, see text) is shown as a dashed line.

Fig. 5 shows the electronic band structure of FeS in the *P4/nmm* unit cell simulated by DFT-D2. Similar to the electronic band structure of Fe_3O_4, the red lines show valance bands while the blue lines represent conduction bands. Similarly, as shown in Fig. 5, the band gap was calculated as 0.60 eV, which is similar to the band gap measured by photoconductor (0.95 eV) (Sun et al., 2011). Moreover, the M point on the X-axis shows a direct band gap where the valance band and the conduction band meet, confirming the pattern of a metal electronic structure, which is in good agreement with the metal nature of FeS.

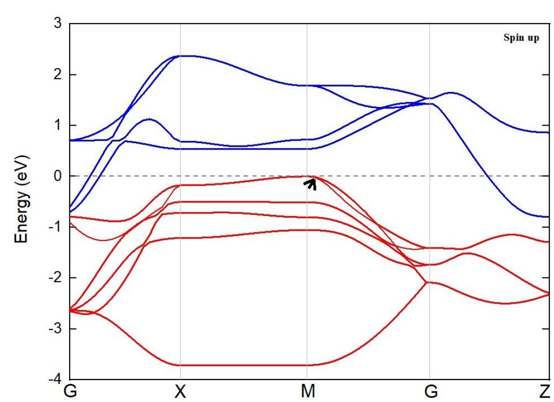

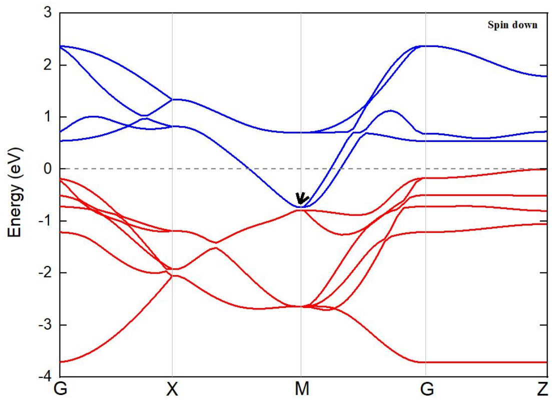

Figure. 5 DFT-D2(PBE) electronic band structure of FeS in the *P4/nmm* unit cell . The partial charge density at valence band maximum or conduction band minimum (VBM or CBM, as indicated with an arrow). The Fermi level (=zero of energy, see text) is shown as a dashed line.

Density of states (DOS)

Moreover, the simulation results also shed some light on phenomena which are technically difficult to directly examine. For example, it is technically challenging to measure electron transfer from Fe^0 through a Fe_3O_4 shell, especially for nanosized particles, but the DFT-D2 can simulate the electronic density of states (DOS) for bulk Fe_3O_4 (Fig. 6(a)), and this can be used to predict electron transfer potential across the iron oxide shell. Theoretically, electron transfer takes place when the energy of electrons in inner orbitals (E) minus the energy of valance electrons (E_f) becomes greater than the Fermi energy. At T = 0 K, the Fermi energy is equal to zero. Thus, according to Fig. 6(a), the DOS corresponding to $E-E_f > 0$ eV represents the electrons which can transfer from the central octahedral-Fe_B layer to the outer tetrahedral-Fe_A layer (Fig.1). Because DOS is essentially the number of different states at a particular energy level that electrons are allowed to occupy, i.e. the number of electron states per unit volume per unit energy, the DOS corresponding to $E-E_f > 0$ represents the number of electron states per unit volume per unit energy which can transfer from the inner orbitals of Fe_3O_4 (i.e., the central octahedral-Fe_B layer) to the outer orbital (i.e. the outer tetrahedral-Fe_A layer). Similarly, for the DOS corresponding to $E-E_f < 0$, electron transfer from the inner orbital to the outer orbital will not occur. In sum, the DOS results in Fig. 6 (b) reveal the potential for electron transfer across the Fe_3O_4, which cannot be experimentally measured.

Interestingly, the simulated DOS of FeS shown in Fig. 6(b) provides potential explanations for the decrease of the NZVI aging effect and enhanced treatment of hydrophobic contaminants by S-NZVI reported in the literature (Fan et al., 2016; Phenrat and Lowry, 2019). For Fe-d states, the DOS corresponding to $E-E_f > 0$ is less than $E-E_f < 0$, while for S-p states, the DOS corresponding to $E-E_f > 0$ is greater than $E-E_f < 0$, suggesting that electron transfer is more favorable through the S than through the Fe of the FeS (Fig. 3).

Thus, NZVI aging is decreased by the presence of FeS because there is less NZVI oxidation due to less electron transfer through the Fe. On the other hand, treatment of hydrophobic COCs such as chlorinated organics is enhanced due to the hydrophobicity and high electron transferability of S producing high electron selectivity and utilization through hydrophobic COCs. S-NZVI generates much more hydroxyl radicals for pollutant degradation through a one-electron transfer pathway than NZVI. Nevertheless, the simulation in this study focused on bulk FeS and not nanoscale FeS. Further modification of DFT-D2 to simulate nanoscale FeS is needed to accurately explain these findings on S-NZVI.

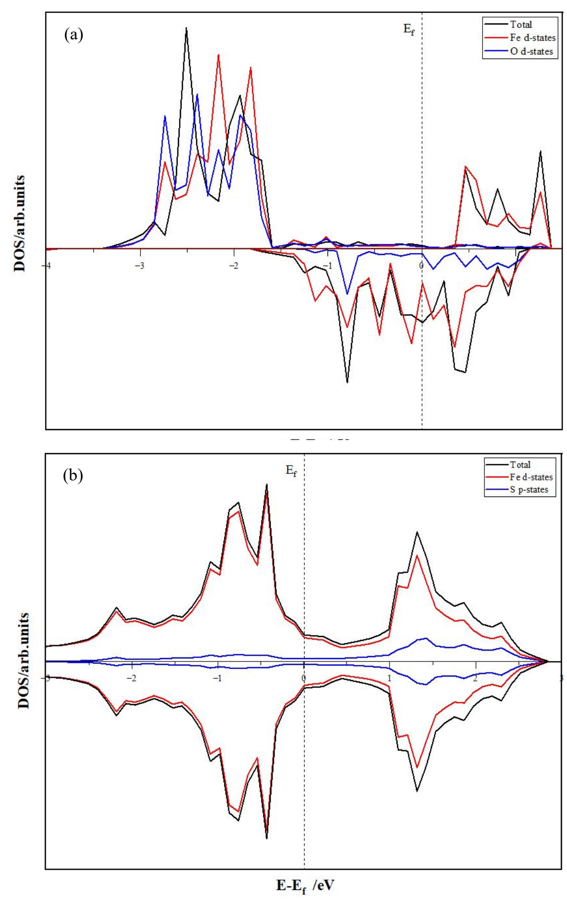

Figure. 6 DFT-D2(PBE) density of states of (a) Fe_3O_4 in the *Fd3m* unit cell and (b) FeS in the *P4/nmm* unit cell . The Fermi level (=zero of energy, see text) is shown as a dashed line.

5. CONCLUSION

We present a computational study of the inversion thermodynamics of the bulk and electronic band structure and density of states (DOS) of bulk Fe_3O_4 and FeS using first principles methods based on the density functional theory. Both DFT and DFT-D2 were implemented, and the results compared with previous experimental results. The simulated properties substantially agree with previous experimental results. Nevertheless, for both bulk Fe_3O_4 and bulk FeS, DFT-D2 performed better than DFT in terms of the accuracy of simulated unit cell parameters. Both DFT and DFT-D2 can also simulate the DOS of both materials effectively. The DOS of Fe_3O_4 supports electron transfer from the central octahedral-Fe_B layer to the outer tetrahedral-Fe_A layer, while the DOS of FeS potentially explains the decrease of the NZVI aging effect and enhanced treatment of hydrophobic contaminants due to sulfidation reported in the literature. This research illustrates that DFT and DFT-D2 can be tools of choice for further modification of interfacial Fe_3O_4 and FeS surface modeling, as well as their interaction with COCs at nanoscale for environmental engineering applications.

6. ACKNOWLEDGMENTS

This work was financially supported by the National Research Council of Thailand (NRCT5-RSA63011-01), 2) the Faculty of Engineering, Naresuan University, Phitsanulok, Thailand (to S. Tongkamnoi), and 3) the Nanostructure Computational Network (NCN) of College of Materials Innovation and Technology, King Mongkut's Institute of Technology Ladkrabang (to Mayuree P. Reilly). We also very much appreciate the permission to access high-performance computers at National e-Science Infrastructure Consortium by National Electronics and Computer Technology Center (NECTEC), Thailand.

7. REFERENCES

Barbieri, A., Weiss, W., Van Hove, M., & Somorjai, G. (1994). Magnetite Fe_3O_4 (111): surface structure by LEED crystallography and energetics. *Surface Science*, *302*(3), 259-279. https://doi.org/10.1016/0039-6028(94)90832-X

Berner, R. A. (1962). Tetragonal iron sulfide. *Science*, *137*(3531),669-669. https://doi.org/10.1126/science.137.3531.669.b

Blochl, P. E. (1994). Projector augmented-wave method. *Phys Rev B Condens Matter*, *50*(24), 17953-17979. https://doi.org/10.1103/physrevb.50.17953

Cornell, R. M., & Schwertmann, U. (2003). *The iron oxides: structure, properties, reactions, occurrences, and uses* (Vol. 664). Wiley-vch Weinheim. https://doi.org/10.1515/CORRREV.1997.15.3-4.533

Dahl, J., & Avery, J. (1986). *Local densityapproximations in quantum chemistry and solid state physics*.

De la Pierre, M., Orlando, R., Maschio, L., Doll, K., Ugliengo, P., & Dovesi, R. (2011). Performance of six functionals (LDA, PBE, PBESOL, B3LYP, PBE0, and WC1LYP) in the simulation of vibrational and dielectric properties of crystalline compounds. The case of forsterite Mg_2SiO_4. *J Comput Chem*, *32*(9), 1775-1784. https://doi.org/10.1002/jcc.21750

Devey, A., Grau-Crespo, R., & De Leeuw, N. (2008). Combined density functional theory and interatomic potential study of the bulk and surface structures and properties of the iron sulfide mackinawite (FeS). *The Journal of Physical Chemistry C*, *112*(29), 10960-10967. https://doi.org/10.1021/jp8001959

Dzade, N., Roldan, A., & de Leeuw, N. H. (2014). The surface chemistry of NO_x on mackinawite (FeS) surfaces: a DFT-D2 study. *Physical Chemistry Chemical Physics*, *16*(29), 15444-15456. https://doi.org/10.1039/C4CP01138D

Dzade, N. Y., Roldan, A., & De Leeuw, N. H. (2013). Adsorption of methylamine on mackinawite (FeS) surfaces: A density functional theory study. *The Journal of Chemical Physics*, *139*(12),124708. https://doi.org/10.1063/1.4822040

Fan, D., O'Brien Johnson, G., Tratnyek, P. G., & Johnson, R. L. (2016). Sulfidation of nano zerovalent iron (nZVI) for improved selectivity during in-situ chemical reduction (ISCR). *Environmental Science & Technology*, *50*(17), 9558-9565. https://doi.org/10.1021/acs.est.6b02170

Grimme, S. (2006). Semiempirical GGA-type density functional constructed with a long-range dispersion correction. *J Comput Chem*, *27*(15), 1787-1799. https://doi.org/10.1002/jcc.20495

Jeong, H. Y., Lee, J. H., & Hayes, K. F. (2008). Characterization of synthetic nanocrystalline mackinawite: crystal structure, particle size, and specific surface area. *Geochimica et cosmochimica acta*, *72*(2), 493-505. https://doi.org/10.1016/j.gca.2007.11.008

Kim-Ngan, N.-T., Soszka, W., & Kozłowski, A. (2004). Studies of an Fe_3O_4 (111) surface by low-energy ion scattering. *Journal of magnetism and magnetic materials*, *279*(1), 125-133. https://doi.org/10.1016/j.jmmm.2004.01.092

Kresse, G., & Furthmüller, J. (1996). Efficiency of ab-initio total energy calculations for metals and semiconductors using a plane-wave basis set. *Computational Materials Science*, *6*(1), 15-50. https://doi.org/10.1016/0927-0256(96)00008-0

Kresse, G., & Hafner, J. (1993). Ab initio molecular dynamics for liquid metals. *Phys Rev B Condens Matter*, *47*(1), 558-561. https://doi.org/10.1103/physrevb.47.558

Kresse, G., & Joubert, D. (1999). From ultrasoft pseudopotentials to the projector augmented-wave method. *Physical Review B*, *59*(3), 1758-1775. https://doi.org/10.1103/physrevb.59.1758

Labanowski, J. K., & Andzelm, J. W. (2012). *Density functional methods in chemistry*. Springer Science & Business Media. https://doi.org/10.1007/978-1-4757-0818-9_5

Lennie, A., Redfern, S. A., Schofield, P., & Vaughan, D. (1995). Synthesis and Rietveld crystal structure refinement of mackinawite, tetragonal FeS. *Mineralogical Magazine*, *59*(397), 677-683.

Lennie, A. R., Redfern, S. A., Champness, P. E., Stoddart, C. P., Schofield, P. F., & Vaughan, D. J. (1997). Transformation of mackinawite to greigite; an in situ X-ray powder diffraction and transmission electron microscope study. *American Mineralogist*, *82*(3-4), 302-309. https://doi.org/10.2138/am-1997-3-408

Liu, Y., Majetich, S. A., Tilton, R. D., Sholl, D. S., & Lowry, G. V. (2005). TCE dechlorination rates, pathways, and efficiency of nanoscale iron particles with different properties. *Environmental Science & Technology*, *39*(5), 1338-1345. https://doi.org/10.1021/es049195r

Liu, Y., Phenrat, T., & Lowry, G. V. (2007). Effect of TCE concentration and dissolved groundwater solutes on NZVI-promoted TCE dechlorination and H_2 evolution. *Environmental Science & Technology*, *41*(22), 7881-7887. https://doi.org/10.1021/es0711967

Mackenzie, K., & Georgi, A. (2019). NZVI synthesis and characterization. *Nanoscale Zerovalent Iron Particles for Environmental Restoration: From Fundamental Science to Field Scale Engineering Applications*, 45-95. https://doi.org/10.1007/978-3-319-95340-3_2

Marand, Z. R., Farimani, M. H. R., & Shahtahmasebi, N. (2014). Study of magnetic and structural and optical properties of Zn doped Fe_3O_4 nanoparticles synthesized by co-precipitation method for biomedical application. *Akush. Ginekol.(Sofiia)*, *15*, 238-247. https://doi.org/10.7508/NMJ.2015.04.004

Monkhorst, H. J., & Pack, J. D. (1976). Special points for Brillouin-zone integrations. *Physical Review B*, *13*(12), 5188-5192. https://doi.org/10.1103/physrevb.13.5188

Néel, L. (1984). Magnetic properties of ferrites: ferrimagnetism and antiferromagnetism. *Physical Chemical & Earth Sciences*(31), 18.

Perdew, J. P., Burke, K., & Ernzerhof, M. (1996). Generalized Gradient Approximation Made Simple. *Physical Review Letters*, *77*(18), 3865-3868. https://doi.org/10.1103/physrevlett.77.3865

Perdew, J. P., Chevary, J. A., Vosko, S. H., Jackson, K. A., Pederson, M. R., Singh, D. J., & Fiolhais, C. (1992). Atoms, molecules, solids, and surfaces: Applications of the generalized gradient approximation for exchange and correlation. *Phys Rev B Condens Matter*, *46*(11), 6671-6687. https://doi.org/10.1103/physrevb.46.6671

Phenrat, T., & Lowry, G. V. (2019). Nanoscale zerovalent iron particles for environmental restoration. *From Fundamental Science to Field Scale Engineering Applications*. https://doi.org/10.1007/978-3-319-95340-3

Phenrat, T., Schoenfelder, D., Kirschling, T. L., Tilton, R. D., & Lowry, G. V. (2018). Adsorbed poly (aspartate) coating limits the adverse effects of dissolved groundwater solutes on Fe^0 nanoparticle reactivity with trichloroethylene. *Environmental Science and Pollution Research*, *25*, 7157-7169. https://doi.org/10.1007/s11356-015-5092-4

Phenrat, T., Thongboot, T., & Lowry, G. V. (2016). Electromagnetic induction of zerovalent iron (ZVI) powder and nanoscale zerovalent iron (NZVI) particles enhances dechlorination of trichloroethylene in contaminated groundwater and soil: proof of concept. *Environmental Science & Technology*, *50*(2), 872-880. https://doi.org/10.1021/acs.est.5b04485

Politzer, P., Seminario, J. M., Concha, M. C., & Murray, J. S. (1993). Some applications of local density functional theory to the calculation of reaction energetics. *Theoretica Chimica Acta*, *85*(1-3), 127-136. https://doi.org/10.1007/bf01374583

Reinsch, B. C., Forsberg, B., Penn, R. L., Kim, C. S., & Lowry, G. V. (2010). Chemical transformations during aging of zerovalent iron nanoparticles in the presence of common groundwater dissolved constituents. *Environmental Science & Technology*, *44*(9), 3455-3461. https://doi.org/10.1021/es902924h

Santos-Carballal, D., Roldan, A., Dzade, N. Y., & de Leeuw, N. H. (2018). Reactivity of CO_2 on the surfaces of magnetite (Fe_3O_4), greigite (Fe_3S_4) and mackinawite (FeS). *Philos Trans A Math Phys Eng Sci*, *376*(2110). https://doi.org/10.1098/rsta.2017.0065

Santos-Carballal, D., Roldan, A., Grau-Crespo, R., & de Leeuw, N. H. (2014). A DFT study of the structures, stabilities and redox behaviour of the major surfaces of magnetite Fe_3O_4. *Phys Chem Chem Phys*, *16*(39), 21082-21097. https://doi.org/10.1039/c4cp00529e

Su, Y., Lowry, G. V., Jassby, D., & Zhang, Y. (2019). Sulfide-modified NZVI (S-NZVI): synthesis, characterization, and reactivity. *Nanoscale Zerovalent Iron Particles for Environmental Restoration: From Fundamental Science to Field Scale Engineering Applications*, 359-386. https://doi.org/10.1007/978-3-319-95340-3_9

Subedi, A., Zhang, L., Singh, D. J., & Du, M.-H. (2008). Density functional study of FeS, FeSe, and FeTe: Electronic structure, magnetism, phonons, and superconductivity. *Physical Review B*, *78*(13), 134514. https://doi.org/10.1103/PhysRevB.78.134514

Sun, R., & Ceder, G. (2011). Feasibility of band gap engineering of pyrite FeS 2. *Physical Review B*, *84*(24), 245211.

Vanderbilt, D. (1990). Soft self-consistent pseudopotentials in a generalized eigenvalue formalism. *Phys Rev B Condens Matter*, *41*(11), 7892-7895. https://doi.org/10.1103/physrevb.41.7892

Vaughan, D., & Ridout, M. (1971). Mössbauer studies of some sulphide minerals. *Journal of Inorganic and Nuclear Chemistry*, *33*(3), 741-746. https://doi.org/10.1016/0022-1902(71)80472-4

Weiss, W., & Ranke, W. (2002). Surface chemistry and catalysis on well-defined epitaxial iron-oxide layers. *Progress in Surface Science*, *70*(1-3), 1-151. https://doi.org/10.1016/s0079-6816(01)00056-9

Wimmer, E. (1996). Computational materials design and processing: perspectives for atomistic approaches. *Materials Science and Engineering: B*, *37*(1-3), 72-82. https://doi.org/10.1016/0921-5107(95)01459-4

Xu, J., Li, H., & Lowry, G. V. (2021). Sulfidized nanoscale zero-valent iron: tuning the properties of this complex material for efficient groundwater remediation. *Accounts of Materials Research*, *2*(6), 420-431. https://doi.org/10.1021/accountsmr.1c00037

Yang, T., Wen, X.-d., Ren, J., Li, Y.-w., Wang, J.-g., & Huo, C.-f. (2010). Surface structures of Fe_3O_4 (111), (110), and (001): A density functional theory study. *Journal of Fuel Chemistry and Technology*, *38*(1), 121-128. https://doi.org/10.1016/s1872-5813(10)60024-2

Zhang, Z., & Satpathy, S. (1991). Electron states, magnetism, and the Verwey transition in magnetite. *Physical Review B*, *44*(24), 13319. https://doi.org/10.1103/PhysRevB.44.13319

8. Biographies

Saranya Tongkamnoi

Challenges in Environmental Science and Engineering (CESE2020) "Understanding surface structure properties and chemisorption of trichloroethylene (TCE) on sulfide-modified nanoscale zerovalent iron (S-NZVI) surfaces using density functional theory (oral presentation)"
ice.saran37@gmail.com

Mayuree P. Reilly

Material simulations for alternative energy and sensor applications, computational chemistry, ab initio and DFT calculation, reaction mechanisms on surfaces, structural, electronic structure, energetic, spectroscopic and dynamic properties of materials.
mayuree.ph@kmitl.ac.th

Tanapon Phenrat

Groundwater and soil remediation, nanomaterials for environmental restoration, groundwater modeling, site characterization, risk assessment.
pomphenrat@gmail.com

NUEJ
Naresuan University
Engineering Journal

Design and Commissioning of Continuously Stirred Anaerobic Bioreactor for Upcycling Carbon Dioxide (CO_2) to Methane (CH_4) via Methanogenesis

Kusuma Rintachai[1], Tanapon Phenrat[1*], Siriwan Wichai[2], Apinun Limmongkon[2], Nusara Yinyom[2]

[1] Department of Civil Engineering, Faculty of Environmental Engineering, Naresuan University,
[2] Faculty of Medical Science, Naresuan University, Phitsanulok, 65000 Thailand

[*]Corresponding author's e-mail: pomphenrat@gmail.com

(Received: 30 May 2023, Revised: 26 November 2023, Accepted: 30 November 2023)

Abstract

Carbon capture and storage (CCS) technology, especially geological storage in depleted oil and gas fields, is essential to achieving the goal of carbon net zero by 2050. Some depleted oil and gas fields contain anaerobic microbes, including methanogens that can transform CO_2 and hydrogen (H_2) to methane (CH_4), which can be extracted and used as a fuel. Thus, subsurface microbiological transformation via methanogens may be key to achieving the large-scale utilization of CO_2. While this concept is exciting and has great potential to promote a circular economy with regard to CO_2 and simultaneously achieve carbon neutrality, extensive research is needed to understand and to maximize methanogen performance. This research preliminary evaluates biogenic gas potential in a neighboring country. Chemical is evaluated. From chemical point of view, the analysis of $\delta^{13}C_{CH4}$ values of the biogenic gas samples from in a neighboring country reveals that the methanogenic pathway is probably dominated by biogenic carbonate reduction. Here, we reveal a design for an automated bioreactor capable of simulating deep subsurface conditions to culture strictly anaerobic methanogens obtained from a gas field in a neighboring country. To simulate deep subsurface conditions, the bioreactor contains a mixture of sediment and anaerobic microbes at an inner pressure of 8 bar and a temperature of 37°C. It has a controlled CO_2 and H_2 feeding system with real-time monitoring of pH, oxidation reduction potential, conductivity, and the transformation of CO_2 and H_2 to CH_4. Even without any optimization, methanogens in this reactor can transform H_2 and CO_2 to CH_4 at a conversion rate of 0.87 to 77.46% of theoretical yield, confirming the survival of active methanogens. This novel reactor facilitates the experimental study of anaerobic methanogenesis in deep subsurface conditions, which is very technically challenging and, to the best of our knowledge, has not previously been performed in Thailand.

Keywords: Automated bioreactor design, Biogenic gas, Carbon capture and storage

1. INTRODUCTION

Anaerobic digestion is an environmental engineering process that transforms the organic load in wastewater into methane (CH_4) with the help of various anaerobic microbes, including synthropes and methanogens (Kong et al., 2019). Methane can then be recovered as a fuel for on-site electricity generation or for heating (Patterson et al., 2017). In addition to wastewater treatment, methanogens also play a crucial role in subsurface biogenic gas formation, accounting for 20% of the world's natural gas reserves (Czauner, Szabó, & Mádl-Szonyi, 2023; Katz, 2011). As shown in Fig. 1(a), large organic molecules including petroleum hydrocarbons in the subsurface can be transformed into either acetate or carbon dioxide (CO_2) and hydrogen (H_2) by fermentative microbes including synthropes (Siddique et al., 2007). The acetate can then be converted to CH_4 by acetoclastic methanogens, while the CO_2 and H_2 can be converted to CH_4 by hydrogenotrophic methanogenic bacteria (*Bioremediation Protocols*, 1997).

Carbon capture and storage (CCS) technology, especially geological storage in depleted oil and gas fields, is essential to achieving the goal of carbon net zero by 2050 (Holz et al., 2021). Since hydrogenotrophic methanogens may already exist in some depleted oil and gas fields, they may substantially benefit CCS projects in depleted oil and gas fields because the methanogens can transform stored CO_2 to CH_4, which can potentially be recovered and reused as a fuel; this will also result in the regeneration of geological CO_2 storage capacity. This transformation will take place if H_2 is available in the subsurface, potentially as a result of other forms of anaerobic microbial activity in the subsurface or if H_2 is produced by water reduction using solar energy and stored in the subsurface (Muhammed et al., 2022). This concept has also been proposed by Prof. Kodie since 1990

(Koide, 1999) as shown in Fig. 1(b). While this concept is exciting and has high potential to promote a circular economy with regard to CO_2 and simultaneously help achieve carbon neutrality, extensive research is needed to understand and maximize methanogen performance.

The most intensive study to understand biogeochemical factors affected biogenic gas formation was conducted by (Ni et al., 2013) for the gas field in Qaidam Basin, China (Ni et al., 2013) evaluated 143 gas samples from different biogenic gas producing locations in China, to investigate the gas origin based on the stable carbon isotopes. The analysis of $\delta^{13}C_{CH4}$ values of biogenic gases reveals that the methanogenic pathway is probably dominated by biogenic carbonate reduction ($\delta^{13}C_{CH4}$ values of biogenic gases mainly from −55‰ to −75‰).

However, since methanogens are strictly anaerobic and CO_2 is gaseous, the design and setup of this kind of bioreactor is challenging and such bioreactors are not currently commercially available. This research provides insight into the design, specification, and setup of a continuously stirred anaerobic bioreactor for transforming CO_2 to CH_4 via methanogenesis. This is a one-of-a-kind bioreactor capable of controlling several parameters including pressure, temperature, pH, oxidation reduction potential (ORP), dissolved oxygen and anaerobic microbial addition, as well as facilitating the continuous online monitoring of CO_2 depletion and CH_4 generation required for exploring the potential of CO_2 upcycling during geological CCS. In addition to the design and the setup of the bioreactor, this study demonstrates its operation without any optimization to demonstrate the baseline for CO_2 transformation by methanogens from a depleted oil and gas field in a neighboring country. The stable carbon isotopes of $\delta^{13}C_{CH4}$ values in the neighboring country were investigated. Out of the 13 gas samples analyzed, 6 exhibited carbon-13 isotopic values in the range of −55.47‰ to −72.44‰, indicating their biogenic origin.

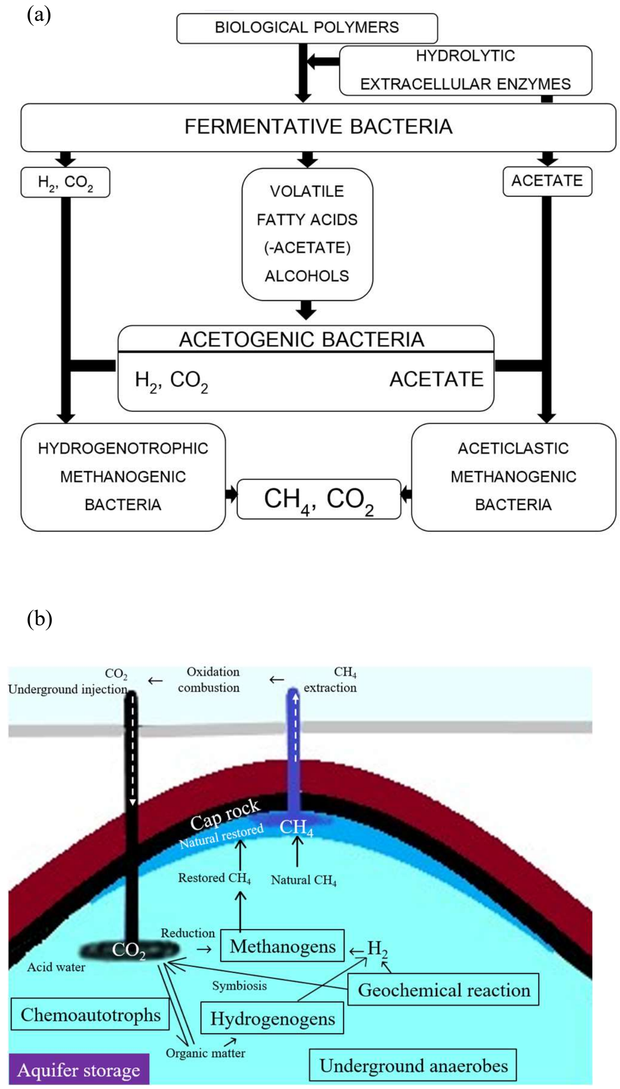

Figure 1 (a) Anaerobic degradation processes including methanogenesis (*Bioremediation Protocols*, 1997; Zehnder, 1988) and (b) concept of subsurface CO_2 transformation to biogenic CH_4 generation (Koide, 1999)

2. DESIGN AND SPECIFICATION OF BIOREACTOR

2.1 Overall Design and P&ID

The design of this bioreactor is based on the principles of continuously stirred tank reactors (CSTRs) (Ruan et al., 2019) and trickle bed reactors (TBRs) (Burkhardt et al., 2019) together with the characteristics of anaerobic subsurface environments. In the laboratory, the bioreactor was continuously stirred and operated by maintaining a continuous flow of CO_2 and H_2 into the reactor at all times. Anaerobic microbes, especially hydrogenotrophic methanogens, transformed CO_2 and H_2 to CH_4, and this process was monitored in real time by means of online gas chromatography. The mixing chamber of the bioreactor was inoculated with a community of anaerobic microbes, including methanogens obtained from an active biogenic natural gas field. The system was strictly anaerobic. Temperature and pressure were monitored and controlled to mimic the subsurface environment, while aqueous chemical parameters including pH, conductivity, and ORP were also continuously monitored. The bioreactor was designed in such as way that samples could be taken from it or more chemicals or microbes added to it. Fig. 2 illustrates the piping and instrumentation diagram (P&ID) of the automated continuously stirred anaerobic bioreactor, while Fig. 3 shows the appearance of the bioreactor.

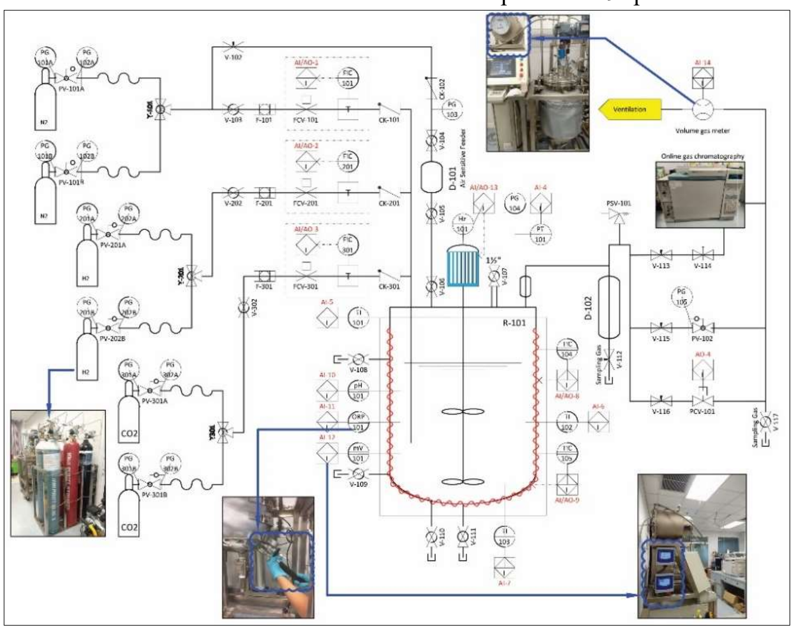

Figure 2 P&ID of continuously stirred anaerobic bioreactor

2.2 Mixing Chambers

Two sizes of stainless steel (SUS304 material) mixing chambers were used in the reactor: a 10-liter vessel and a 40-liter vessel. The equipment and fittings were designed to operate at high pressure (10 bar); Swagelok fittings (tube adapter, male connector, female connector, nut, check valve, valve, cylinder, and flexible hose) were used. The 10-L mixing chamber had a diameter of 27.30 cm and a height of 37.60 cm, with 5-L of headspace. The 40-L mixing chamber, on the other hand, had a diameter of 40.60 cm, a height of 67.76 cm, and 20-L of headspace. Both mixing chambers could be used interchangeably with the rest of the reactor components, including the frame and the gas monitoring unit. The reason for having two mixing chamber sizes was to allow evaluation of the potential for upscaling the methanogenesis process. The mixing chamber was gas-tight and pressurized to allow the creation of a strictly anaerobic environment. In the continuous bioreactor, H2 and CO2 gases, introduced at a 5:1 ratio for highly efficient CH4 generation (Kim et al., 2013), were directed into the mixing chamber. These gases were controlled by an EL-FLOW SELECT Model Series mass flow meter (Bronkhorst) installed at the bottom of the bioreactor to ensure thorough mixing of 5 kilograms of soil with 5 kilograms of soil and 9 liters of water (the media in the bioreactor). The bioreactor had a four-blade, equipped with a magnetic drive and magnetic couplings, manufactured by Amar (Magnetic Drives for High Pressure Reactors) and connected to a SEW-EURODRIVE geared motor (with a maximum working speed of 119 rpm and a maximum torque of 54 Nm).

2.3 Gas Sampling and Monitoring Unit

Automatic gas sampling ports at the top of the bioreactor were directly connected to a gas chromatograph (GC) for online real-time gas analysis. The gas was automatically sampled for analysis when the pressure is greater than 8 bar: when the pressure inside the bioreactor was greater than 8 bar, gas was released at the top of the bioreactor by an ASCO solenoid valve controller and the volume of gas was detected by a drum-type gas meter (Ritter, Germany). A HP6890 GC equipped with a thermal conductivity detector (TCD) was used to quantify CH_4, H_2S, CO_2, and H_2 in the released gas sample. Using capillary columns (HP-PLOT/Q) by setting conditions, the 0.5 mL gas samples were injected into the GC using the sampling valve (an automatic valve directly connected to the bioreactor). The injector temperature was 55 °C and the oven temperature was

60 °C. Argon was used as the carrier gas for the TCD, and the TCD temperature was 180 °C.

2.4 Data Logger and Programmable Logic Controller (PLC)

The bioreactor's parameters were monitored using a Mitsubishi touch-screen programmable logic controller (PLC) connected to a Mettler Toledo Pt4805-DXK-S8/120 ORP sensor (-2000 mV to 2000 mV (Technology, 2021)), a Mettler Toledo InPro7100i/12/120/4435 conductivity sensor (0.02 to 500 mS/cm), a Mettler Toledo InPro4260i/SG/120 pH sensor (pH 0 to 14), a WIKA temperature transmitter (-30 to 300 °C), and a WIKA pressure transmitter (-1 to 15 bar), as shown in Fig. 4. The sensor probes for ORP, conductivity, and pH measurement were calibrated using standard solutions (Thermo Fisher Scientific for ORP and conductivity, Ajax Finechem for pH). The temperature of the reactor was maintained at 37.0 ± 1.0 °C by a heater band operating at 3000W, 220V and 50Hz.

Moreover, the data recorded, controlled and monitored by means of the touch screen display were saved using a data logger and exported as an Excel spreadsheet.

Figure 3 Photo of a bioreactor with a 15-L mixing chamber

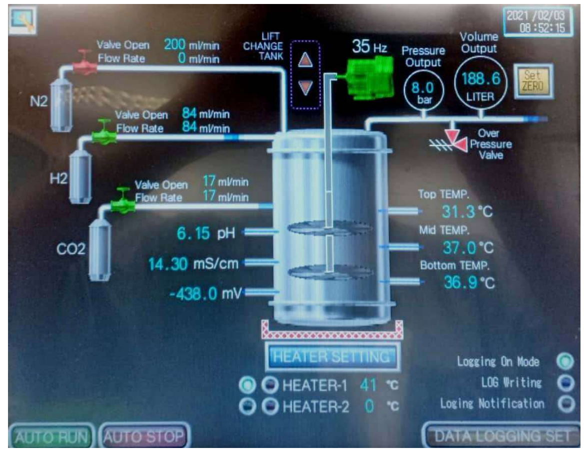

Figure 4 Monitoring and control of bioreactor

2.5 Liquid Feeder and Liquid and Solid Sampling

A liquid substrate feeder in the form of a cylindrical sampling bomb was used as a port through which to add substrate and anaerobic microorganisms to the bioreactor while avoiding oxygen intrusion. During substrate addition using the bomb, we flushed the bomb with nitrogen gas to replace the oxygen.

In addition, a sampling port was positioned at the bottom of the reactor to allow solids or liquids to be removed from it. This port could also be used to drain water from the reactor if necessary.

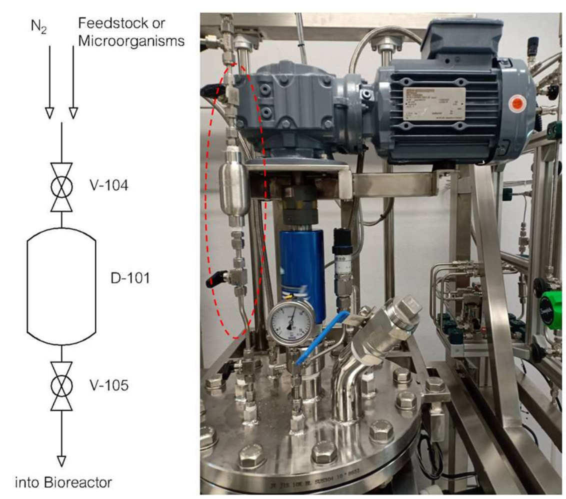

Figure 5 Concept for liquid feeder

3. Bioreactor Commissioning and Operation

The bioreactor mixes CO_2, soil slurry, and methanogens together and monitors CO_2 transformation, as well as changes in geochemical parameters, in real time. To make a soil slurry, water and soil slurry were placed in the vessel before the vessel was closed using the PLC's touchscreen. After the anaerobic system was set up in the bioreactor, a vacuum was created at -0.9 bar using a vacuum pump (Vacuubrand). Next, N_2 was fed into the water and soil slurry to flush oxygen gas out of the system. The ORP probe showed a value of sub-zero millivolts, confirming anaerobic conditions. The mixing chamber was stirred by the motor at 87 rpm (35 Hz).

Next, a total of 190 mL of anaerobic bacteria, including hydrogenotrophic methanogens in a culture medium (tryptone soya broth, basal medium), were introduced to the bioreactor using the cylindrical sampling bomb (Fig. 5). The microorganisms were then cultured in the bioreactor for 9 days following startup. H_2 (99.99% purity) was fed into the bioreactor at 84 mL/min while CO_2 (95% purity) was fed at 17 mL/min, with a mass flow controller used to ensure a continuous flow (with real-time monitoring). When the pressure exceeded 8 bar, the system drained gas to the GC to allow quantification of gas composition and to maintain the pressure in the bioreactor. The methane yield data was thus not reported as a cumulative yield, but instead as real-time methane yield (i.e., methane yield per day). The recording parameters were saved to a memory card every 300 seconds.

4. Performance Evaluation of Bioreactor

4.1 Control and Monitoring of Anaerobic Environment

Fig. 6 illustrates the control and monitoring of the geochemical parameters of the bioreactor, including pH, temperature, conductivity, and ORP. pH ranged from 6.16 to 7.65 (Fig.6(a)) while temperature ranged from 36.8 to 37.7 ºC (Fig.6(b)) as programmed; both these ranges are suitable for mesophilic methanogens (Schiraldi & Rosa, 2014). The conductivity ranged from 10.42 mS/cm to 14.98 mS/cm (Fig. 6(c)), representing the content of water-soluble inorganic compounds such as SO_4^{2-} and Fe^{3+} (Agency, 2012; Authority, 2014). Moreover, during the 21 days of the test, ORP was in the range of -439.0 mV to -537.8 mV (Fig.6(d)), which is clear evidence of a strictly anaerobic system favorable for methanogenesis (below -330 mV) (Hungate, 1969; Mauerhofer et al., 2019). In sum, the commission of the bioreactor was successful in providing suitable conditions for methanogenesis.

4.2 Monitoring CO_2 Transformation and CH_4 Formation

Using a 10-L mixing chamber, Fig. 7 (a) illustrates the flow of CO_2 and H_2 being fed into the bioreactor (at a H_2-to-CO_2 ratio of 5:1) as well as the outlet flow from the bioreactor. Notably, both inlet and outlet flows were stable over the experimental period. Fig. 7(b) shows the results of monitoring the major gas components as a function of time. In addition to CO_2 and H_2, which were the inlet gas components, a substantial portion of CH_4 was continuously detected at the outlet over the experimental period. This confirms the continuous formation of CH_4 from CO_2 and H_2 9 days after the initial incubation of anaerobic microbes. Fig. 7(c) illustrates the kinetics of CH_4 formation as CH_4 yield (% of theoretical yield) and CH_4 concentration (% volume) in the bioreactor. Utilizing CO_2 and H_2 at a ratio of 1:5 as the feedstock, the theoretical CH_4 yield is 0.0167 mole. During 21 days of continuous operation in the bioreactor, the maximum yield of CH_4 formation by methanogens, without any optimization or manipulation, ranged from 0.87 to 77.46% of the theoretical yield per day. This corresponded to a volume percentage of 0.072% to 6.47%. in comparison, the control group, which did not receive CO_2 and H_2, showed CH4 formation at a volume percentage of 0.014% to 0.57%, as illustrated in Fig.7(d). Concentrations of CO_2 and H_2 were 0.073 to 18.05% by volume and 0 to 75.25% by volume, respectively (see Fig.7(a)) while the total gas outflow rate was 9.52 to 80.42 mL/min (see Fig.7(a)). In sum, the bioreactor generated anaerobic conditions suitable for incubating anaerobic microbes, which produced up to 77.46% of the maximum theoretical CH_4 yield.

5. Conclusion and Recommendations

Table 1 summarizes the specifications and working conditions of the bioreactor developed in this study. The design and commissioning of the bioreactor was successful in producing anaerobic conditions and incubating anaerobic microbes, especially methanogens, for CO_2 upcycling. The bioreactor controlled and monitored the inlet gases, the products, and the geochemical parameters in the mixing chamber effectively. Using anaerobic microbes, including hydrogenotropic methanogens, with CO_2 and H_2 as the feedstock, the CH_4 yield of the 10-L bioreactor was 77.46% of the theoretical yield. This reactor serves as an effective tool with which to study the subsurface transformation of CO_2. This represents an emerging technology that not only facilitates the geological storage of CO_2 but can also turn it into fuel, generating significant value added from CO_2 and thus forming an important component of a circular economy and an essential incentive for CO_2 management.

The recommendations from this research regarding the competition in hydrogen gas utilization between hydrogenotrophic methanogens and other microbial groups, such as iron-reducing bacteria and sulfate-reducing bacteria, emphasize the necessity of a balanced and excessive supply of hydrogen gas. This balance is crucial to counteract carbon dioxide in hydrogenotrophic methanogenesis by microorganisms. For larger-scale applications, directly introducing high-grade hydrogen gas may not be suitable. On the contrary, exploring ways to cultivate bacteria capable of generating hydrogen gas, thriving in subsurface environments, and proliferating offers a sustainable approach for hydrogen gas production.

a)

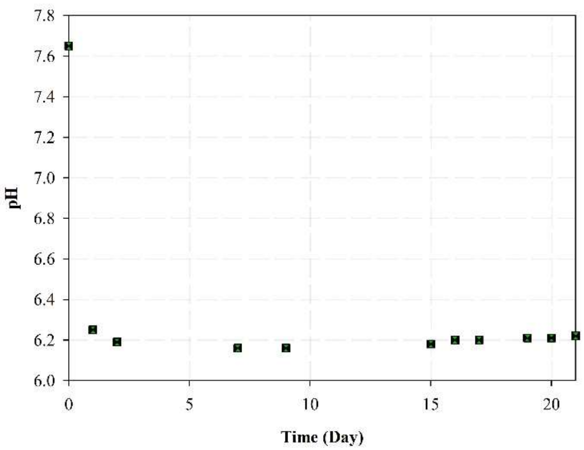

b)

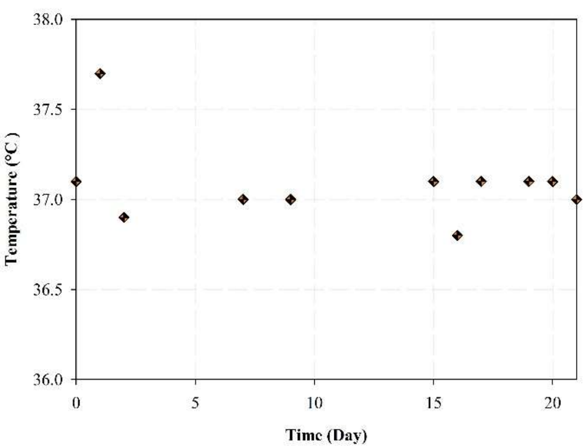

c)

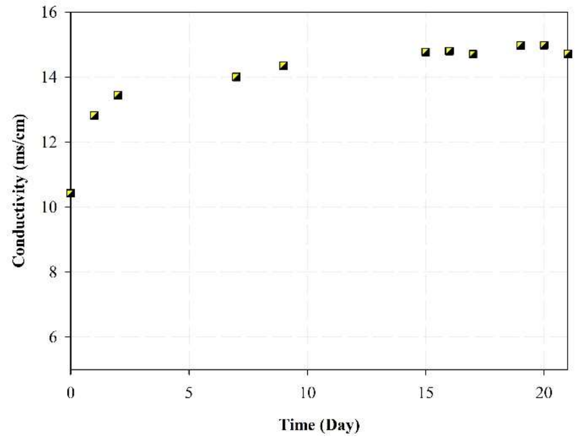

d)

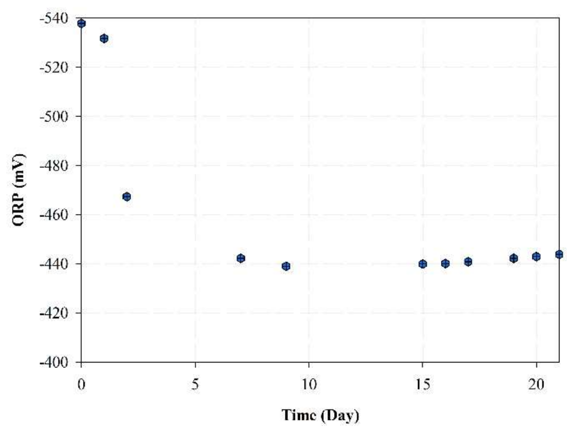

Figure 6 Monitoring of (a) pH, (b) temperature, (c) conductivity, (d) ORP

a)

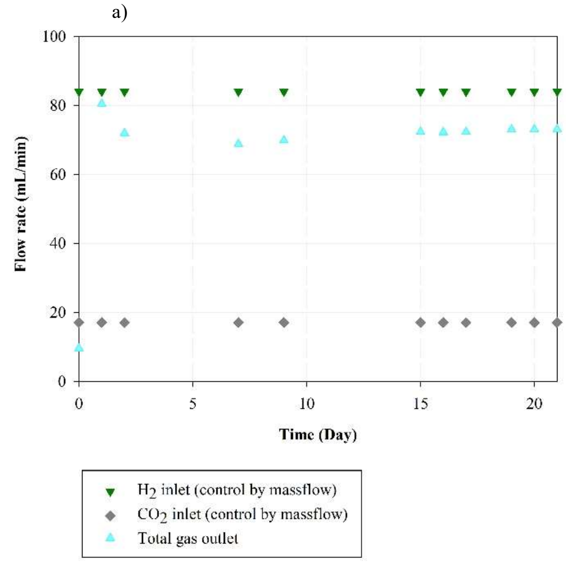

b)

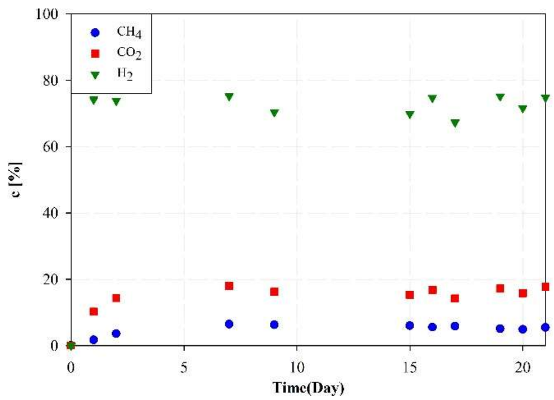

c)

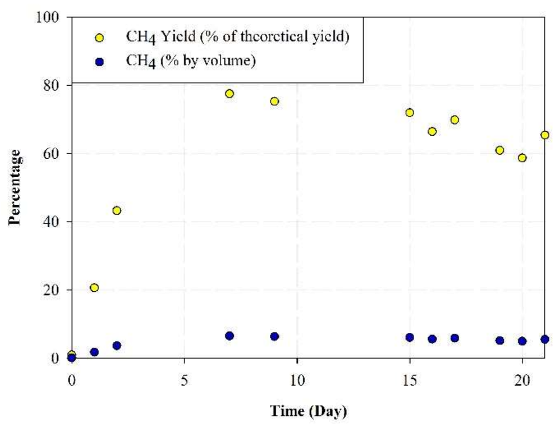

d)

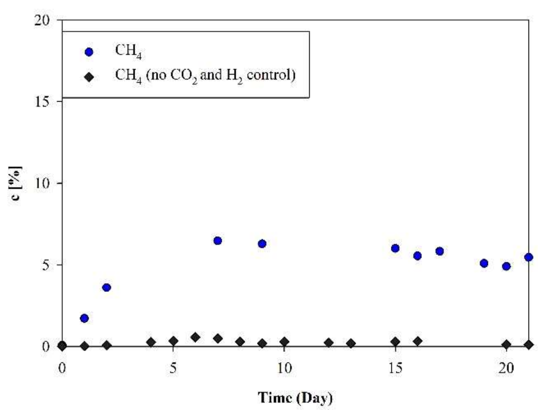

Figure 7 (a) monitoring of inlet and outlet flow rates, (b) gas components of the outlet, (c) kinetics of CH_4 yield and CH_4 concentration as a result of bioreactor testing, and (d) CH_4 concentration as a result of CO_2 and H_2 as the feedstock and no CO_2 and H_2 control bioreactor testing

Table 1 The summary specification and working range of the bioreactor

Item	Specification	Monitoring and controlling work
Pressure (headspace of the bioreactor)	0 to 10 bar	Working at 8 bar by means of continuous system
Oxidation reduction potential (ORP)	-2000 to 2000 mV (Technology, 2021)	ORP was in the range of -439.0 mV to -537.8 mV, which is suitable for anaerobic conditions.
GC /HP-PLOT/Q Column	Detect nonpolar and polar compounds in samples, such as hydrocarbons, CH_4, CO_2, H_2, and H_2S (Technologies, 2022; Zhou & Wang, 2003)	CH_4, CO_2, and H_2 levels monitored as 0.072 to 6.47% vol, 0.073 to 18.05% vol, and 0 to 75.25% vol, respectively. Monitored by gas chromatography (GC), as shown in section 2 on materials and methods (6).
Mass flow Controller	Flow rates of mass flows of gases are 10 to 500 ml/min for CO_2, 20 to 1000 ml/min for N_2, and 10 to 500 ml/min for H_2.	Working at 100 ml/min for N_2, 17 ml/min for CO_2, and 84 ml/min for H_2.
Heating	Maximum 120 °C	Working at 37 °C
Mechanical pressure resistance for pH, ORP, and conductivity sensor	Mechanical pressure resistance at 15 bar for ORP and pH and 10 bar for conductivity (25 °C)	Working at 8 bar
Volume gas meter	Measuring range is 6 to 360 l/hr	Monitored via the touch screen every 0.1 liters
Data logging	Parameters saved every 5 to 1200 seconds.	Recording parameters saved every 300 seconds
Relief valve	The safety device is set to a pressure of 12.5 bar.	When the pressure in the bioreactor exceeds 12.6 bar, the system will release the pressure and trigger an audible alert to notify the operator.

6. ACKNOWLEDGMENTS

This research has received funding support from the NSRF via the Program Management Unit for Human Resources & Institutional Development, Research and Innovation (Grant Number B40G660037). Moreover, we gratefully acknowledge support from the Faculty of Environmental Engineering, Naresuan University.

Special thanks to Suchat Pongchaiphol (King Mongkut's University of Technology Thonburi (KMUTT), Bangkok, Thailand) for engineering support and services.

7. References

Agency, U. S. E. P. (2012). Water: Monitoring & Assessment. Retrieved 03/31/2022, 2022, from https://archive.epa.gov/water/archive/web/*html*/vms59.html

Authority, M. W. (2014). Conductivity. from https://www.mwa.co.th/ewt_news.php?nid=13321

Bedoić, R., Dorotić, H., Rolph Schneider, D., Čuček, L., Ćosić, B., Pukšec, T., & Duić, N. (2021). Synergy between feedstock gate fee and power-to-gas: An energy and economic analysis of renewable methane production in a biogas plant. *Renewable Energy, 173*, 12-23. doi: https://doi.org/10.1016/j.renene.2021.03.124

Bioremediation Protocols. (1997). (D. Sheehan Ed.): Humana Press.

Burkhardt, M., Jordan, I., Heinrich, S., Behrens, J., Ziesche, A., & Busch, G. (2019). Long term and demand-oriented biocatalytic synthesis of highly concentrated methane in a trickle bed reactor. *Applied Energy, 240*, 818-826. doi: doi:10.1016/j.apenergy.2019.02.076

Czauner, B., Szabó, Z., & Mádl-Szonyi, J. (2023). Basin-Scale Hydraulic Evaluation of Groundwater Flow Controlled Biogenic Gas Migration and Accumulation in the Central Pannonian Basin. *MDPI, 15*(18). doi: 10.3390/w15183272

Fernández-Prini, R., Aires, B., Alvarez, J. L., Aires, B., & Harvey, A. H. (2003). Henry's Constants and Vapor–Liquid Distribution Constants for Gaseous Solutes in H2O and D2O at High Temperatures. *Physical and Chemical*. doi: https://doi.org/10.1063/1.1564818

Holz, F., Scherwath, T., Granado, P. C. d., Skar, C., Olmos, L., Ploussard, Q., . . . Herbst, A. (2021). A 2050 perspective on the role for carbon capture and storage in the European power system and industry sector. *Energy Economics, 104*. doi: https://doi.org/10.1016/j.eneco.2021.105631

Hungate, R. E. (1969). Chapter IV A Roll Tube Method for Cultivation of Strict Anaerobes. *Methods in Microbiology, 3*, 117- 132. doi:https://doi.org/10.1016/S0580-9517(08)70503-8

Katz, B. J. (2011). Microbial Processes and Natural Gas Accumulations. *The Open Geology Journal,, 5*, 75-83. doi: 10.2174/1874262901105010075

Kim, S., Choi, K., & Chung, J. (2013). Reduction in carbon dioxide and production of methane by biological reaction in the electronics industry. *International Journal of Hydrogen Energy, 38*(8), 3488-3496. doi: 10.1016/j.ijhydene.2012.12.007

Koide, H. (1999). GEOLOGICAL SEQUESTRATION AND MICROBIOLOGICAL RECYCLING OF CO2 IN AQUIFERS. *Paper presented at the Greenhouse Gas Control Technologies, Proc. 4th Int. Conf. on Greenhouse Gas Control Technologies*.

Kong, D., Zhang, K., Junfeng Liang, Wenxuan Gao, & author, L. D. (2019). Methanogenic community during the anaerobic digestion of different substrates and organic loading rates. *Microbiologyopen, 8*(5). doi: 10.1002/mbo3.709

Magnetic Drives for High Pressure Reactor. Retrieved 03/31/2022, 2022, from https://amarequip.com/magnetic-drives-for-high-pressure-reactor

Mauerhofer, L.-M., Pappenreiter, P., Paulik, C., Seifert, A. H., ernacchi, S., & Rittmann, S. K.-M. R. (2019). Methods for quantification of growth and productivity in anaerobic microbiology and biotechnology. *Folia Microbiologica*, 321–360. https://doi.org/10.1007/s12223-018-0658-4

Muhammed, N. S., Haq, B., Shehri, D. A., Al-Ahmed, A., Rahman, M. M., & Zaman, E. (2022). A review on underground hydrogen storage: Insight into geological sites, influencing factors and future outlook. *Energy Reports, 8*, 461-499. doi: https://doi.org/10.1016/j.egyr.2021.12.002

Ni, Y., Dai, J., Zou, C., Liao, F., Shuai, Y., & Zhang, Y. (2013). Geochemical characteristics of biogenic gases in China. *International Journal of Coal Geology, 113*, 76-87. doi:10.1016/j.coal.2012.07.003

Patterson, T., Savvas, S., Chong, A., Law, I., Dinsdale, R., & Esteves, S. (2017). Integration of Power to Methane in a waste water treatment plant – A feasibility study. *Bioresour Technol, 245*, 1049-1057. doi: https://doi.org/10.1016/j.biortech.2017.09.048

Rehman, A., Ma, H., Ahmad, M., Irfan, M., Traore, O., & Chandio, A. A. (2021). Towards environmental Sustainability: Devolving the influence of carbon dioxide emission to population growth, climate change, Forestry, livestock and crops production in Pakistan. *Ecological Indicators, 125*. doi: https://doi.org/10.1016/j.ecolind.2021.107460

Rice, D. D., & Claypool, G. E. (1981). Generation, Accumulation, and Resource Potential of Biogenic Gas1. *AAPG Bulletin, 65*(1), 5–25. doi: https://doi.org/10.1306/2F919765-16CE-11D7-8645000102C1865D

Ruan, D., Zhou, Z., Pang, H., Yao, J., Chen, G., & Qiu, Z. (2019). Enhancing methane production of anaerobic sludge digestion by microaeration: Enzyme activity stimulation, semi-continuous reactor validation and microbial community analysis. *Bioresour Technol, 289*, 121643. doi: 10.1016/j.biortech.2019.121643

Sander, R. (2015). Compilation of Henry's law constants (version 4.0) for water as solvent. *Atmospheric Chemistry and Physics, 15*(8). doi: https://doi.org/10.5194/acp-15-4399-2015, 2015.

Sander, S. P., Abbatt, J., Barker, J. R., Burkholder, J. B., Friedl, R. R., Golden, D. M., Wine, P. H. (2011). Chemical Kinetics and Photochemical Data for Use in Atmospheric Studies, Evaluation No. 17.

Schiraldi, C., & Rosa, M. D. (2014). *Encyclopedia of Membranes* (E. Drioli & L. Giorno Eds.): Springer, Berlin, Heidelberg.

Seifert, A. H., Rittmann, S., & Herwig, C. (2014). Analysis of process related factors to increase volumetric productivity and quality of biomethane with Methanothermobacter marburgensis. *Applied Energy, 132*, 155–162. doi:http://dx.doi.org/10.1016/j.apenergy.2014.07.002

Show, K.-Y., Lee, D.-J., & Chang, J.-S. (2011). Bioreactor and process design for biohydrogen production. *Bioresour Technol, 102*, 8524–8533. doi: 10.1016/j.biortech.2011.04.055

Singh, J., Kaushik, N., & Biswas, S. (2014). Bioreactors – Technology & Design Analysis. *THE SCITECH, 01*(06).

Susilawati, R., Papendick, S. L., Gilcrease, P. C., Esterle, J. S., Golding, S. D., & Mares, T. E. (2013). Preliminary investigation of biogenic gas production in Indonesian low rank coals and implications for a renewable energy source. *Asian Earth Sciences*. doi: 10.1016/j.jseaes.2013.08.024

Technologies, A. (2022). HP-PLOT Q Columns. Retrieved 03/31/2022, 2022, from https://www.agilent.com/en/product/gc-columns/plot-gc-columns/hp-plot-q-columns

Technology, S. S. (2021). Mettler Toledo – Redox sensor. Retrieved 03/31/2022, 2022, from https://www.sea-sun-tech.com/product/mettler-redox/Wellinger, A.,

Murphy, J., & Baxter, D. (2013). *The biogas handbook Science, production and applications*: Woodhead Publishing.

Wolfgang, D., Lauckner, J., Liu, Z., Svensson, U., & Buhmann, D. (1996). The kinetics of the reaction CO2 + H20 + H+ + HCO3-, as one of the rate limiting steps for the dissolution of calcite in the system H2O-CO2-CaC03. *Geochimica et Cosmochimica Acta, 60*. doi: 10.1016/0016-7037(96)00181-0

Zehnder, A. J. B. (1988). *Biology of Anaerobic Microorganisms (Wiley Series in Ecological and Applied Microbiology) 99th Edition* (A. J. B. Zehnder Ed.): Wiley-Interscience; 99th edition (September 7, 1988).

Zhou, Y., & Wang, C. (2003). Analysis of Permanent Gases and Methane with the Agilent 6820 Gas Cromatograph.

Zinder, S. H. (1993). *Physiological Ecology of Methanogens*.

8. BIOGRAPHIES

Miss Kusuma Rintachai

Department of Civil Engineering, Faculty of Environmental Engineering, Naresuan University, Phitsanulok, Thailand

Associate Professor Dr. Tanapon Phenrat

Department of Civil Engineering, Faculty of Environmental Engineering, Naresuan University, Phitsanulok, Thailand

Dr. Siriwan Wichai

Faculty of Medical Science, Naresuan University, Phitsanulok, Thailand

Associate Professor Dr. Apinun Limmongkon

Faculty of Medical Science, Naresuan University, Phitsanulok, Thailand

Miss Nusara Yinyom

Faculty of Medical Science, Naresuan University, Phitsanulok, Thailand

NUEJ
Naresuan University
Engineering Journal

Experimental investigation on granular fodder flow characteristics during discharge period in silo

K Santhisan[1], K Kraitong[1,*,] and S Mailoungkard[2]

[1] Department of Mechanical Engineering, Faculty of Engineering, Naresuan University, Phitsanulok, Thailand.
[2] CPF (Thailand) Public Company Limited, Samokhae, Muang Phitsanulok District, Phitsanulok 65000, Thailand.

[*]Corresponding author e-mail: kwanchaik@nu.ac.th

(Received: 21 July 2023, Revised: 12 December 2023, Accepted: 19 December 2023)

Abstract

The purpose of this study is to conduct an experimental investigation on granular fodder flow characteristics during discharge period in silos. The pressure on the silo wall and the mass flow rate of pellets feed stored in the silo for 1 hour were determined with the laboratory-scale steel and fiberglass silos. Additionally, the parametric study of four angles of a 55 mm diameter outlet conical hopper such as 10, 20, 30, and 45 degrees were done in this testing. From the results, the average wall pressure of the steel silo in the discharge period was more than that of the fiberglass silo. Both silos presented the minimum and maximum mass flow rate occurring on a hopper angle of 45 degrees and 10 degrees, respectively. When considering experimental results of the wall pressure and the average mass flow rate, it could be concluded that the flow patterns of granular fodder during discharge period in both steel and fiberglass silos were funnel flow patterns.

Keywords: Discharge process, Granular fodder flow, Pattern flow, Silo

1. INTRODUCTION

The feed industry is an agricultural processing industry that uses silos to store the granular product. Most silos in this industry are a cylindrical silo with conical hopper as shown in Figure 1.

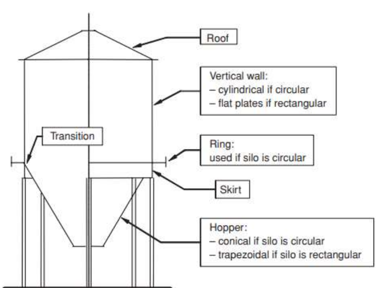

Figure 1 Terminology for parts of a hopper silo. (Rotter, 2009)

However, in the process of waiting for transportation, it was found that the feed stored in silos for a long time can be introduced to blockage of flow above the silo exit channel during discharge process. In other words, the material can flow out for a certain period of time, and then jamming occurs stagnant or immobile. This is the primary issue causing significant damage to the feed industry. As the result, various technologies are being employed to assist in the resolution of this issue. For example, some devices are installed to allow vibrating, taping, or shaking on the silo. Additionally, the usage of blowing wind for destroying the material's adhering ability is implemented. Many industrial silos have been damaged by popular solutions such as knocking from the outside with a heavy hammer for breaking down the material that sticks together and allowing it to move out as shown in Figure 2.

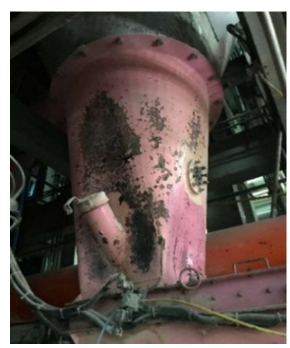

Figure 2 Hammer rash.

There are two main processes of material flow within the silo as filling process and discharge process. When the outlet is opened, the material begins to gravitationally move out of the silo. The movement of objects could be classified into three flow patterns: mass flow, funnel flow, and expand flow as shown in Figure 3. For the mass flow, it is defined that all the material inside the silo was constantly moving out of the silo. The formation of this flow pattern is introduced in hoppers with small tilt angles and sufficiently smooth silo walls. There are no areas that cause an abrupt change in the direction of movement. Hence this type of flow pattern is suitable for the operation of industrial silos and considerable to be the best flow pattern (Grudzien & Gonzalez, 2013). Unlike the funnel flow, material located only in the center of the silo is allowed to move out while some material is fixed to the silo wall. This phenomenon creates dead zones within the silo. In the case of a combination of the two flow forms, only the material located in the core bin region and the hopper area are all material outflow phenomena.

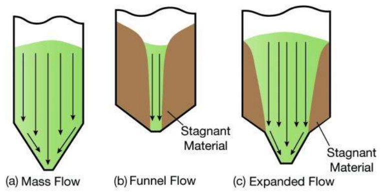

Figure 3 Flow pattern a) Mass flow b) funnel flow and (c) Expanded flow. (Greg Mehos et al., Apr 2018)

As mentioned above, the design of silos with effective particle outflow could clearly be one of the high-priority improvement issues in the feed industry. In engineering design, it is necessary to consider the pressure inside the silo and the maximum force exerted on the wall, combined with the mass flow rate due to the material flowing out, it is used to analyze mass flow/funnel flow behavior in bins or hoppers. (Askegaard & Munch-Andersen, 1985; Ayuga, Guaita, Aguado, & Couto, 2001; Härtl et al., 2008; Ramírez, Nielsen, & Ayuga, 2010; Zhong, Ooi, & Rotter, 2001). Uñac et al. (Uñac, Vidales, Benegas, & Ippolito, 2012) conducted an experimental study of the influence of different silo-shape factors and outlet sizes that affect the mass flow rate of quartz particles. The result of the study has shown that the channel size factor significantly affects the flow rate, as well as Wang et al. (Wang et al., 2022) studies the flow patterns of barre and plastic pellets, and the pressure at the flat bottom aluminum silo walls, which changes the flow pattern from a funnel flow to a mass flow. The result of the study has shown that the filling process strongly affects the flow pattern and pressure of the pellets, while the barre is only slightly affected. In addition, Wang et al. (Wang et al., 2020) also studied the pressure created during the flow process of mass-volume materials in an experiment with conical silos. The result of the study found that the stress fluctuation at the hopper top is independent of the outlet diameter, while the period of the stress fluctuation decreases with the increase of the outlet diameter. As well, many researchers conducted studies on the pressure within silos during the discharge process of various materials (An, Wang, Fang, Liu, & Liang, 2021; R. Gandia, Júnior, Carlos Gomes, Coimbra de Paula, & Dornelas, 2021; R. M. Gandia, Gomes, Paula, Oliveira Junior, & Aguado Rodriguez, 2021; Tang, Lu, Guo, & Liu, 2021; Walker, 1966) to guide the design of silos for further maximize efficiency. However, a few researchers are considering the flow of feed materials in silos. Hence, this research project aims to conduct an experimental study of the pressures that occur in silo walls and the mass flow rate of fodder preserved in a silo for 1 hour during the discharge process. The testing silos, moreover, are made of steel and fiberglass which have a conical hopper with an outlet diameter of 55 mm and an inclination of 10, 20, 30, and 45 degrees.

2. Materials and methods.

2.1 Fodder

The fodder product used in the test was manufactured by CPF (Thailand) Public Company Limited. The bulk density was 444.45 kg/m^3, the average diameter was 2 mm and the average length was 5 mm. The moisture content was 13% on average; it was evaluated by a moisture analyzer and can be used to accurately determine the moisture content in feed samples. In each trial, the amount of fodder was 15 kg as shown in Figure 4.

Figure 4 fodder material.

2.2 Characteristics of laboratory-scale silos

The laboratory-scale silo was divided into two parts: a bin and a hopper with varied inclination angles of 10, 20, 30, and 45 degrees as well as an outlet size of 55 mm as seen as Figure 5.

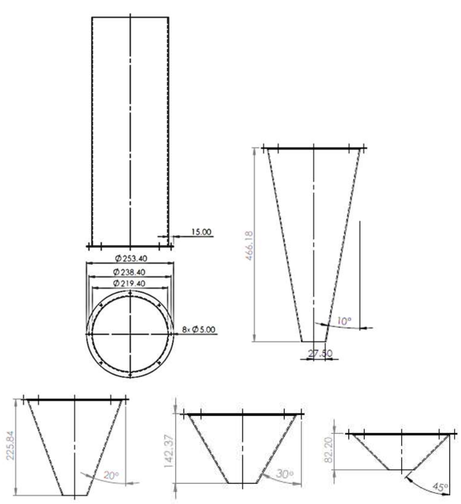

Figure 5 The scale of the silo laboratory

Testing silos were made from steel and fiberglass materials which were based on feed industrial silo's characteristics. The one-tenth size scale reduction of an actual industrial silo was applied to this experiment. The characteristics of testing silos are illustrated in Figure 6 .

a)

b)

Figure 6 Laboratory-scale silos: a) Steel silo b) Fiberglass silo.

2.3 Laboratory set-up

The two main measuring instruments were installed on the test rig such as the load cell for measuring the material weight and the force sensing resistors (FSR) for measuring normal pressure acting on the wall during the discharge process. Three load cells with a weight range from 0 to 50 kg were equipped to measure the weight of the changing feed as shown installation points in Figure 7.

Figure 7 Location of three load cells.

The bin wall and hopper wall of lab-scale silos were attached with Force Sensing Resistors (FSR) which is able to withstand pressures of 0 kg to 10 kg and had a specification of sensitivity range < 1.5 psi to > 150 psi (0.1 to 10 kg/cm^2). Hoppers with inclination angles of 10, 20, 30, and 45 degrees faced the installed instrument points as seen in Figure 8.

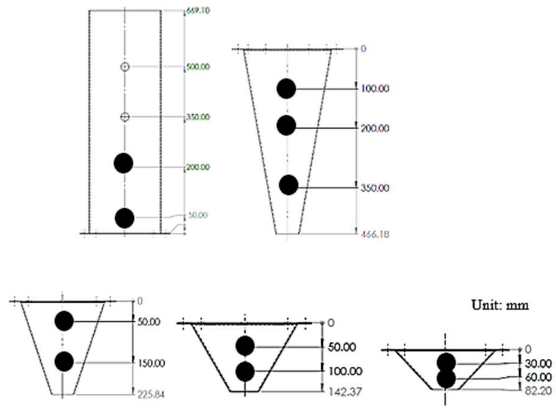

Figure 8 Location of FSR on various hoppers

2.4 Parameter

2.4.1 Normal pressure acting on the silo wall

After filling the material in a silo and storing for 1 hour, the experimental data is obtained while opening the silo's exit channel to allow the material to flow out. The reading data obtained from the pressure sensor mounted on the storage tank and hopper wall is introduced to Eq. (1) This would be as a weight value that can be used to calculate the pressure.

$$P = \frac{F}{A} \tag{1}$$

where P - Normal pressure on silo wall (kPa)
F - Force of fodder obtained from FSR (N)
A - Area of FSR equal to 0.001452 m^2

2.4.2 Mass flow rate

The process of collecting data to calculate the mass flow rate of material can be done in conjunction with pressure-finding experiments at the silo wall. The load sensor monitors the weight of the material being released at any point in time and the average mass flow rate (Q) is obtained by dividing the weight difference of the fodder by the time it takes out the complete. This equation could be expressed as Eq. (2)

$$Q = \frac{|w_1 - w_2|}{|t_1 - t_2|} \tag{2}$$

NUEJ
Naresuan University
Engineering Journal

where Q - Average mass flow rate (kg/s)
w_1 - Weight of fodder at t_1 (kg)
w_2 - Weight of fodder at t_2 (kg)
t_1 - Time (s)
t_2 - Time (s)

3. RESULT AND DISCUSSION

This study considers the pressure on the silo wall and the mass flow rate of the material during the discharging process. The experiment was repeated three times at 32˚c, showing the following results.

3.1 Normal pressure acting on silo wall

The pressure data on the wall of bin and hoppers made of steel and fiberglass with tilt angles of 10, 20, 30 and 45 degrees obtained during the release process are considered in percentage time periods of flow time and presented in Figure 9 and Figure 10, respectively.

From Figure 9, shows the result of normal pressure over the steel wall, it was found that the characteristic of normal pressure greatly depended on the hopper's degree of inclination. Considering the second to fourth period on the release procedure reaching its finish, it is observed that hoppers with an angle of inclination of 10 degrees result the lowest pressure, compared to other hoppers at all places of measurement. It can be seen from the first period that the value of normal stress with hoppers at 10, 20 ,30 and 45 degress are 2.2, 8.3, 10.8, and 14.4 kPa, respectively.

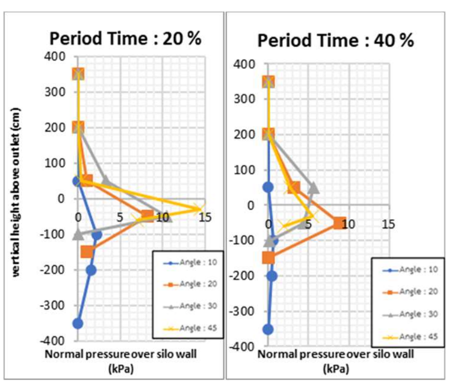

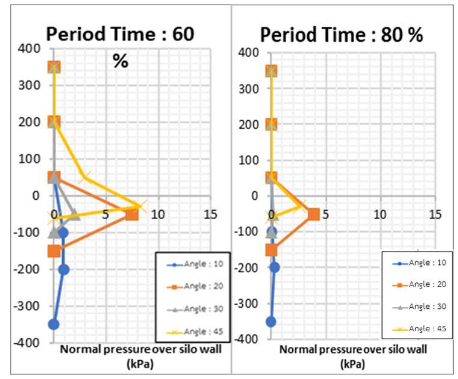

Figure 9 Normal pressure over the steel silo wall with different hopper inclination angles.

When evaluating pressure fluctuation, it is reported that it mostly happens with hoppers at a 45 degree angle of inclination, the result shows that the normal pressure increases at the beginning, then decreases in the second period, then increases in the third period, and finally drops obviously.

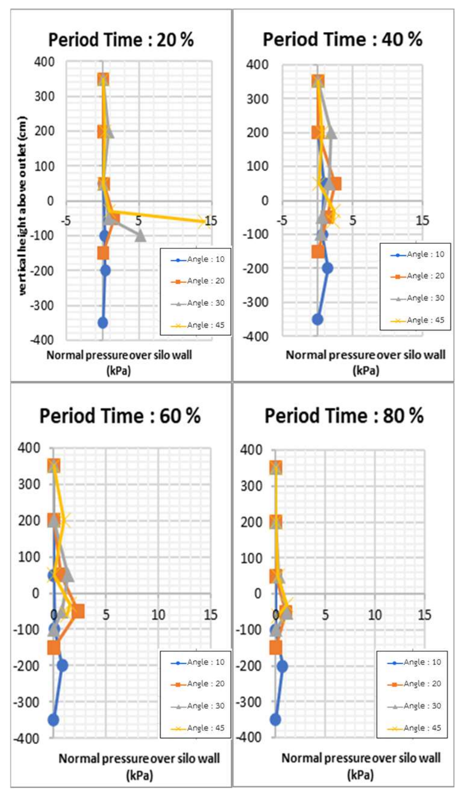

Figure 10 Normal pressure over the fiberglass silo wall with different hopper inclination angles.

From Figure 10, it is found that, at the first period, the pressure varies according to the size of the hopper's angle of inclination and it is noticeable that the results obtained from hoppers with a 10 degree inclination angle present the minimal pressure compared to other size hoppers in all positions of measurement, as well as steel silos. Moreover, similar results are shown when considering the profile of pressure exerted on steel and fiberglass silos. There is the area of the highest pressure under the seam between the bin and the hopper. Then it gradually decreases as it approaches the exit channel. However, the value of pressure generated at the walls of the fiberglass silo is lower than that of the steel silo.

3.2 Mass flow rate

Experiments presented the results obtained from steel hoppers with an angle of inclination of 10 degrees being the highest average mass flow rate of 1.006 kg/s. When comparing the flow rate between steel hoppers and fiberglass, it was found that the testing of steel hoppers showed a higher mass flow rate than the testing of fiberglass hoppers in all values of inclination angle as seen in Table 1. It is because of silos made of steel have better finishing and smoother surfaces than silos made of fiberglass at the experimental time. However, after a given amount of time, the surface of the steel material may corrode, then it causes a decrease in flow rates.

Table 1 Average mass flow rate.

Inclination of hopper (Degrees)	Average mass flow rate (kg/s)		% Diff
	Steel	Fiberglass	
10	1.006	0.677	32.70
20	0.687	0.428	37.70
30	0.472	0.316	33.05
45	0.257	0.238	7.93

It was also found that steel hoppers with an angle of inclination of 45-degrees formed an arch of material above the exit channel and it results in a stoppage of flow as shown in Figure 11. Therefore, a knock was done on the outer wall to facilitate the flow. After that, the material was able to flow out continuously until a material collapse caused the weight of the material to drop sharply. While fiberglass hoppers were non-jammed and gave an average flow rate of 0.238 kg/s, with the reason that the wall friction between particles and fiberglass is lower than that (Santhisan K., Kraitong K. , & Kanokjaruvijit K. , 2022). It is a function of the stress level applied to the wall surface. The wall friction angle is an important parameter; it is used to determine behavior in bin and hopper.

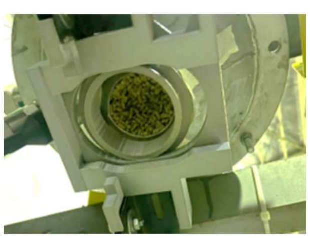

Figure 11 Flow blockage in hopper.

Arching happens when a sufficiently cohesive powder is stored in a hopper that has not steep enough cone walls and/or a large enough outlet. It could be avoided by design by calculating the hopper wall angle required and the critical outlet diameter required in order to always ensure enough constraint to break arches and make the powder flow.

4. CONCLUSION

In all studies, it is discovered that silos made of steel had greater pressure values on the silo wall in the discharge process of fodder materials than silos made of fiberglass and the pressure value varies according to the size of the hopper's angle of inclination. It means that when the hopper has a greater angle of inclination, the pressure becomes greater accordingly. However, it is found that the average mass flow rate of steel silos is higher than that of fiberglass silos. This is due to the factor of the internal surface since the steel silos used in the experiment are newly manufactured and unprocessed. Whereas fiberglass silos have a rougher surface, it is discovered that hoppers with a 10-degree angle of inclination produce the maximum mass flow rates from both steel and fiberglass silos of 1.006 kg/s and 0.677 kg/s, respectively. Also, when considering the effect of the pressure pattern combined with the average flow rate of the material, it could be said that the flow characteristics of fodder in silos which steel and fiberglass produced would be in a funnel flow pattern. In conclusion, the steel silo has better than the fiberglass silo for materials stored for 1 hour.

5. ACKNOWLEDGMENT

This work is part of a Ph.D. research funded by the Faculty of Engineering at Naresuan University. I'd like to thank CPF (Thailand) Public Company Limited for providing raw materials and data.

6. REFERENCES

An, H., Wang, X., Fang, X., Liu, Z., & Liang, C. (2021). Wall normal stress characteristics in an experimental coal silo. *Powder Technology, 377*, 657-665.

Askegaard, V., & Munch-Andersen, J. (1985). Results from tests with normal and shear stress cells in a medium-scale model silo. *Powder Technology, 44*(2), 151-157. doi:https://doi.org/10.1016/0032-5910(85)87022-4

Ayuga, F., Guaita, M., Aguado, P. J., & Couto, A. (2001). Discharge and the eccentricity of the hopper influence on the silo wall pressures. *Journal of Engineering Mechanics, 127*(10), 1067-1074.

doi:10.1061/(ASCE)0733-9399(2001)127:10(1067)

Gandia, R., Júnior, E., Carlos Gomes, F., Coimbra de Paula, W., & Dornelas, K. (2021). EXPERIMENTAL PRESSURES EXERTED BY MAIZE IN SLENDER CYLINDRICAL SILO: COMPARISON WITH ISO 11697. *Engenharia Agrícola, 41*, 576-590. doi:10.1590/1809-4430-eng.agric.v41n6p576-590/2021

Gandia, R. M., Gomes, F. C., Paula, W. C. d., Oliveira Junior, E. A. d., & Aguado Rodriguez, P. J. (2021). Static and dynamic pressure measurements of maize grain in silos under different conditions. *Biosystems Engineering, 209*, 180-199. doi:https://doi.org/10.1016/j.biosystemseng.2021.07.001

Greg Mehos, Mike Eggleston, SHAWN GRENIER, CHRISTOPHER MALANGA, GRISHMA SHRESTHA, & TRAUTMAN, T. (Apr 2018). Designing Hoppers, Bins, and Silos for Reliable Flow. *Chemical Engineering Progress; New York 114*(4), 50-58.

Grudzien, K., & Gonzalez, M. (2013). Detection of tracer particles in tomography images for analysis of gravitational flow in silo. *Image Processing & Communications, 18*. doi:10.2478/v10248-012-0075-2

Härtl, J., Ooi, J. Y., Rotter, J. M., Wojcik, M., Ding, S., & Enstad, G. G. (2008). The influence of a cone-in-cone insert on flow pattern and wall pressure in a full-scale silo. *Chemical Engineering Research and Design, 86*(4), 370-378. doi:https://doi.org/10.1016/j.cherd.2007.07.001

Ramírez, A., Nielsen, J., & Ayuga, F. (2010). Pressure measurements in steel silos with eccentric hoppers. *Powder Technology, 201*(1), 7-20. doi:https://doi.org/10.1016/j.powtec.2010.02.027

Rotter, J. M. (2009). *Silo and Hopper Design for Strength*.

Santhisan K., Kraitong K. , & Kanokjaruvijit K. . (2022, February 14 -15, 2022). *Effect of storage time on flowability of mash feed.* Paper presented at the International Conference on Food and Applied Bioscience, Chiang Mai University.

Tang, J., Lu, H., Guo, X., & Liu, H. (2021). Static wall pressure distribution characteristics in horizontal silos. *Powder Technology, 393*, 342-348. doi:10.1016/j.powtec.2021.07.084

Uñac, R. O., Vidales, A. M., Benegas, O. A., & Ippolito, I. (2012). Experimental study of discharge rate fluctuations in a silo with different hopper geometries. *Powder Technology, 225*, 214-220. doi:https://doi.org/10.1016/j.powtec.2012.04.013

Walker, D. M. (1966). An approximate theory for pressures and arching in hoppers. *Chemical Engineering Science, 21*(11), 975-997. doi:https://doi.org/10.1016/0009-2509(66)85095-9

Wang, X., Liang, C., Guo, X., Chen, Y., Liu, D., Ma, J., . . . An, H. (2020). Experimental study on the dynamic characteristics of wall normal stresses during silo discharge. *Powder Technology, 363*. doi:10.1016/j.powtec.2020.01.023

Wang, X., Shi, Y., Luo, B., Liang, C., Liu, D., Ma, J., & Chen, X. (2022). Flow profile and wall normal stress characteristics in pattern-transformable flow silos. *Chemical Engineering Research and Design, 182*, 381-394. doi:https://doi.org/10.1016/j.cherd.2022.04.019

Zhong, Z., Ooi, J. Y., & Rotter, J. M. (2001). The sensitivity of silo flow and wall stresses to filling method. *Engineering Structures, 23*(7), 756-767. doi:https://doi.org/10.1016/S0141-0296(00)00099-7

NUEJ
Naresuan University
Engineering Journal

New Classification of Textile Samples through l_p Norm Spectral Enhancement Using Template Filters Combining the Analytic Geometry Technique

Wachira Limsripraphan, Suchart Yammen*

Department of Electrical and Computer Engineering, Faculty of Engineering, Naresuan University, Phitsanulok, Thailand

*Corresponding author e-mail sucharty@nu.ac.th

(Received: 3 November 2023, Revised: 27 November 2023, Accepted: 1 December 2023)

Abstract

This paper introduces a novel method for classifying textile fibers into three groups: natural fibers, synthetic fibers, and blended fibers using near-infrared (NIR) spectra obtained via the NeoSpectra-Micro sensor. Our approach involves preprocessing and employing the l_p-norm with p = ∞, 1, and 2 to enhance spectral signals. These enhanced signals alongside textile template filters were obtained from both natural and synthetic fiber groups. Next, the template filters are used to construct a new 2x1 feature vector through covariance-based techniques to effectively reduce spectral data dimension. The feature vector is pivotal for establishing two threshold lines together with an analytical geometry technique to classify for accurate fiber groups. To evaluate the performance of the proposed method, experiments were conducted by using three groups of fiber samples: 210 natural fiber spectra, 480 synthetic fiber spectra, and 270 blended fiber spectra. The dataset was divided into training and testing sets with ten random iterations exploring eight ratios and l_p-norm enhancements for training and evaluation. Remarkably, the experimental result has shown that the overall accuracy remains consistent across the three cases of the l_p-norm enhancements providing the similar accuracies. Considering the limited computational resource, the l_1-norm emerges as a practical choice for embedded systems, emphasizing its practicality for implementation. Moreover, the proposed method additionally provides high accuracies (mean ± standard deviation) of 0.9995 ± 0.0006, 0.9999 ± 0.0004, and 0.9999 ± 0.0005, whereas the ratio of the train and test data is equal to three cases: 10:90, 20:80 and 30:70, respectively, and achieves an exceptional overall accuracy of 100%, whereas the ratio of the train and test data is equal to five cases: 40:60, 50:50, 60:40, 70:30 and 80:20.

Keywords: l_p norm Enhancement, Near-Infrared (NIR) spectroscopy, Template Filters, Textile Fiber Classification

1. INTRODUCTION

The textile industry is one of the most polluting industries, primarily due to its manufacturing processes that extensively use the second highest amount of land resources and the fourth highest amount of water resources. It contributes to greenhouse gas emissions and water pollution, accounting for 10% and 20% of the global world's pollution, respectively (Dissanayake & Weerasinghe, 2021; Filho et al., 2022). Additionally, global post-consumer textile waste has nearly doubled from 58 million to 109 million tons per year in the past decade, leading to issues to textile waste in landfills and contributing to microfiber pollution in oceans.

Recycling textile waste is an important approach to make the textile industry more sustainable and move towards a circular economy. However, only 1% of textile waste can be currently recycled into new clothing due to technological limitations in efficiently and rapidly classifying different fiber components. This is because the fiber composition in textiles, such as polymer fibers in synthetic fabrics and cellulose fibers in natural fabrics, or blended fabrics containing both types, requires different recycling methods (Damayanti et al., 2021; Piribauer & Bartl, 2019).

In recent year, near-infrared (NIR) spectroscopy has become a popularity as a method for textile analysis and classification due to its ease of use, non-destruct the samples, efficiency, cost-effectiveness, and time-saving advantages compared to traditional laboratory-based chemical analysis methods (Guifang et al., 2015; Sun et al., 2015; Chen et al., 2018). However, it is essential to highlight that in the majority of research applications, preprocessing and dimensionality reduction steps are prerequisites before developing classification models. Similarly, alternative methods using low-cost devices, such as image processing, have emerged as viable options for textile classification, as demonstrated by Da Silva Barros et al. (2020). Their approach involves the utilization of mobile device images and Convolutional Neural Networks (CNN) for feature extraction. The experimental results indicate that feature extraction using DenseNet201 and the SVM classification model achieved the highest accuracy, with an accuracy rate of 94.350% and an F1-Score of 94.296%. This underscores the importance of employing robust feature extraction techniques in both NIR spectroscopy and image processing for accurate textile classification.

Wu et al. (2015) employed preprocessing techniques, including the first derivative and the standard normal variant (SNV), before applying the principal component analysis (PCA), a widely used method for linear dimensionality reduction. This approach generated six principal components (PCs), which subsequently served as input variables for a classification model based on least-squares support vector machines (LS-SVM). The LS-SVM model was utilized to classification four types of natural fibers. Sun et al. (2015) employed the Savitzky-Golay first derivative with a five-point window width as preprocessing and used PCA to reduce the initially high dimensionality of 3,000 variables per NIR spectra from the Antaris II FT-NIR spectrometer. They reduced these variables to 3, 4 and 6 PCs, which were used as new input variables for SIMCA analysis, LS-SVM with the RBF kernel function, and the extreme learning machine (ELM) model to classify various fabrics, including cotton, viscose, acrylic, polyamide, polyester, and blend fabric. The results indicated that ELM model achieved a 100% with higher processing speed compared to SIMCA and LS-SVM. Zhou et al. (2019) applied the second derivative as preprocessing before used PCA to reduce 601 variables per NIR spectra obtained from the Brimrose Luminar 3060 AOTF-NIR to three PCs. The new variables were subsequently used in SIMCA analysis to classify seven types of fabric into three groups. The results indicated that PP, PET, PLA, cotton and tencel fabrics were accurately classified with almost perfect accuracy of 100%, whereas wool and cashmere fabrics required another method to achieve best classification accuracy of 100%, specifically the linear discriminant analysis (LDA).

Recently, Ruiz et al. (2022) aimed to enhance the accuracy of classifying post-consumer textile waste by employing data fusion techniques that combined MIR (mid-Infrared) and NIR (near-Infrared) spectroscopy data. Before fusing the given data, they conducted a preprocessing step, which involved applying the first and second derivatives of the Savitzky-Golay smoothing method with a moving average window of 5 and 10 points. They additionally performed mean-centering and balanced the weight of the MIR and NIR spectra data within the 0–1 interval by using min-max normalization. For dimensionality reduction, they utilized the PCA and the canonical variate analysis (CVA) to reduce the dimensionality of the fusion data, which consisted of 3,551 variables from MIR and 2,201 variables from NIR. This reduction produced a new set of variables equal to the number of classes minus one. Subsequently, these new variables served as inputs for a k-Nearest Neighbors (kNN) classification model. The results indicated that the fusion data provided more accurate classification results than using the NIR or MIR spectra data separately, particularly in the case study of blended fibers (mixed between cotton fibers and polyester fiber) achieving the best accuracy with only a 5% error in classification, whereas the error rates for the NIR and MIR spectra were 7% and 6%, respectively. In the same year, Ruiz, Cantero, Riba-Mosoll, et al. (2022) employed a Deep Learning algorithm based on convolutional neural networks (CNNs) to classify textile waste, which included both pure fibers and cotton/polyester blend fibers. They proposed two distinct methods in their methodology both beginning with crucial preprocessing steps involving the calculation of the first or second derivatives and mean-centering of the NIR spectrum. In the first approach, no dimensionality reduction step was applied before the CNN classification. In contrast, the preprocessed spectral data underwent transformation using the PCA and CVA algorithms to reduce dimensionality and create new variables for the classification step alongside the CNN in the second approach. The results demonstrated that the PCA + CVA + CNN approach in the second method outperformed the CNN-only method without dimensionality reduction. Specifically, the PCA + CVA + CNN approach achieved a correct classification rate of 100% in the case study of pure fibers and a correct classification rate of 91.1% in the case study of cotton/polyester blend fibers.

From all the research reviewed above, it is evident that preprocessing processes with a variety of methods such as standard normal variables (SNV), and first or second derivatives combined with Savitzky-Golay smoothing, and widely used dimensionality reduction processes like PCA, are essential for achieving accurate textile classification with NIR data. This finding aligns with our previous research (Limsripraphan & Yammen, 2022), which demonstrated that preprocessing processes with signal enhancement in proposed methods improved the classification efficiency. In addition, it has been shown that improving the accuracy of blended textile classification using NIR spectra remains a major challenge.

This paper presents a novel classification approach to classifying textile samples. The method involves several key steps, starting with $l_p - norm$ spectral enhancement as a preprocessing technique (Cadzow, 2002; Cadzow et al., 2002) and utilizing covariance-based feature filters (Yammen et al., 2021) for dimensionality reduction to extract a useful feature vector. Subsequently, this new feature vector is subjected to the analytic geometry (AG) technique to establish threshold lines that can classify textile fibers into three groups: natural, synthetic, and blended fibers. The performance of the classifiers is evaluated using three key metrics: overall accuracy, precision, and recall. These metrics are also applied to various scenarios, considering different cases of $l_p - norm$ spectral enhancement, where p takes on values of $1,\ 2,\ \infty$ across varying training and testing dataset ratios. The proposed method consistently achieves overall accuracy of 100% for all $l_p - norm$ spectral enhancement, even when the training dataset is reduced unto 30%, which differs from the observed variations in accuracy under different training and testing data ratios.

In conclusion, this paper aims to highlight the improvement in the accuracy of the textile classification using the NIR spectra, particularly in classifying blended fabrics and reducing intensive computational resources. The objective is to employ simple and interpretable methods while comparing the effectiveness of $l_p - norm$ spectral enhancement in achieving best classification accuracy.

2. Spectra Data Preparation

2.1 Sample Collection and Identification

The NIR spectral data in this paper were collected from samples of various types of woven and knitted fabrics commonly used in clothing production. These samples were sourced from fabric distributors and factories in Thailand. The textile samples include natural fibers (such as cotton, linen, and rayon), synthetic fibers (like polyester or spandex) and blended fibers between both types in various proportions from high to low ratios of natural to synthetic fiber. Additionally, to include maximum variability in the analyzed set of samples, each fabric sample was selected in a multitude of colors ranging from dark to light.

All fabric samples were sent to the textile testing center, Thailand's textile institute (THTI), which operates under the Ministry of Industry's Foundation for Industrial Development (FID), to confirm the fiber composition and to identify the fabric samples into three groups. The fiber composition was determined based on the clean dry mass with percentage additions for moisture method under the Thai Industrial Standard (TIS), Standards No.121 part 26-2552. This method is widely recognized for quantifying binary mixtures of fibers in textile products.

In summary, all fabric samples were categorized into three fiber group based on the composition confirmed by THTI: 7 fabric types in natural fiber group, 16 fabric types in synthetic fiber group, and 9 fabric types in blended fiber group, which were further divided into 7 different ratios of natural to synthetic fiber: 68:32, 52:48, 48:52, 36:64, 35:65, 34:66, and 17:83. There are total 32 fabric types, and each of which comes in 3 different colors. Therefore, this research utilized a total of 96 fabric samples for training and testing the performance of the proposed method.

2.2 NIR Spectral Acquisition

The NIR spectra of the textile samples were acquired using the NeoSpectra-Micro Development Kit (Si-ware Systems, Cairo, Egypt), a portable NIR instrument that has shown its reliability for analysis and classification in various fields. These fields include food (McVey et al., 2021; Giussani et al., 2021; Chadalavada et al., 2022), healthcare (Habibullah et al., 2019), agriculture (Du et al., 2019), and textile fibers as shown in a previous study (Yammen et al., 2022; Limsripraphan. et al., 2022; Cadzow, 1999). The device is housed in a specially designed enclosure to prevent interference from external light and to maintain consistent measurements over fabric samples at a height of one centimeter as shown in Figure 1.

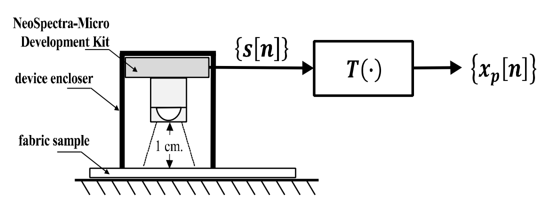

Figure 1 NIR spectral acquisition and spectral enhancement

Each spectral value is acquired using a device that records data for 65 pairs of absorbance and wavelength in the range of 1350 nm to 2550 nm. This data is then transformed in the form of signals representation $\{s[n]\}$, where $n \in \{0,1,2,\ldots,64\}$, as shown in Figure 2. All fabric samples are measured at 10 positions on a fabric sample with dimensions of 30 x 50 centimeters. Therefore, 960 NIR spectral samples were obtained for use in the proposed method.

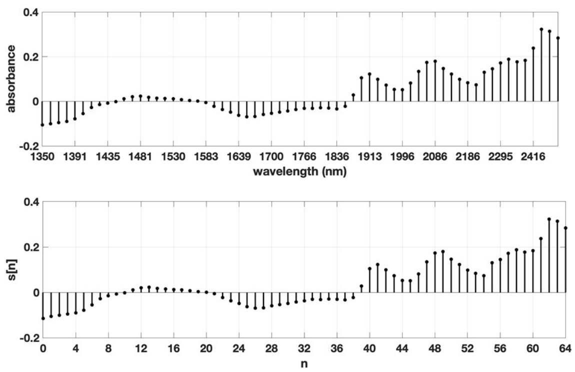

Figure 2 NIR spectral signals representation

2.3 NIR Spectral Signal Enhancement with l_p $norm$

Before applying our proposed classification method to the 960 NIR spectral samples, we introduce $l_p - norm$ spectral enhancement (Cadzow, 1998) as a preprocessing step to reduce the spectral variability of the input spectral signals $\{s[n]\}$ (Bunchuen et al., 2011). In this process, each spectral signal is normalized by subtracting its mean and dividing the result by its l_p norm, resulting in an enhanced spectral signal $\{x_p[n]\}$ as calculated using Eq. (1). We explore various p values to assess their impact on classification accuracy when applying our proposed method in section 4.

$$x_p[n] = T(\{s[n]\}) = \frac{s[n] - \mu_s}{\|\{s[n] - \mu_s\}\|_p} , \quad (1)$$

where: p = 1, 2, ∞ and

$$\mu_s = \frac{1}{65} \sum_{n=0}^{64} s[n] \quad (2)$$

2.4 Train and Test Datasets

In this study, the entire set of enhanced spectral signals $\{x_p[n]\}$, obtained from three enhancement studies using $l_p - norm$ with p values of 1, 2, and ∞ was randomly divided into eight different proportions for the train-to-test dataset within each fiber group. These proportions included 10:90, 20:80, 30:70, 40:60, 50:50, 60:40, 70:30, and 80:20, as shown in Table 1.

This approach allowed us to assess the accuracy of our proposed classification method, which was trained using the train dataset, while ensuring that the testing data were not used during the training step. Additionally, this evaluation helped us understand the performance of our proposed method when the amount of training data is reduced. Moreover, each sample was labeled to identify its respective fiber group, facilitating the assessment of correct classification.

Table 1 Number of Train and Test Samples

proportions	Train dataset			Test dataset		
	Natural (N_n)	Synthetic (N_s)	Blended (N_b)	Natural (N_n)	Synthetic (N_s)	Blended (N_b)
10:90	21	49	27	189	432	243
20:80	42	96	54	168	384	216
30:70	63	144	81	147	336	189
40:60	84	192	108	126	288	162
50:50	105	240	135	105	240	135
60:40	126	288	162	84	192	108
70:30	147	336	189	63	144	81
80:20	168	384	216	42	96	54

3. METHODOLOGY

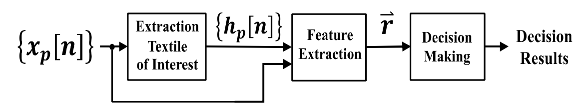

Figure 3 Diagram of proposed classification method

Figures 3 shows our proposed method for classifying textile fibers into three groups. We utilize enhanced spectral signals $\{x_p[n]\}$ as input to extract patterns of interest in natural and synthetic fiber spectra, resulting in the creation of two textile template filters. These template filters are then employed for feature extraction based on covariance, leading to the creation of the two new feature vectors. Each of the two feature vectors is utilized to build a classification system that facilitates decision-making regarding fiber groups.

3.1 Textile Template Filter

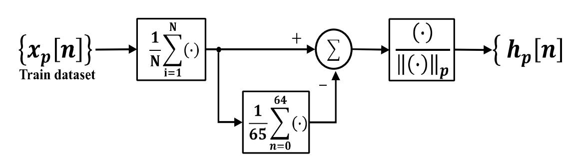

Figure 4 Diagram of create textile templates filter

In this section, we introduce to creation of textile template filter to extract characteristic patterns of interest within in either natural or synthetic fibers spectra group. To create this filters, we start by utilizing input data of interest derived from the training dataset. We computed the average of the enhanced spectral signals $\{x_p[n]\}$, which serves as the input. This average spectrum was then normalized by subtracting its mean and dividing the result by its $l_p - norm$, resulting in the textile template filters $\{h_p[n]\}$ as shown in Figure 4. Consequently, when we utilize spectra from the training dataset of the natural group ($N = N_n$ samples), the textile template filters represent the pattern within natural fiber spectra. Similarly, when employing spectra from the synthetic group ($N = N_s$ samples), the textile template filters represent the pattern within synthetic fiber spectra.

3.2 Feature Extraction with Covariance-based

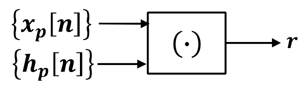

Figure 5 Diagram of covariance-based feature

The proposed method involves a dimensionality reduction process by extracting useful features using the textile template filters $\{h_p[n]\}$, which effectively represent characteristic patterns in natural or synthetic fiber groups. We employ a covariance-based technique (Fuangpian et al., 2011) to assess the similarity between two inputs: the enhanced spectral signals $\{x_p[n]\}$ from unknown fiber groups and the representations of natural or synthetic fiber spectra provided by the textile template filters $\{h_p[n]\}$. This process results in a r value as shown in Figure 5, within the interval from 0 to 1 described in Eq. (3), signifying the degree of similarity.

$$r = \frac{\sum_{l=0}^{64} x_p[l]h_p[l]}{\left\|\{x_p[n]\}\right\|_2 \times \left\|\{h_p[n]\}\right\|_2} \;\; ; \;\; 0 \le r \le 1 \qquad (3)$$

When employing textile template filters from the natural fiber group and utilizing enhanced spectral signals $\{x_p[n]\}$ from the unknown fiber groups as input, the resulting r values, denoted as r_n, indicate a high degree of similarity to the patterns found in natural fiber spectra. Similarly, when employing textile template filters from the synthetic fiber group with the same input enhanced spectral signals, the resulting r values, denoted as r_s, signify patterns highly similar to those present in synthetic fiber spectra. These values are pivotal in our approach as they form the foundation of the new feature vector denoted as a 2x1 feature vector $\vec{r}$ with r_n and r_s as its components. This transformation practically reduces feature dimensionality from 65 to 2, ensuring efficient separation and classification of textile fibers based on their spectral. This new feature vector $\vec{r}$ is used for analysis to create our proposed classification algorithm, which utilizes the analytic geometric technique as shown in Figure 6.

3.3 Classification Algorithm using Analytic Geometric technique

Figure 6. shows a scatter plot of all two-dimensional vectors $\vec{r_i}$ obtained from the training dataset, comprising three distinct fiber groups, where $i \in \{1,2,3,\dots,N\}$. Each vector is represented as an ordered pair (r_{ni}, r_{si}), with r_{ni} denoted the x-axis component and r_{ni} representing the y-axis component.

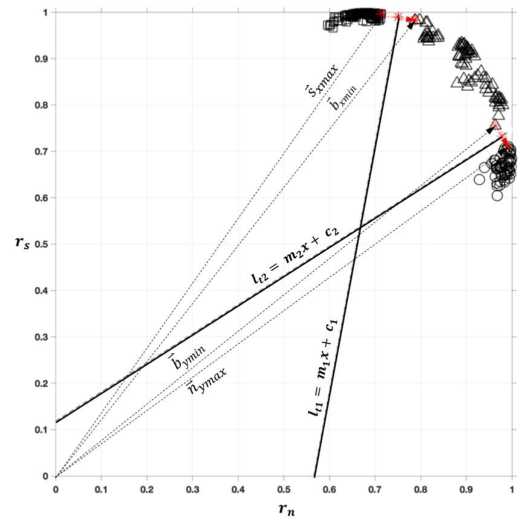

Figure 6 Classification using Analytic Geometric technique

Vectors from the synthetic fiber group (square symbol) cluster near the y-axis, while those from the natural fiber group (circle symbol) cluster near the x-axis. This demonstrate that r_{si} corresponds to synthetic fiber patterns, and r_{ni} to natural fiber patterns. Therefore, vectors from the blended fiber group (triangle symbol) lie between these clusters, demonstrating their relationships. To effectively separate these groups and determine the boundaries between them, we employ vector and geometric analysis techniques to establish two critical threshold lines: l_{t1} and l_{t2}.

In Eq. (4) and Eq. (5) as described, the two essential vectors, $\vec{s}_{xmax}$ and $\vec{b}_{xmin}$, are used in the process of establishing l_{t1}. These vectors play a pivotal role in signifying the boundaries between the synthetic and blended fabric groups.

$$\vec{s}_{xmax} = [r_{nN_s^*} \quad r_{sN_s^*}]^T \;, \qquad (4)$$
$$where \;\; r_{nN_s^*} = \max_{i \in \{1,2,3\dots N_s\}} \{r_{ni}\}$$

$$\vec{b}_{xmin} = [r_{nN_b^*} \quad r_{sN_b^*}]^T \;, \qquad (5)$$
$$where \;\; r_{nN_b^*} = \min_{i \in \{1,2,3\dots N_s\}} \{r_{ni}\}$$

The based vector $\vec{s}_{xmax}$ is determined on $N_s^* \in \{1,2,3 \dots N_s\}$, which represents the index of the maximum value r_{ni} within the synthetic fabric group. Similarly, the based vector $\vec{b}_{xmin}$ is determined on $N_b^* \in \{1,2,3 \dots N_s\}$, which represents the index of the minimum value r_{ni} within the blended fabric group. After identifying these key vectors, we calculate the midpoint vector $\vec{c}_1$, which serves as the center point of our geometric approach, as described in Eq. (6):

$$\vec{c}_1 = 0.5 \times \left(\vec{s}_{xmax} + \vec{b}_{xmin}\right) \quad (6)$$

Subsequently, we create a perpendicular line to the midpoint vector $\vec{c}_1$. This line is instrumental in establishing l_{t1}, which define the boundary between the synthetic and blended fabric groups. We find the slope $m_1$of the line using a component of vectors as described in Eq. (7):

$$m_1 = -\frac{\vec{b}_{xmin}(1) - \vec{s}_{xmax}(1)}{\vec{b}_{xmin}(2) - \vec{s}_{xmax}(2)} \quad (7)$$

Additionally, we define the equation of the threshold line as $l_{t1} = m_1 x + c_1$, where $0 \leq x \leq 1$. The y-intercept c_1 is calculated by using a component of vector $\vec{c}_1$, as described in Eq. (8):

$$c_1 = \vec{c}_1(2) - \vec{c}_1(1) \times m_1 \quad (8)$$

For the second threshold line l_{t2}, which signifies the boundary between the blended and natural fiber groups, we follow a similar procedure to create vector $\vec{b}_{ymin}$ and $\vec{n}_{ymax}$ as described by Eq. (9) and Eq. (10):

$$\vec{b}_{ymin} = [r_{nN_b^*} \quad r_{sN_b^*}]^T, \quad (9)$$

$$where \quad r_{sN_b^*} = \min_{i \in \{1,2,3 \dots N_b\}} \{r_{si}\}$$

$$\vec{n}_{ymax} = [r_{nN_n^*} \quad r_{sN_n^*}]^T, \quad (10)$$

$$where \quad r_{sN_n^*} = \max_{i \in \{1,2,3 \dots N_n\}} \{r_{si}\}$$

The based vectors: $\vec{b}_{ymin}$ is determined on $N_b^* \in \{1,2,3 \dots N_n\}$, which represents the index of the minimum value r_{si} within the blended fabric group. Conversely, the based vector $\vec{n}_{ymax}$ is determined on $N_n^* \in \{1,2,3 \dots N_n\}$, which represents the index of the maximum value r_{si} within the natural fabric group.

With these two vectors, we create l_{t2} using the same geometric analysis techniques. We calculate the slope m_2 by using the components of the vectors with the formula as described in Eq. (11):

$$m_2 = -\frac{\vec{n}_{ymax}(1) - \vec{b}_{ymin}(1)}{n_{ymax}(2) - b_{ymin}(2)} \quad (11)$$

The equation of the threshold line l_{t2} is expressed as $l_{t2} = m_2 x + c_2$, where $0 \leq x \leq 1$, and we compute calculate the y-intercept c_2 by using a component of vector $\vec{c}_2$, as described in Eq. (12):

$$c_2 = \vec{c}_2(2) - \vec{c}_2(1) \times m_2 \quad (12)$$

In our classification process, once the constants for l_{t1} and l_{t2} have been determined, these threshold lines play a pivotal role in the classification of unknown vectors, represented as (r_{nu}, r_{su}), into one of three distinct fiber groups: natural, synthetic, or blended fiber group. Our algorithm employs a fundamental linear equation and follows the sequence of criteria checks:

Step 1: if $r_{su} - m_1 \times r_{nu} + c_1 > 0$, classify the unknow vector into the synthetic groups. If this condition is not met, proceed to the next classification.

Step 2: if $r_{su} - m_2 \times r_{nu} + c_2 < 0$, classify the unknow vector into natural group. If this condition is not met, the unknown vector is classified into the blended group.

In this section, we have detailed our classification algorithm based on the analytic geometric technique. The algorithm's fundamental linear equations and criteria have been explained. In the next section, we will present the outcomes of applying this algorithm with training dataset, providing insights into its performance.

3.4 Results of NIR Signal Enhancement with l_p norm

Figures 7 to 9 (a) show three examples of the raw fiber spectra $\{s[n]\}$ in each group, which have the same similar pattern but exhibit variability and slight differences due to noise or bias, making it challenging to identify the group. In Figures 7 to 9 (b-c), the enhanced spectral signals $\{x_p[n]\}$ with l_p $norm$, where $p = \infty$,1 and 2, respectively, are shown and can effectively reduce spectral variability. This ensures that all signals have equal power to one.

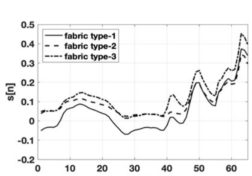

(a) raw spectra signal

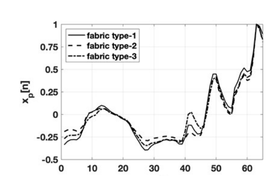

(b) Enhanced with p = ∞

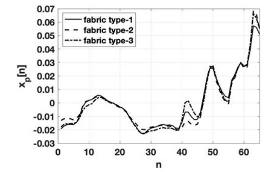

(c) Enhanced with p = 1

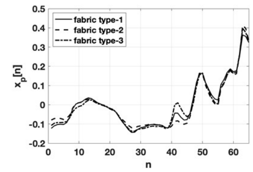

(d) Enhanced with p = 2

Figure 7 Signal enhancement with l_p $norm$ of Natural fiber group

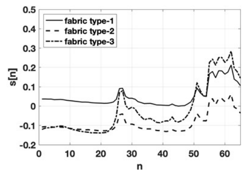

(a) raw spectra signal

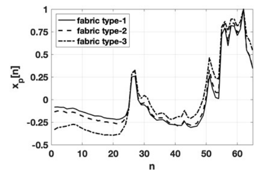

(b) Enhanced with p = ∞

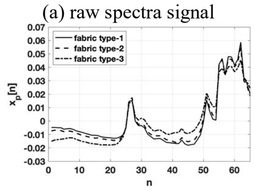

(c) Enhanced with p = 1

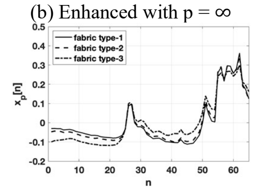

(d) Enhanced with p = 2

Figure 8 Signal enhancement with l_p $norm$ of Synthetic fiber group

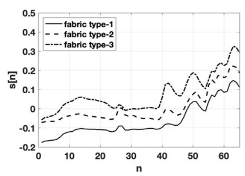

(a) raw spectra signal

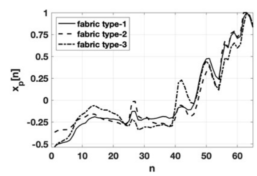

(b) Enhanced with p = ∞

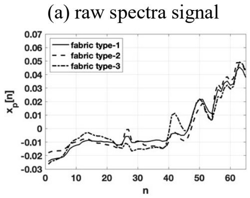

(c) Enhanced with p = 1

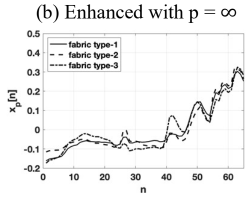

(d) Enhanced with p = 2

Figure 9 Signal enhancement with l_p $norm$ of Blended fiber group

3.5 Result of Analytic Geometric Classification with l_p norm

We extend the proposed method from Section 3 to demonstrate the use of spectral signal enhancement $\{x_p[n]\}$ with three different l_p $norm$ cases in the creation of new feature vectors $\vec{r}$, which extract features using the covariance-based technique. In Figures 10 (a), (b) and (c), we present vector data obtained from a 50:50 training dataset enhanced with l_p $norm$, where $p = \infty$,1 and 2, respectively. The figures illustrate that each l_p $norm$ generate a distinct threshold line l_{t1} and l_{t2}, with slight variations in the two constant values m (slop) and c (intercept) in line equation.

From Table 2 and 3, show the average values and standard deviations of the constants m_1, c_1, m_2 and c_2 for threshold line l_{t1} and l_{t2}. These values were obtained through ten random iterations on various dataset ratios. Threshold line l_{t2} demonstrates minimal variance in standard deviation values across different l_p $norm$ enhancements. However, the variance in standard deviations values is notably higher for threshold line l_{t1}. This variance decreases gradually as the l_p $norm$ shift from ∞ to 2, respectively.

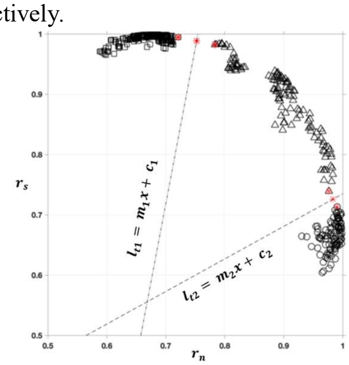

(a) Classification with $l_p - norm$ spectral enhancement, where $p = \infty$

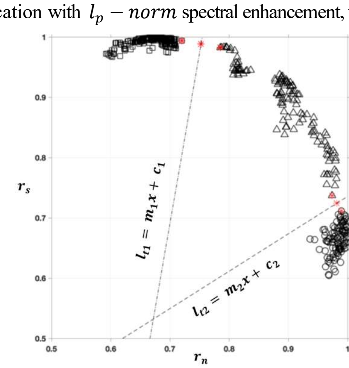

(b) Classification with $l_p - norm$ spectral enhancement, where $p = 1$

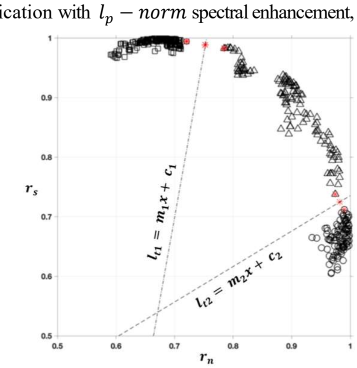

(c) Classification with $l_p - norm$ spectral enhancement, where $p = 2$

Figure 10 The new feature vector from proposed classification method with $l_p - norm$

Table 2 Average value of constants for threshold line l_{t1}

l_p norm	m_1	c_1
$p = \infty$	-10.742 ± 21.174	9.031 ± 15.882
$p = 1$	9.472 ± 14.058	-6.146 ± 10.552
$p = 2$	5.086 ± 8.104	-2.855 ± 6.078

Table 3 Average value of constants for threshold line l_{t2}

l_p *norm*	m_2	c_2
$p = \infty$	0.514 ± 0.111	0.227 ± 0.112
$p = 1$	0.591 ± 0.138	0.151 ± 0.139
$p = 2$	0.568 ± 0.129	0.173 ± 0.130

3.6 Results of the proposed method evaluation

To evaluate the performance of the proposed method for textile fiber classification into the natural, synthetic and blended classes, we utilize four evaluation metrics: overall accuracy, precision, and recall. These metrics are calculated using data extracted from the confusion matrix, which is generated from the classification results utilizing the test dataset with parameters obtained from the training process, unique to each iteration and acquired from ten random iterations with various dataset ratios across three different cases of l_p $norm$ enhancements with value of $p = \infty$,1 and 2. The evaluation process consists of following steps:

Step 1: Extract feature from spectral signal enhancement $\{x_p[n]\}$ using the textile template filters $\{h_p[n]\}$ for natural and synthetic, resulting in a new feature vector $\vec{r}$.

Step 2: Utilize the vector $\vec{r}$ for classification with the analytic geometric classification with constant of both threshold lines l_{t1} and l_{t2}.

Step 3: Count and record the classification results in the confusion matrix, as show in Table 4. Then, calculate the overall accuracy, precision, and recall evaluating the classification performance.

Table 4 The confusion matrix for multi-class classification.

	Actual Class			
	Class	**Natural**	**Synthetic**	**Blended**
Predicted Class	**Natural**	C_{11}	C_{12}	C_{13}
	Synthetic	C_{21}	C_{22}	C_{23}
	Blended	C_{31}	C_{32}	C_{33}

Table 4 represents a confusion matrix tailored for a multi-class classification task with three distinct classes: natural, synthetic, and blended. Within this matrix, the diagonal values C_{11}, C_{22}, and C_{33} signify *true positive* (*TP*) for each class, indicating the number of samples correctly classified within their respective classes. To calculate *false negative* (*FN*) for a specific class, look at the off-diagonal values associated with that class. For natural class, use $FN_{\text{Natural}} = C_{21} + C_{31}$. These values represent natural samples incorrectly classified as synthetic and blended, respectively. Similarly, to calculate *false positive* (*FP*) for the natural class, use $FP_{\text{Natural}} = C_{12} + C_{13}$. These values represent the instances of incorrect classifications, where samples from other classes, synthetic and blended were incorrectly classified as natural class. For a more detailed breakdown of *TP*, *FN*, *FP* and *TN* for each class shown in Table 5. The expanded information offers insights into the classification results for each class.

Table 5 The confusion matrix for multiclass classification.

	Natural	**Synthetic**	**Blended**
TP	C_{11}	C_{22}	C_{33}
FN	$C_{21} + C_{31}$	$C_{12} + C_{32}$	$C_{13} + C_{23}$
FP	$C_{12} + C_{13}$	$C_{21} + C_{23}$	$C_{31} + C_{32}$
TN	$C_{22}+C_{23}+C_{32}+C_{33}$	$C_{11}+C_{13}+C_{31}+C_{33}$	$C_{11}+C_{12}+C_{21}+C_{22}$

From Table 4, to calculate the overall accuracy, which reflects the proportion of correctly classified instances across all classes and provides an overall view of the classifier's performance, you can use the formulation as described in Eq. (13):

$$Overall\ Accuracy = \frac{\sum_{k=1}^{3} c_{kk}}{\sum_{i=1}^{3}\sum_{j=1}^{3} c_{ij}} \tag{13}$$

Moreover, the result of overall accuracy in various of train: test ratio across three different cases three different cases of l_p $norm$ enhancements with value of $p = \infty$,1 and 2, as show in Table 6.

Table 6 Overall Accuracy across different Train: Test ratios and l_p $norm$ cases.

Ratio Train:Test	$p = \infty$	$p = 1$	$p = 2$
10:20	0.9995 ± 0.0006	0.9995 ± 0.0006	0.9995 ± 0.0006
20:80	0.9999 ± 0.0004	0.9999 ± 0.0004	0.9999 ± 0.0004
30:70	0.9999 ± 0.0005	0.9999 ± 0.0005	0.9999 ± 0.0005
40:60	1.0000±0.0000	1.0000±0.0000	1.0000±0.0000
50:50	1.0000±0.0000	1.0000±0.0000	1.0000±0.0000
60:40	1.0000±0.0000	1.0000±0.0000	1.0000±0.0000
70:30	1.0000±0.0000	1.0000±0.0000	1.0000±0.0000
80:20	1.0000±0.0000	1.0000±0.0000	1.0000±0.0000

In Table 6, it is demonstrated that the overall accuracy remains consistent across various l_p $norm$ enhancements, indicating high performance. The value of p does not significantly affect the results. Considering the lower computational resource requirements, the $l_1\ norm$ is often preferred over the $l_2\ norm$, which involves more complex square root calculations, and the $l_\infty\ norm$, which requires finding the maximum absolute value. Therefore, the $l_1\ norm$ is an appropriate choice, especially when the method is intended for application in an embedded system, emphasizing practicality in implementation. Subsequently, we will narrow our focus to the case of $l_p\ norm$ enhancement with $p = 1$ to assess the classification performance for each individual class.

We utilize data from Table 5 to calculate the evaluation metrics of precision, recall, and accuracy for each class, and these results are presented in Tables 7 thru 9 to assess the classification performance:

Precision: measures the proportion of correctly predicted positive outcomes to all the predicted positive outcomes, with an emphasis on avoiding false positives as described in Eq. (14):

$$Precision = \frac{TP}{TP + FP} \tag{14}$$

Recall: represents the proportion of correctly predicted positive outcomes to all the outcomes in each class, focusing on the ability to avoid false negatives as described in Eq. (15):

$$Recall = \frac{TP}{TP + FN} \tag{15}$$

Accuracy: This metric measures the proportion of correctly classified instances and is defined by Eq. (16):

$$Accuracy = \frac{TP + TN}{TP + FN + FP + TN} \tag{16}$$

Table 7 Precision results across different Train:Test ratios.

Ratio Train:Test	Natural	Synthetic	Blended
10:20	0.9979±0.0027	1.0000±0.0000	1.0000±0.0000
20:80	0.9994±0.0019	1.0000±0.0000	1.0000±0.0000
30:70	0.9993±0.0021	1.0000±0.0000	1.0000±0.0000
40:60	1.0000±0.0000	1.0000±0.0000	1.0000±0.0000
50:50	1.0000±0.0000	1.0000±0.0000	1.0000±0.0000
60:40	1.0000±0.0000	1.0000±0.0000	1.0000±0.0000
70:30	1.0000±0.0000	1.0000±0.0000	1.0000±0.0000
80:20	1.0000±0.0000	1.0000±0.0000	1.0000±0.0000

Tables 7 thru 9 clearly demonstrate the exceptional performance of our proposed method, consistently achieving a perfect score of 1 for precision, recall, and accuracy in the synthetic class across various train: test ratios. This remarkable performance showcases the method's robust and reliable nature, even when dealing with a limited training dataset. However, it's important to note that when the training dataset size is below the 40:60 ratio, the precision of the natural class and the recall of the Blended class do not reach a perfect score. Consequently, this results in the overall accuracy falling short of achieving a score of one. Nevertheless, our method outperforms the approach by Ruiz et al. (2022), which involved data fusion between MIR and NIR, achieving the highest accuracy of 95% in the case study of blended fibers. Furthermore, our method surpasses the approach by Ruiz, Cantero, Riba-Mosoll, et al. (2022) who employed PCA + CVA + CNN which achieved a correct classification rate of 91.1% in the case study of blended fibers.

Table 8 Recall results across different Train:Test ratios.

Ratio Train:Test	Natural	Synthetic	Blended
10:20	1.0000±0.0000	1.0000±0.0000	0.9984±0.0021
20:80	1.0000±0.0000	1.0000±0.0000	0.9995±0.0015
30:70	1.0000±0.0000	1.0000±0.0000	0.9995±0.0017
40:60	1.0000±0.0000	1.0000±0.0000	1.0000±0.0000
50:50	1.0000±0.0000	1.0000±0.0000	1.0000±0.0000
60:40	1.0000±0.0000	1.0000±0.0000	1.0000±0.0000
70:30	1.0000±0.0000	1.0000±0.0000	1.0000±0.0000
80:20	1.0000±0.0000	1.0000±0.0000	1.0000±0.0000

Table 9 Accuracy results across different Train:Test ratios.

Ratio Train:Test	Natural	Synthetic	Blended
10:20	0.9995±0.0006	1.0000±0.0000	0.9995±0.0006
20:80	0.9999±0.0004	1.0000±0.0000	0.9999±0.0004
30:70	0.9999±0.0005	1.0000±0.0000	0.9999±0.0005
40:60	1.0000±0.0000	1.0000±0.0000	1.0000±0.0000
50:50	1.0000±0.0000	1.0000±0.0000	1.0000±0.0000
60:40	1.0000±0.0000	1.0000±0.0000	1.0000±0.0000
70:30	1.0000±0.0000	1.0000±0.0000	1.0000±0.0000
80:20	1.0000±0.0000	1.0000±0.0000	1.0000±0.0000

4. CONCLUSION

This paper introduces an innovative approach for classifying textile fibers based on near-infrared spectrum signals. The proposed method involves spectral signal enhancement using various $l_p\ norm$ values with p = ∞, 1, and 2, as a preprocessing step to assess and compare classification accuracy. The method also incorporates the textile template filters and covariance-based techniques for the feature extraction, which effectively reduces the dimensionality of spectral data into a new 2x1 feature vector. The classification is based on an algorithm rooted in the analytic geometric technique. The results show that the proposed method achieved a perfect overall accuracy of 100% when used with train and test data ratio not less than minimum at 40:60 indicating that it is robust and can generalize even when dealing with a limited training dataset. However, even under varying train and test data ratios such as 30:70, 20:80 and 10:90 ratios, the method maintains impressive accuracy values of 0.9999 ± 0.0005, 0.9999 ± 0.0004 and 0.9995 ± 0.0006, respectively. Nevertheless, this still surpasses our previous study (Yammen & Limsripraphan, 2022) where the highest accuracy achieved was 0.9922 ± 0.0078, but only when using an 80:20 training-to-test dataset ratio. These findings underscore the robustness and reliability of the proposed method in textile fiber classification across different scenarios. A notable contribution of this study is found in the simplicity and minimal computational resource demands of the proposed method, rendering it well-suited for applications in the textile industry. This is especially relevant for the embedded systems used in automating textile recycling processes or in portable devices across diverse fields that employ spectroscopy techniques. In the future work, analytical methods will be improved in predicting the composition of the blended fiber either natural or synthetic fabric.

5. ACKNOWLEDGMENT

The authors are greatly thankful to the research and researcher for industries (RRI) and the TJ Supply Limited Partnership for supporting a research grant.

6. REFERENCES

Bunchuen, S., Boonsri, U., Muneesawang P. & Yammen, S. (2011). Detection Method for Corrosion on the Pole Tip. *Naresuan University Engineering Journal, 6(2), 2011, 1-8.*

Cadzow, J. A. (2002). Minimum ℓ1, ℓ2, and ℓ∞ Norm Approximate Solutions to an Overdetermined System of Linear Equations. *Digital Signal Processing, 12(4), 524-560.* DOI:10.1006/dspr.2001.0409

Cadzow, J. A., & Yammen, S. (2002). Data Adaptive Linear Decomposition Transform. *Digital Signal Processing 12(4), 494-523.* DOI:10.1006/dspr.2001.0408

Cadzow, J. A. (1999). Linear Recursive Operator's Response Using the Discrete Fourier Transform. *IEEE Signal Processing Magazine, 16(2), 100-114.*

Cadzow, J. A. (1998). Multidimensional Recursive Linear System Synthesis. *Digital Signal Processing 8(3), 139-157.* DOI:10.1006/dspr.1998.0312

Chadalavada, K., Anbazhagan, K., Ndour, A., Choudhary, S., Palmer, W. E., Flynn, J. R., Mallayee, S., Pothu, S., Prasad, K., Varijakshapanikar, P., Jones, C., & Kholova, J. (2022). NIR Instruments and Prediction Methods for Rapid Access to Grain Protein Content in *Multiple Cereals. Sensors, 22(10), 3710.* https://doi.org/10.3390/s22103710

Chen, H., Tan, C., Lin, Z., & Wu, T. (2018). Rapid determination of cotton content in textiles by Near-Infrared spectroscopy and interval partial least squares. *Analytical Letters*, *51*(17), 2697–2709. https://doi.org/10.1080/00032719.2018.1448853

Damayanti, D., Wulandari, L. A., Bagaskoro, A., Rianjanu, A., & Wu, H. (2021). Possibility routes for textile recycling technology. *Polymers*, *13*(21), 3834. https://doi.org/10.3390/polym13213834

Da Silva BarrosM, A. C., Firmeza Ohata, E., Da Silva, S. P., Silva Almeida, J., & Reboucas Filho, P. P. (2020). An innovative approach of textile fabrics identification from mobile images using computer vision based on deep transfer learning.*2020 International Joint Conference on Neural Networks (IJCNN)*. https://doi.org/10.1109/ijcnn48605.2020.9206901

Dissanayake, G., & Weerasinghe, D. (2021). Fabric Waste Recycling: a Systematic Review of Methods, Applications, and Challenges. Materials Circular Economy, 3(1). https://doi.org/10.1007/s42824-021-00042-2

Du, X., Wang, J., Dong, D., & Zhao, X. (2019). Development and Testing of a Portable Soil

Nitrogen Detector Based on Near-infrared Spectroscopy. IEEE Joint International Information Technology and Artificial Intelligence Conference. https://doi.org/10.1109/itaic.2019.8785499

Filho, W. L., Perry, P., Heim, H., Dinis, M. a. P., Moda, H. M., EbhE. E., & Paço, A. M. F. D. (2022). An overview of the contribution of the textiles sector to climate change. *Frontiers in Environmental Science*, *10*. https://doi.org/10.3389/fenvs.2022.973102

Fuangpian, T., Muneesawang P., & Yammen S. (2011). An Algorithm for Detection of Solder Balls on HGA. *Naresuan University Journal, Special Issue,.24–32*.

Giussani, B., Escalante-Quiceno, A. T., Boqué, R., & Riu, J. (2021). Measurement Strategies for the Classification of Edible Oils Using Low-Cost Miniaturised Portable NIR Instruments. Foods, 10(11), 2856. https://doi.org/10.3390/foods10112856

Guifang, W., Hai, M., & Xin, P. (2015). Identification of varieties of natural textile fiber based on Vis/NIR spectroscopy technology. In IEEE Advanced Information Technology, Electronic and Automation Control Conference. https://doi.org/10.1109/iaeac.2015.7428621

Habibullah, M., Oninda, M. a. M., Bahar, A. N., Dinh, A., & Wahid, K. A. (2019). NIR-Spectroscopic Classification of Blood Glucose Level using Machine Learning Approach. Canadian Conference on Electrical and Computer Engineering. https://doi.org/10.1109/ccece.2019.8861843

Limsripraphan W., & Yammen, S. (2022). Signal Enhancement for Natural Fiber Textile Classification Algorithm. *Proceedings of the 18th Naresuan Research Conference: Steering towards Frontier University: Challenges and Foresight* (*NRC18*). http://conference.nu.ac.th/nrc18/

McVey, C., McGrath, T. F., Haughey, S. A., & Elliott, C. T. (2021). A rapid food chain approach for authenticity screening: The development, validation and transferability of a chemometric model using two handheld near infrared spectroscopy (NIRS) devices. Talanta,222,121533. https://doi.org/10.1016/j.talanta.2020.121533

Ruiz, J. R., Cantero, R., & Puig, R. (2022). Classification of textile samples using data fusion combining near- and Mid-Infrared spectral information. *Polymers*, *14*(15), 3073. https://doi.org/10.3390/polym14153073

Ruiz, J. R., Cantero, R., Riba-Mosoll, P., & Puig, R. (2022). Post-Consumer Textile Waste Classification through Near-Infrared Spectroscopy, Using an Advanced Deep Learning Approach. *Polymers*, *14*(12), 2475. https://doi.org/10.3390/polym14122475

Sun, X., Zhou, M., & Sun, Y. (2015). Classification of textile fabrics by use of spectroscopy-based pattern recognition methods. *Spectroscopy Letters*, *49*(2), 96–102. https://doi.org/10.1080/00387010.2015.1089446

Yammen, S., & Limsripraphan, W. (2022). Matched Filter Detector for Textile Fiber Classification of Signals with Near-Infrared Spectrum. 2022 Asia-Pacific Signal and Information Processing Association Annual Summit and Conference (APSIPA ASC). https://doi.org/10.23919/apsipaasc55919.2022.9980054

Yammen, S., & Muneesawang, P. (2021). P. 2014. An Advanced Vision System for the Automatic Inspection of Corrosions on Pole Tips in Hard Disk Drives. *IEEE Transactions on Components, Packaging and Manufacturing Technology, 4(9), 1523-1533*.

Zhou, J., Yu, L., Ding, Q., & Wang, R. (2019). Textile Fiber Identification Using Near-Infrared Spectroscopy and Pattern Recognition. Autex Research Journal, 19(2), 201–209. https://doi.org/10.1515/aut-2018-0055

Piribauer, B., & Bartl, A. (2019). Textile recycling processes, state of the art and current developments: A mini review. *Waste Management & Research*, *37*(2), 112–119. https://doi.org/10.1177/0734242x18819277

7. BIOGRAPHIES

Wachira Limsripraphan received the bachelor's and master's degree in computer science, Currently, studying for a Ph.D. program in computer engineering from Naresuan University, Phitsanulok, Thailand. He is also employed as an instructor in computer engineering at Pibulsongkram Rajabhat University.

Dr. Suchart Yammen received the bachelor's (2nd Honor with class rank one) degree in electrical engineering from Chiang Mai University, Chiang Mai, Thailand, in 1988, and the M.S. and Ph.D. degrees from Vanderbilt University, Nashville, TN, USA, in 1998 and 2001, respectively. He was a supervisor of the Colgate-Palmolive (Thailand) Company, Ltd., Bangkok, Thailand in 1988, and also served as production engineer in the powder plant. From 1989 to 1993, he was with Siam Cement Public Company, Ltd., Bangkok, not only as a production engineer, a maintenance engineer but also a project engineer. In 1994, he also joined with Naresuan University, Thailand, where he is also currently an associate professor of electrical engineering, he was an assistant to the president for administrative affairs and for information technology, and the Engineering Dean. Furthermore, he is one of the two authors to produce the textbook title: "The Era of Interactive Media" (New York, USA: Springer Publisher, 2012), and has co-authored of the textbook title: *Principles of Communications* (Bangkok, Thailand: Chulalongkorn University Press: CUP, 2011). His current research interests also include various areas of a power electrical engineering, digital signal processing and analysis, automatic control systems, and the related areas in biomedical engineering, computer engineering, renewable energy, energy conservation management, robotics, system identification and modeling.
Dr. Yammen also is various famous professional members, i.e., an IEEE Senior Member, a Fellow Member of the Engineering Institute of Thailand (EIT), Associate Member of Council of Engineers (COE), and the Director for the Research Unit of Biomedical Engineering and Innovation for Social Equality (BEISE) at Faculty of Engineering in Naresuan University, Phitsanulok, Thailand. etc.